République Algérienne Démocratique et Populaire
Ministère de l'Enseignement Superieur et de la Recherche Scientifique
الجمهورية الجزائرية الديمقراطية الشعبية
وزارة التعليم العالي والبحث العلمي
جامعة الإخوة منتوري
Université Frères Mentouri
Faculté des Sciences Exactes
Département de Physique
كلية العلوم الدقيقة
قسم الفيزياء
Université Constantine 1
Tel : +213 (0)31 81 11 72 - Fax : +213 (0)31 81 11 72 - E-mail : departement_physique@yahoo.fr

FACULTE DES SCIENCES EXACTES

DEPARTEMENT DE PHYSIQUE

UNIVERSITE FRERES MENTOURI – CONSTANTINE 1

RELATION CONTRAINTE-ALLONGEMENT POUR LES SOLIDES CRISTALLINES 2D ET 3D

THESE de DOCTORAT EN COTUTELLE

CHORFI HOCINE

TESIS DOCTORAL EN COTUTELA

RELACIONES TENSION-DEFORMACIÓN EN SÓLIDOS CRISTALINOS 2D Y 3D

DEPARTAMENTO DE QUÍMICA FÍSICA Y ANALÍTICA

PROGRAMA DE DOCTORADO EN ANÁLISIS QUÍMICO, BIOQUÍMICO Y ESTRUCTURAL Y MODELIZACIÓN COMPUTACIONAL

Universidad de Oviedo
Universidá d'Uviéu
University of Oviedo

JUILLET 2020 JULIO 2020

Universidad de Oviedo
Universidá d'Uviéu
University of Oviedo

RESUMEN DEL CONTENIDO DE TESIS DOCTORAL

1.- Título de la Tesis	
Español/FrancésOtro Idioma: Relaciones tension-deformación en sólidos cristalinos 2D y 3D/Relation contrainte-allongement pour les solides cristallines 2D et 3D	Inglés: Tension-strain relationships in 2D and 3D crystalline solids

2.- Autor	
Nombre: CHORFI HOCIME	DNI/Pasaporte/NIE:
Programa de Doctorado: Programa de Doctorado en Análisis Químico, Bioquímico y Estructural y Modelización Computacional	
Organo responsable:	

RESUMEN (en español)

El carburo de silicio (SiC), el óxido de zinc (ZnO), el grafito y el disulfuro de molibdeno (MoS2) atraen mucho interés como materiales con aplicaciones tecnológicas para el desarrollo de nuevos dispositivos electrónicos, en particular la nueva generación de semiconductores conocidos como dispositivos de semiconductores de potencia (PSD) o Transistores de efecto de campo (FET). Uno de los mayores desafíos es comprender la ruptura mecánica que ocurre en el proceso de fabricación de estos materiales como resultado de las tensiones inducidas durante los ciclos de calentamiento a los que están sujetos. Por lo tanto, el objetivo fundamental de esta Tesis es la evaluación y análisis en términos químico-físicos de las relaciones tensión-deformación. A partir de estas relaciones, se puede determinar el límite de estabilidad mecánica de estos sistemas. La simulación computacional permite acceder a estas relaciones de forma cuantitativa, proporcionando así información que a veces es difícil de alcanzar experimentalmente. En este estudio, presentamos los resultados de cálculos de primeros principios basados en la teoría del funcional de la densidad que explican cuantitativamente la respuesta de materiales covalentes, iónicos y laminares seleccionados a condiciones generales de estrés. En particular, hemos evaluado la resistencia ideal a lo largo de las principales direcciones cristalográficas de los politipos 3C y 2H de SiC, el apilamiento hexagonal ABA de grafito, varias fases de ZnO y el politipo 2H-MoS2. La tensión transversal superpuesta en la tensión de tracción se tuvo en cuenta para evaluar cómo la resistencia crítica se ve afectada por estas condiciones de carga múltiple. En general, el aumento de la tensión transversal desde valores negativos a positivos conduce a la disminución esperada de la resistencia crítica. Pocas excepciones encontradas en la región de tensión compresiva se correlacionan con las tendencias en la densidad de enlaces a lo largo de las direcciones con el comportamiento inesperado. Además, proponemos una ecuación espinodal de estado modificada capaz de describir con precisión las curvas de tensión-deformación calculadas. Esta función analítica es de uso general y también se puede aplicar a datos experimentales que anticipan resistencias críticas y valores de deformación, y para proporcionar información sobre la energía almacenada en los procesos de tensión de tracción.
La primera parte de esta Tesis Doctoral estará dedicada a la presentación de las bases teóricas y metodológicas de las herramientas computacionales que se utilizan en las simulaciones del comportamiento mecánico que se investigará en estos materiales. En la segunda parte, las relaciones tensión-deformación se evalúan a lo largo de direcciones cristalográficas relevantes, se calcula la resistencia ideal y los resultados se interpretan y explican en términos del enlace químico y el límite de estabilidad termodinámica utilizando la ecuación espinodal. La tesis concluirá con un resumen de las contribuciones más relevantes de este estudio.

Universidad de Oviedo
Universidá d'Uviéu
University of Oviedo

RESUMEN (en Inglés)

Silicon carbide (SiC), Zinc oxide (ZnO), graphite and molybdenum disulfide (MoS_2) attract much interest as materials with technological applications for the development of new electronic devices, in particular the new generation of semiconductors known as Power Semiconductor Devices (PSDs) or Field Effect Transistors (FETs). One of the biggest challenges is to understand the mechanical failure that occurs in the manufacturing process of these materials as a result of the stresses induced during the heating cycles to which they are subjected. Therefore, the fundamental objective of this thesis is the evaluation and analysis in chemical-physical terms of the stress-strain relationships. From these relationships, the limit of mechanical stability of these systems can be determined. Computational simulation allows accessing to these relationships in a quantitative way, thus providing information that is sometimes difficult to reach experimentally. In this study, we present results from first-principles density functional theory calculations that quantitatively account for the response of selected covalent, ionic and layered materials to general stress conditions. In particular, we have evaluated the ideal strength along the main crystallographic directions of 3C and 2H polytypes of SiC, hexagonal ABA stacking of graphite, ZnO and 2H-MoS_2. Transverse superimposed stress on the tensile stress was taken into account in order to evaluate how the critical strength is affected by these multi-load conditions. In general, increasing transverse stress from negative to positive values leads to the expected decreasing of the critical strength. Few exceptions found in the compressive stress region correlate with the trends in the density of bonds along the directions with the unexpected behavior. In addition, we propose a modified spinodal equation of state able to accurately describe the calculated stress–strain curves. This analytical function is of general use and can also be applied to experimental data anticipating critical strengths and strain values, and for providing information on the energy stored in tensile stress processes.

The first part of this Doctoral Thesis will be devoted to the presentation of the theoretical and methodological bases of the computational tools that are used in the simulations of the mechanical behavior that will be investigated in these materials. In the second part, stress-strain relationships are evaluated along relevant crystallographic directions, the ideal strength is calculated and the results are interpreted and explained in terms of the chemical bond and the thermodynamic stability limit using the spinodal equation. The thesis will conclude with a summary of the most relevant contributions of this study.

SRA. PRESIDENTA DE LA COMISIÓN ACADÉMICA DEL PROGRAMA DE DOCTORADO
EN Análisis Químico, Bioquímico y Estructural y Modelización Computacional

REPUBLIQUE ALGERIENNE DEMOCRATIQUE ET POPULAIRE

MINISTERE DE L'ENSEIGNEMENT SUPERIEUR ET DE LA RECHERCHE SCIENTIFIQUE

UNIVERSITE FRERES MENTOURI – CONSTANTINE

FACULTE DES SCIENCES EXACTES

DEPARTEMENT DE PHYSIQUE

N°d'ordre: ……....

Série: ……

THESE

Pour l'obtention du diplôme de

DOCTORAT en SCIENCES

OPTION

CRISTALLOGRAPHIE

par

Hocine CHORFI

THEME

Approche théorique et computationnelle des propriétés physiques des matériaux cristallins

Soutenue le : ……

Devant le jury:

Président: Miloud SEBAIS. Prof. Université Frères Mentouri, Constantine /Algerie

Rapporteur: Boubekeur BOUDINE. Prof. Université Frères Mentouri, Constantine /Algerie

Co- Rapporteur: José Manuel RECIO MUÑIZ. Prof. Université d' Oviedo / Espagne

Examinateurs:

Tarik OUAHRANI. Prof. Université l'Ecole supérieure en sciences appliquées, Tlemcen/Algerie

Mourad ZAABAT. Prof. Université Larbi Ben Mhidi, Oum El Bouagui/Algerie

ACKNOWLEDGEMENTS

باسم الله الرحمان الرحيم

أحمد الله وأشكره على نعمه التي لا تعد ولا تحصى وعلى توفيقه و تيسيره على إنشاء وإتمام هذا البحث ثم من لا يشكر الناس لا يشكر الله فإن كل شكر لمن ساهم بيسير أو وفير و أن يجعلها في ميزان حسناته.

Then, I would like to thank the following people for their contributions to my work.

Completing this amount of research would not have been possible without their support.

- Pr. Fahima Boudjada and Pr. Boubakeur BOUDINE, my advisors and friends whose advices and suggestions were invaluable to overcoming any obstacle encountered in my research work.

- Pr. José Manuel RECIO, my co-advisor whose advices and suggestions were invaluable to overcoming any obstacle encountered in my research work.

- The members of jury committee, Pr. Miloud SEBAIS, Pr. Mourad Zaabat and Pr. Tarik OUAHRANI, who kindly agreed to be part of the jury and to consider my work.

- Dra Ruth FRANCO and Dr Miguel Ángel SALVADÓ.

- My family whose support and constant reminders have helped me.

- All of my friends whose support has helped me.

- And all of the many others who helped me during my work.

- This work was accomplished on Malta supercomputing center of Oviedo university/Spain and financially supported by: Spanish MINECO project CTQ 2015-67755-C2-2-R, Principado de Asturias GRUPIN-0049 and Algerian MERS project PNE/ENS-096/2015-2016 and CNEPRU-project: D00920140037.

Contents

LIST OF FIGURES

LIST OF TABLES

LIST OF ABBREVIATIONS

AE: All electron.

aiPI: atom in Perturbed Ion

AOs: Atomic Orbitals.

B_0: Bulk modulus at 0-pressure.

B'_0: Bulk modulus p-derivative at 0-pressure.

BF: Bloch function.

BFGS: Broyden-Fletcher-Goldfarb-Shanno.

BZ: Brillouin Zone.

CG: Conjugate Gradiant.
DAC: Diamond Anvil Celles
DFT: Density Functional Theory.
DOS: Density Of States

E_F: Energy of Fermi

EOS: Equation Of State.

FETs: Field EffectTransistors.

FFT: Fast Fourier Transforms.
GGA: General Gradient Approximation.

GEA: General Expansion Approximation.

HP: High Pressure.

HF: Hartree-Fock.

HCP: Hexagonal Close Packed.

FHI: Fabius Habber Institute.

IBZ: Irreducible **BZ.**

KS: Kohn-Sham
KB: Kleinmer-Bylander.
LAPW: Linearized Augmented Plane-Wave Method.
LCAO: Linear combination of atomic orbitals.
LDA: Local density approximation.
LSDA: Local Spin density approximation.

LPAW: Linear Projector-Augmented-Wave.

LYP: Lee, Yang and Parr

NN: Nearest neighbors.

OC: Crystalline Orbitals.
PAW: Projector-augmented-wave.

PBC: Periodic Boundary Condition.
PP: Pseudopotential.

PP- PW: PseudoPotential Plane Wave.

PWSCF: Plane Waves Self Consistent Field.
PW: Plane wave.

PDTs: Power Semiconductor Devices.
RMM-DIIS: Residual Minimization Method with Direct Investment in the Iterative Subspace.

SEOS: Spinodal Equation Of State.

SC: Self Consistent.

SNN: Second Nearest Neighbor

STO:

SW: Stillinger-Weber.

TGO: Great Orthogonality Teorem.

TSE: Electronic Severability Theory.

US-PP: Ultrasoft PseudoPotential.

VdW: Van der Waals.

VASP: Vienna ab-initio simulation package
Wz: Wurtzite.
XC: exchange-correlation.
Zb: Zincblende.

SUMMARY

Silicon carbide (SiC), zinc oxide (ZnO), graphite and molybdenum disulfide (MoS_2) attract much interest as materials with technological applications for the development of new electronic devices, in particular the new generation of semiconductors known as Power Semiconductor Devices (PSDs) or Field Effect Transistors (FETs). One of the biggest challenges is to understand the mechanical failure that occurs in the manufacturing process of these materials as a result of the stresses induced during the heating cycles to which they are subjected. Therefore, the fundamental objective of this thesis is the evaluation and analysis in chemical-physical terms of the stress-strain relationships. From these relationships, the limit of mechanical stability of these systems can be determined. Computational simulation allows accessing to these relationships in a quantitative way, thus providing information that is sometimes difficult to reach experimentally. In this study, we present results from first-principles density functional theory calculations that quantitatively account for the response of selected covalent, ionic and layered materials to general stress conditions. In particular, we have evaluated the ideal strength along the main crystallographic directions of 3C and 2H polytypes of SiC, hexagonal ABA stacking of graphite, ZnO and 2H-MoS_2. Transverse superimposed stress on the tensile stress was taken into account in order to evaluate how the critical strength is affected by these multi-load conditions. In general, increasing transverse stress from negative to positive values leads to the expected decreasing of the critical strength. Few exceptions found in the compressive stress region correlate with the trends in the density of bonds along the directions with the unexpected behavior. In addition, we propose a modified spinodal equation of state able to accurately describe the calculated stress–strain curves. This analytical function is of general use and can also be applied to experimental data anticipating critical strengths and strain values, and for providing information on the energy stored in tensile stress processes.

The first part of this Doctoral Thesis will be devoted to the presentation of the theoretical and methodological bases of the computational tools that are used in the simulations of the mechanical behavior that will be investigated in these materials. In the second part, stress-strain relationships are evaluated along relevant crystallographic directions, the ideal strength is calculated and the results are interpreted and explained in terms of the chemical bond and the thermodynamic stability limit using the spinodal equation. The thesis will conclude with a summary of the most relevant contributions of this study.

INTRODUCTION

INTRODUCTION

This thesis is the result of four years of theoretical and computational work aimed at the development and application of chemical and physical models that bridge the gap between the outcome of quantum mechanical electronic structure methodologies and the observed stress-strain phenomena in solids. Stress (σ) along with temperature (T), electromagnetic radiation and chemical agents are the genuine elements of alteration of the properties and functionality of bulk materials systems. They participate in a multitude of phenomena and processes of interest for many areas of knowledge, essential for scientific and technological progress. This is one of the main reasons to have undergone the current investigation.

This fundamental character has ensured, in tune with the advances in modern science, a development of specific research lines focused on both basic and applied aspects of the interaction of these elements on various chemical-physical systems. This is the case of the expansion experienced in the field of High Pressure (*HP*), whose boom in the last decades has been strongly favored the Physics of Condensed Matter, the Sciences of the Materials, the Sciences of Earth and the Planets and even the food sciences [1].

Research on various aspects related to High Pressure is currently carried out routinely in many laboratories due to the development of advanced experimental techniques capable of achieving pressures in the mega bar regime (10^2 *GPa*), particularly thanks to the improvement in methods based on diamond anvil cells (*DAC*) combined with new generation sources of synchrotron radiation and other spectroscopic (infrared and Raman), electrical and magnetic techniques. On the other hand, the increase of the power of the computers together with the greater precision of the calculation programs, where more robust and rigorous theoretical methodologies have been codified, now allow reliable simulations and with predictive character of the response of the materials to various mechanical conditions [2].

The character of the essential role of stress (and particular its hydrostatic representative pressure) is reflected in its ability to correlate the microscopic and macroscopic visions of the matter providing capacity to control and access different geometrical configurations in solids, modifying interatomic distances and angles of bonds. Its effectiveness is higher than that of temperature. In crystalline solids, for example, the volumetric changes vary from a few units to a few tens of percent depending on whether the maximum temperatures or the maximum pressures attainable in the laboratories are applied,

respectively. In the most common experiments, the decrease in volume and the consequent increase in density experienced by a solid sample when subjected to pressure within the *DAC* are quantified through the variable compressibility. In practice, its inverse is evaluated, which is called the modulus of compression (bulk modulus), and at zero pressure it is represented by B_0. This magnitude and its pressure derivative, also evaluated at zero pressure (B'_0), are the fundamental parameters of the equation of state (*EOS*) isotherm of the material system contained in the *DAC*.

When increasing the hydrostatic pressure, it is observed that the stability range of a sample in a certain crystalline structure is finite and, normally, a transformation takes place towards another structure where the packing of its atoms is more effective. A phase transition induced by pressure is therefore produced. This change affects the nature of the bonding chemical network of the solid which can induce for example polymerization processes, as in molecular solids. In addition, it usually increases the hardness and incompressibility and can lead to new magnetic arrangements. The study of polymorphism has, therefore, a great importance in basic aspects such as the understanding of the cohesion of solids, but also in the field of technological applications where, for example, potentially super hard materials have been synthesized by means of induced transitions by pressure [3].

The observable properties of solids are, ultimately, determined by the electronic structure, which, in turn, is governed by the laws of quantum mechanics. The calculations of first principles provide the ideal complement to experimental work. They allow the support, confirmation and interpretation of measurements and experiments. They also may have a predictive character and can provide information about regions that are not experimentally accessible. The use of quantum-mechanical methodologies of the electronic structure in solids to study the effects of stress on crystalline structures has experienced an extraordinary growth in recent years, mainly due to the high reliability of its results and the interdisciplinary nature of High Pressure [2].

This thesis aims to contribute to the understanding of the behavior of crystalline solids when they are subjected to varying conditions of stress, with emphasis on regions of uniaxial tensions rather than hydrostatic compressions. This is the essential contribution of this investigation which differentiates from others carried out in the same group. The fundamental objective that arises in this thesis is the generation of interpretative theoretical models aimed at the understanding of properties, phenomena and processes that exhibit crystalline solids

subjected up to limiting stability conditions of uniaxial tensions with and without superimposed loads. To do this, we resort to first principles quantum-mechanical methodologies for the resolution of the electronic structure, non-empirical algorithms for obtaining equations of state (*EOS*), and theoretical algorithms for evaluating elastic constants. These computational tools allow us to access fundamental properties of matter (structural, elastic, etc.) and compare with the observed behavior in the form of general trends in order to propose simple models for their description.

In order to rationalize the study while keeping also a practical implementation of the investigation, a selection of crystalline systems has been performed. We focus on materials with important and current technological applications in fields as electronics, solar cells and lubricants. For example, in the development of new electronic devices, particularly the last generation of semiconductors known as *PSDs* (Power Semiconductors Devices) [4] and prototype *FFTs* (Field Effect Transistors) [5..8], one of the biggest challenges is to understand the mechanical failure that occurs in the manufacturing processes of these materials as a result of the stress induced during the heating cycles to which they are subjected. The ideal strength, defined as the maximum tension that a crystal can support in the absence of defects in a certain direction, constitutes one of the most important mechanical properties to provide reliable information on this behavior due to the role it plays in the description of these phenomena during the production process. One way to access this fundamental property, both experimentally and theoretically, is through the study of stress-strain relationships. Understanding how these relationships affect the mechanical properties of PSDs and prototype FETs is therefore crucial to optimize their manufacturing processes and the clarification of the types of polymorphic transformations induced by pressure these materials can undergo.

First principles computational simulations based on the density functional theory (*DFT*) allow the quantitative evaluation of stress-strain relationships in any crystallographic direction, thus providing information that is difficult to access experimentally. Although studies of these relationships exist in particular crystalline systems, limited mostly to a small set of directions, it would be also desirable to investigate the general theoretical fundaments of the stress-strain relationships and to systematically address the assessment and analysis of the elastic stability of at least some family of compounds using these relationships and following a computational strategy.

We aim to use theoretical and computational methodologies from Quantum and Physical Chemistry to calculate structural, stability and elastic properties of *2H* and *3C* polytypes of silicon carbide (*SiC*), graphite, zinc oxide(*ZnO*) and molybdenum disulfide (MoS_2). Due to the particular bi-dimensional and three-dimensional atomic arrangements of their crystalline structures, the behavior of these solids is shown to be highly anisotropic. This fact constitutes both, a challenge and an attractive research scenario to our computational approach. The fundamental objective is the determination of the stability limits of these systems when they are subjected to controlled uniaxial and biaxial stresses along the most relevant crystallographic directions. The fulfillment of this objective entails the detailed exploration of tension-deformation curves. For detailed analysis we mean that it is required (i) the interpretation of these relationships in terms of the different chemical bonding networks present in each material, (ii) to establish the correspondence of these curves with the elastic behavior of the materials and (iii) to find the relationship of the calculated critical strengths with the stability limit evaluated by means of the so-called spinodal equation of state (*SEOS*) [9]. This analytical function was designed to describe the high-pressure behavior of condensed matter using as a reference state the onset of elastic instability. It has been successfully applied not only to the description of experimental and theoretical pressure-volume data, but also to the pressure evolution of one dimensional unit cell parameters [10]

The computational codes used in this Thesis can be divided into two groups according to the tasks they perform: (i)-quantum-mechanical methods of solving the crystalline electronic structure and (ii)-equation of state and thermal models to access stability limits and thermodynamic properties of crystalline materials at static and finite temperatures.

The calculation of the electronic structure can be made with different methodologies according to the characteristics of the system and the problem to be treated. For example, in clearly ionic systems, the *aiPI* method is a good option [11,12]. It solves the Hartree-Fock equations of the solid by splitting the crystal wave function into localized group functions using a crystal-consistent procedure. For other systems, different methodologies framed within the approach of the density functional theory can be proposed. The choice of one or the other lies fundamentally in the problem to be dealt with. Thus, all electron electronic density can be obtained with the *CRYSTAL* code [13], which approximates the wave functions by a linear combination of localized orbitals of Gaussian type (*LCAO*). This procedure has on the other hand certain undesired characteristics (linear pseudo dependency problems, base superposition errors, etc.). The immediate alternative is the use of plane waves as base

functions, since they constitute a universal, orthogonal and in principle complete set. This is the strategy implemented in the codes *ABINIT* [14], *PWSCF* [15] and *VASP* [16], which also use the pseudo potential approach, according to which the strong potential of coulomb and the core electrons are replaced by an effective pseudo potential much weaker, and the valence wave functions, which oscillate rapidly in the core region, by pseudo-wave functions, which vary more smoothly in this region and coincide with the real wave functions outside it. This reduces the complexity of the problem. First, by not considering the core electrons explicitly, the number of wave functions to be calculated is smaller. Second, since the potential no longer diverges to $-\infty$ and the valence wave functions are softer within the core region, fewer flat waves are needed to describe the valence wave functions. Within the presented methods, the *ABINIT* method is the one chosen for the study of our crystalline systems.

On the other hand, the *GIBBS* code [17] deals numerically and analytically with energy-volume (*E*-*V*) points calculated in order to deduce pressure-volume relations (*p*-*V*) and parameters of the *EOS* (compressibility module and its derivative with respect to pressure) in static conditions (zero temperature and neglecting the vibrational contributions of zero point). The code used also a non-empirical Debye-type model to give an approximate account of the thermal contributions. In given conditions of *P* and *T*, the evaluation of the Gibbs function allows to identify the thermodynamically stable phase. In our work, we have used computational strategies implemented in the *GIBBS* code to describe energy-strain curves computed with *ABINIT*.

The first block of the two in which this document is organized introduces the fundamentals of the methodologies used in the Thesis. We have also divided it into two parts according to the static or dynamic character of the properties studied. In the first place, we consider the crystalline structure and the electronic structure (chapters 1 and 2). This part contains the bases that allow us the study of the fundamental observables of the solids and also those of prototypical access from the computational point of view. In the second part we consider the response of the crystalline system to forces on the cell or on the atoms (chapter 3). We consider only the linear response. We let the cell to change in shape (not only in size) and the atoms to move. We briefly study the concepts and procedures for calculating elasticity.

The second block of the document collects and discusses the results of quantum-mechanical simulations in a collection of selected crystalline solids. We have divided it into

one single chapter dealing with the four materials under study, *SiC*, *ZnO*, Graphite and MoS_2. They are organized in similar sections presenting: (i)-description of the crystal structure, (ii)-computational details in total energy calculations including the convergence study (bases, k-points, exchange-correlation functional, weak interactions corrections, etc.), (iii)-results and discussion. This last section is further divided into subsections containing our discussion of (1)-observable structural, *EOS* and elastic constants, (2)-evaluation of ideal strength with and without transverse stress effects, and (3)-analysis beyond the stability limit: phase transition and bond breaking.

The Thesis ends with a compilation of the general and particular conclusions of the investigation. At the end of them we have compiled the manuscript that has already been published in the *Nanomaterials* journal.

References

[1] J. M. Recio, J. M. Menéndez and A. Otero-de-la-Roza Eds. **An Introduction to High-Pressure Science and Technology.** CRC Press (2015). Joint 20th AIRAPT- 43rd EHPRG, 2005**. International scientific program Conference on High pressure Science and technology.** e-mail: hikwww.fzk.de/ehprg/conf_prog/.

[2] A. Mújica, A. Rubio, A. Muñoz and R. J. Needs. **High-pressure phases of group-IV, III–V and II–VI compounds.** Rev. Mod. Phys. 75:863, 2003.

[3] J. Z. Jiang, H. Lindelov, L. Gerward, K. Stahl, J. M. Recio, P. Mori-Sanchez, S. Carlson, M. Mezouar, E. Ddooryhee, A. Fitch and D. J. Forst. **Compressibility and thermal expansion of cubic silicon nitride.** Phys. Rev. B, **65**:161202(R), 2002.

[4] K. Asano, T. Hayashi, D. Takayama, Y. Sugawara, S.-H. Ryu, J.W. Palmour, **Temperature dependence of On-state characteristics, and Switching characteristics of 5 kV class 4H-SiC SEJFET.** IEEj Trans. IA **125** (2) (2005) 147.

[5**]** B. Radisavljevic, A. Radenovic, V. Giacometti, A. Kis. **Single-layer MoS2 transistors.** Nat. Nanotechnol. **6**, 2011, 147-150.

[6**]** H. Wang, L. Yu, Y.-H. Lee, Y. Shi, A. Hsu, M.L. Chin, L.-J. Li, M. Dubey, J. Kong, T. Palacios. **Integrated circuits based on bilayer MoS_2 transistors.** Nano Lett. 12, 2012, 4674-4680.

[7**]** G. Fiori, B. N. Szafranek, G. Iannaccone, D. Neumaier. **Velocity saturation in few-layer MoS_2 transistor.** Appl. Phys. Lett 103, 2013, 233509.

[8] S. Kim, A. Konar, W.-S. Hwang, J.H. Lee, J. Yang, C. Jung, H. Kim, J.-B. Yoo, J.-Y. Choi. High-mobility and low-power thin-film transistors based on multilayer MoS2 crystals. Nat. Commun. 3, 2012, 1011.

[9] Baonza, V.G.; Cáceres, M.; Núñez, J. **Universal compressibility behavior of dense phases.** Phys. Rev. B **1995**, 51, 28–37.

[10] Francisco, E.; Bermejo, M.; García Baonza, V.; Gerward, L.; Recio, J.M. **Spinodal equation of state for rutileTiO2.** Phys. Rev. B **2003**, 67, 064110(1)–064110(8).

[11] V. Luaña and L. Pueyo. **Simulation of ionic crystals: The initio perturbed- ion methods and application to alkali hydrides and halides.** Phys. rev. B, **41**:3800, 1990.

[12] M.A. Blanco, V. Luaña and A. M. Pendas. **Quantum mechanical cluster calculations of ionic materials: Revision 10 of the*ab initio* Perturbed Ion program.** Comput. Phys. Commun, 103:287, 1997.

[13] V. R. Saunders, R. Dovesi, C. Roetti, M. Causa, N. M. Harrison, R. Orlando and C. M. Zicovich-Wilson. **CRYSTAL98 User's Manual: Computer Simulation of Materials at Atomic Level.** University of Torino, Torino, 1998.

[14] ABINIT**. http://www.abinit.org**

[15] PWSCF code. http://www.pwscf.org.

[16] G. Kresse and J. Furthmuller. **Efficient iterative schemes for *ab initio* total-energy calculations using a plane-wave basis set.** Phys. Rev. B, 54:11169, 1996.

[17] M. A. Blanco, E. Francisco and V. Luana. **GIBBS: isothermal-isobaric thermodynamics of solids from energy curves using a quasi-harmonic Debye model.** Comput. Phys. Commun, 158:57, 2004.

CHAPTER I

CRYSTAL STRUCTURE

1.1 CRYSTALLOGRAPHY

Point symmetry and periodicity are perhaps the most fascinating and genuine characteristics of crystalline systems. These attributes allow to distinguish crystals from other forms of matter. In the context of group theory, point symmetry is described using point groups and periodicity by means of translation groups, with the global symmetry of the crystal governed by the space groups.

The correlation between the symmetry of the crystal and its observational properties is clear according to the Neumann principle that states that all physical property of a crystal must possess at least the same symmetry as the symmetry of its point group. The crystalline symmetry manifested by real solids is, therefore, of vital importance for the understanding of the electronic structure, the polymorphism, the compressibility, the elasticity and the crystalline vibrations. All these phenomena and properties will be object of study in the present memory.

1.1.1 CRYSTALLOGRAPHIC LANGUAGE

1.1.1.1 unit cell

The crystals are objects in the three-dimensional ($3D$) physical space. A model for its mathematical treatment is point space. Known in crystallography as a direct space. In this, the structures of the finite real crystals are idealized as infinite and perfect crystalline $3D$ structures, which for most applications is an excellent approach.

A vector space V^n ($n = 3$) connected to the point space can also be considered. Thus, the crystalline structures are described in the point space, since the vectors normal to the faces, the translational vectors and the reciprocal lattice are elements of the vector space.

The connection between the vector space V^n and the point space E^n transfers the metric and the dimension of V^n to the point space E^n so that the distances and angles in the point space can be calculated. The translational periodicity implies the existence of translation symmetry operations defined by the set of vectors $\{T_i\}$:

$$\vec{T}_i = u_{i,1}\vec{a}_1 + u_{i,2}\vec{a}_1 + u_{i,3}\vec{a}_1; \quad u_{i,j} \in Z \tag{1.1}$$

Such that set of points at the ends of the translation vectors (nodes) forms a $3D$ network. The three base vectors define a parallelepiped called the unit cell. In this way, the $3D$network is perfectly described by the lengths $a, b\ and\ c$, of the base vectors $(\vec{a}_1, \vec{a}_2, \vec{a}_3)$ and by the three inter axial angles α, β, and Υ, this set constituting the so-called parameters metrics of the structure. Another description of the base can be given through the scalar products of all pairs of base vectors. The set of these scalar products obeys the rules of the second rank covariant tensors and can be written through a 3x3 matrix, called the metric tensor, G, with elements $g_{ik} = \vec{a}_i.\vec{a}_k;\ i,k = 1,2,3$.

The different types of unit cells are characterized by the number of network points they have. Thus, primitive cells contain a lattice point, while those containing two or more lattice points are designed as multiple or centered. The distinction between these two types of cells can be transferred to the vector space. Thus, if the coefficients of all the vectors with respect to the crystallographic basis are integers, the base is primitive, whereas if rational coefficients appear, the base is non-primitive. A unit cell commonly used is the Wigner-Seitz cell. This cell is constructed by choosing as origin any point of the lattice O and drawing planes that bisect perpendicularly the lines that join O with its closest neighbors. Due to the fact that crystals are anisotropic systems it is necessary to identify directions and planes in which specific properties are observed. In this sense, the directions and planes determined by two or three lattice points are called directions and crystallographic planes, respectively. To facilitate the realization of calculations and to allow the interpretation of the physical properties of the glass, the use of the reciprocal space is convenient. Thus, if the base vectors of the real lattice are $\vec{a}_1, \vec{a}_2\ and\ \vec{a}_3$, it is possible to define a set of vectors of the reciprocal lattice $\vec{b}_1, \vec{b}_2\ and\ \vec{b}_3$, where $\vec{b}_i.\vec{b}_j = 2\pi\delta_{ij}$ $(i,j = 1,2,3)$, so that $\vec{b}_1, \vec{b}_2\ and\ \vec{b}_3$ can be written explicitly as:

$$\vec{b}_1 = \frac{2\pi(\vec{a}_2 x \vec{a}_3)}{\vec{a}_1.(\vec{a}_2 x \vec{a}_3)},\ \vec{b}_2 = \frac{2\pi(\vec{a}_3 x \vec{a}_1)}{\vec{a}_2.(\vec{a}_3 x \vec{a}_1)},\ \vec{b}_3 = \frac{2\pi(\vec{a}_1 x \vec{a}_2)}{\vec{a}_3.(\vec{a}_1 x \vec{a}_2)} \qquad (1.2)$$

Thus, any vector of the reciprocal lattice can be written as a function of $\vec{b}_1, \vec{b}_2 and\ \vec{b}_3$ and, by analogy, with equation (1.1):

$$\vec{v}_i = v_{i,1}\vec{b}_1 + v_{i,2}\vec{b}_2 + v_{i,3}\vec{b}_3\ ;\ v_{i,j} \in \mathrm{Z} \qquad (1.3)$$

While in real space x, y, z are used as coordinates for any vector $\vec{r}$, in the reciprocal space $k_x, k_y \; and \; k_z$ are used as coordinates, since any vector in the reciprocal space it is usually designated by $\vec{k}$.

As in the real space the unit cell is defined, in the reciprocal space the first zone of Brillouin is defined, which is, essentially, a unit cell of the reciprocal lattice. Conventionally, the Wigner-Seitz unit cell of the reciprocal lattice is chosen. Another unit cell that is useful to consider is the primitive unit cell, which is the parallelepiped centered on $\vec{k} = \vec{0}$ and with vertices parallel and equal in magnitude to $\vec{b}_1, \vec{b}_2 \; and \; \vec{b}_3$, where $\vec{b}_1, \vec{b}_2 \; and \; \vec{b}_3$ are the base vectors of the reciprocal lattice. The volume of the first Brillouin zone is then given by:

$$\vec{b}_1 . (\overrightarrow{b_2} x \vec{b}_3) = \frac{8\pi^3}{V} \tag{1.4}$$

V being the volume of the real primitive unit cell.

1.1.1.2 Symmetry operations

To understand the periodic and ordered nature of the crystals, it is also necessary to know the rest of the operations, apart from the translation, by which the repetition of the basic unit is obtained and which leave the metric tensor invariant. An operation of any symmetry is represented by an augmented matrix formed by a 3x3 matrix, W, called the linear part (it is the part that defines the rotation) and a column matrix (3x1) that describes the translation in the movement (ω). Thus, any movement of x to its image $\tilde{x}$can be represented by:

$$\tilde{x} = (W, \omega) = Wx + \omega \tag{1.5}$$

Considering the properties of the augmented matrix, three movements can be defined:

▪ translation. In this case $W = I$, where I is the unit matrix and the vector

$\vec{\omega} = \omega_1 \vec{a}_1 + \omega_2 \vec{a}_2 + \omega_3 \vec{a}_3$ is the translation vector.

▪ Movements with at least one fixed point. They are divided into their own movements or rotations if det(W) = +1. Within the improper operations can be inversions if $W = -1$, reflections if $W^2 = I$ and $W = -1$ and rotor inversions in the rest of the cases.

▪ Movements without fixed points and that are not translations (or non-simorphic operations). They are divided into helical rotations if det(W) = +1 and reflections with slip if det(W) $= -1$.

The geometries (points, axes or planes) around which the symmetry operations take place and which correspond to the geometric place of the points that remain for such operations are called elements of symmetry. Not all elements of symmetry are compatible with the periodic nature of space, which imposes restrictions on the type and possible combinations of elements of symmetry. The set of all the symmetry operations of an object forms a group, the symmetry group.

1.1.1.3 Space groups and point groups

In crystallography, the symmetry groups are called space groups and there are 230 types. Classification in types reveals the common symmetry properties of all space groups belonging to a type. Algebraically, the space groups G and G' belong to the same type of space group if there exists a matrix P of dimensions (n + 1) × (n + 1) with det(P) = ± 1 and column p conformed by real numbers such what :

$$W' = P^{-1}WP \tag{1.6}$$

where the matrix part of P describes the translation from the primitive basis of G to the primitive basis of $G'$and the column p of P indicates the possibility of a different origin choice for the operations of G and G'. Recall that W represents an operation of any symmetry of group G . Thus the 219 types of related space groups are obtained. In practical crystallography, however, we want to distinguish the orientation of the helicoidal rotations and we do not want to change the orientation of the coordinate system, so we add the additional condition det$(P) = \pm 1$ to the equation 1.6, such that 11 types of space groups divide themselves, originating the 230 space groups collected in the International Chart of Crystallography [1].

Let's see now how the point groups are defined. If we consider that H is a subgroup of the space group G and g_j an element of G not contained in H, G can be decomposed with respect to H in the following way: $G = HUg_jHUg_kHU$ ...., whereg_jH and g_kH form a coset on the left and on the right of H respectively. Furthermore, if the above decompositions result in the same cosets, except for the order of the elements in each coset, the subgroup H is called

the normal subgroup. An example of a normal subgroup present in all space groups is the translation subgroup. If we call the normal group of translation ξ and decompose the space group G with respect to that:

$$G=\xi UW_i\xi UW_j\xi U \tag{1.7}$$

it can be shown that there is a unique correspondence between cosets and matrices W_j. As a consequence, if the symmetry operations of G are described by the matrices (W,ω), the cosets can be represented alternatively by the matrices W_j. These matrices form a group of finite order, known as group point β of group G. Likewise, it is possible to define the group, G/T, formed by a finite number (h ≤ 48) of own, improper and non-simorphic operations, where the translational vectors $\vec{\tau} = q_1\vec{a}_1+q_2\vec{a}_2+q_3\vec{a}_3$ are restricted to the unit cell: $0 \leq q_1, q_2, q_3 < 1$. The space group is obtained as a direct product of the factor and translation groups: $G = \left(\frac{G}{T}\right) \otimes T$. It is always possible to establish an isomorphism between the factor group and a crystallographic point group. Both will have the same operations and their multiplication table will be equivalent.

The point groups are polar or not depending on whether or not there is a polar direction, without equivalent directions by symmetry, such that a permanent dipole electrical moment appears along this direction.

The set of crystalline structures with the same point group constitute a crystalline class, there being, therefore, 32 crystalline classes in $3D$ space. Algebraically, two space groups G and G' belong to the same crystalline class if the matrix representation W and W' of their point groups are equivalent, there is an actual matrix P such that the equation $W' = P^{-1}WP$ is verified. The name comes from the mathematical definition according to which is a group of symmetry operations that act on a point O leaving all the distances and angles in $3D$ space invariant.

A crystallographic point group must satisfy the extra requirement of being compatible with the translational symmetry of crystalline solids, which reduces the possible operations to identity, inversions, reflections in certain planes and rotations around axes of order 1,2,3,4 or 6. The combination of these operations leads to 32 crystallographic point groups. These can be classified into 7 crystalline systems (syngonies) according to the order of the main axis. There are 5 crystal systems for point groups with a single major axis of order

1,2,3,4 or 6 called triclinic, monoclinic, trigonal, tetragonal and hexagonal crystalline systems, respectively. There are 2 more systems, the orthorhombic with 3 axes of rotation of order 2 mutually perpendicular and the cubic system with 4 axes of rotation of order 3 directed towards the vertices of a regular tetrahedron.

In a given crystalline system, the point group that contains the greatest number of symmetry operations is called the holosimetric point group of the system. It is also possible to assign each of the 14 Bravais networks (possible arrangements of identical points in *3D* space such that the environment of each is identical) to one of the 7 crystalline systems. Through the combination of the 32 point groups with the 14 Bravais networks, the 73 simorphic space groups are obtained, while the remaining 157 groups require the substitution of proper or improper symmetry axes and of reflection planes by sliding axes of the same order and by sliding plans, respectively.

1.1.1.4 Unit cell and symmetry

Normally, crystallography usually chooses unit cells that clearly exhibit the symmetry of the crystal, which is done by selecting vector vectors along symmetry directions and origin at a network point. This leads to so-called cell conventions that are not necessarily primitive, although it is possible to obtain primitive cells from them. In the reciprocal space the choice of the unit cell of Wigner-Seitz in front of others is due to the fact that this unit cell exhibits the symmetry of the point group of the reciprocal lattice. However, for crystals that belong to crystalline systems of low symmetry (monoclinic, triclinic) its construction is very tedious and the primitive unit cell is used. On the other hand, the usefulness of the primitive cells in the reciprocal space is crucial in the calculations of electronic structure (developed in chapter 4). Thanks to them it is possible to simplify the mathematical expressions, and that allow to transform an infinite system (the crystalline cell) into a finite one (the cell of Wigner-Seitz or first zone of Brillouin). The integrals thus have finite limits and, making use of the translational symmetry, the calculations are facilitated.

Given a zone of Brillouin and a point k of this zone there are certain elements of P, the point holosimetric group of the corresponding crystalline system, which transform k into itself or at some equivalent point k'. These elements form a subgroup of P that is denoted by $P(k)$ and is called the symmetry group of k. Based on this, points, lines and planes of symmetry can be defined. Thus, k is a point of symmetry if there exists a neighborhood N of

k in which no point except k has the symmetry group $P(k)$. On the other hand, if in a sufficiently small neighborhood N of k there is always a line (plane) passing through k such that all its points have the same group of symmetry of k, then k is said to be a line (plane) of symmetry.

1.1.2 CHARACTER TABLES

The isomorphism between operations of symmetry, $\hat{R}$ and matrices allows to represent the operations by means of matrices of transformation of coordinates in the base f, $D^{(f)}(\hat{R})$, whose order corresponds with the dimension of the representation. However, the matrix representation of the operations of the symmetry is not unique, but different representations of a group can be obtained through a base change by means of a transformation of similarity, $D^{(g)}(\hat{R}) = AD^{(f)}(\hat{R})A^{-1}$ where A is the matrix that relates the bases $f and\ g$. when there exists the matrix A that transforms by the previous similarity relation all the matrices of the representation $\Gamma^{(f)} = \{D^{(f)}(\hat{R})\}$ in those of the representation $\Gamma^{(g)} = \{D^{(g)}(\hat{R})\}$, $\Gamma^{(f)}$ and $\Gamma^{(g)}$ are equivalent representations. A representation can be reduced if a new coordinate system is found in which each matrix has non zero blocks in the main diagonal and blocks of zeroes outside it (blocked matrices). That is, where $D^{(a)}(\hat{R})$ and $D^{(b)}(\hat{R})$ are matrices $n_1 x n_1$ and $n_2 x n_2$,, respectively, and $n_1, n_2 < n$; $n_1 + n_2 = n$. When this reduction is possible, we say that the representation $\Gamma^{(f)}$ is the right sum of the representations $\Gamma^{(a)} = \{D^{(a)}(\hat{R})\}$ and $\Gamma^{(b)} = \{D^{(b)}(\hat{R})\}$, $\Gamma^{(f)} = \Gamma^{(a)} \otimes \Gamma^{(b)}$. On the other hand, we say that $\Gamma^{(k)}$ is an irreducible representation if there is no matrix A capable of converting all the matrices of $\Gamma^{(k)}$ in an identical block. The enormous advantage of examining the irreducible representations of a group is that:

- A finite group has only a small number of non-equivalent irreducible representations.

- Similarity transformations keep some properties of the matrices (determinant, trace) invariant.

Since the symmetry operations that are part of an equivalence class are also transformed by equivalence relations, the matrices of the operations $\hat{R}$ and $\hat{S}$ that belong to the same class will also have an identical trace and determinant. This allows us to construct a unique table for the group (Table of characters), in which the rows are labeled by non-

equivalent irreducible representations and the columns mediate the equivalence classes of operations. Thus, class i of the irreducible representation $\Gamma^{(f)}$ corresponds to the trace of the matrices $D^{(f)}(\hat{R})$ ($\hat{R} \in$ to class i) also called character. The last two columns list basic functions of the irreducible representations. In the first column, translational and rotational movements appear along and around the x, y, z axes (T_x, T_y, T_z and R_x, R_y, R_z), while in the second, the six components of the polarizability are listed.

The character tables provide essential information for the study of the vibrations of a solid, both for its determination through the factor group analysis, as well as for the assignment of Raman or IR activities. Traditionally, the Mullikan notation is used for irreducible representations. According to this, the irreducible representations of dimension 1 are called A or B depending on whether or not they are symmetric with respect to the rotation around the main axis of symmetry. Moreover, the subindices 1 or 2 depending on whether or not they are symmetrical with respect to the rotation around the axis C_2 perpendicular to the main axis or to the perpendicular plane of reflection. The letter E designates an irreducible representation of dimension 2, while the letter F denotes an irreducible representation triple-degenerated. For pooled groups containing an operation σ_h single and double primes are used, indicating the first symmetry and the second antisymmetry with respect to σ_h. When there is a center of symmetry i, the symbols g and u are used to designate irreducible representations that transform symmetrically and antisymmetrically with respect to i.

One of the results of group theory that has deeper consequences is the Great Orthogonality Theorem (TGO), according to which if $\Gamma^{(f)}$ and $\Gamma^{(g)}$ are two irreducible representations of group C, then:

$$\sum_{\hat{R}} D_{ij}^{(f)}(\hat{R}) D_{kl}^{(g)}(R^{-1}) = \frac{h}{d_f} \delta_{fg} \delta_{il} \delta_{jk} \qquad (1.8)$$

Where the sum runs through all the symmetry operations of the group, h is the order of G, d_f the dimension of $\Gamma^{(f)}$ and $\delta_{ij} = 0$, unless $i = j$. Among the consequences of the TGO are:

▪ The number of non-equivalent irreducible representations matches the class number of the group.

▪ The sum of the squares of the dimensions of all irreducible representations not equivalent to the order of the group.

▪ Any two rows of the table of characters are orthogonal to each other:

If $\sum_R \chi^{(f)}(\hat{R})\chi^{(g)*}(\hat{R}) = h\delta_{fg} = \sum_i \eta_i \chi_i^{(f)} \chi_i^{(g)*}$ where the second summation crosses classes i and η_i is the order of class i.

▪ Any two columns of the table of characters are also orthogonal:

$$\sum_f \chi_i^{(f)*} \chi_j^{(f)} = \frac{h}{\eta_i} \delta_{il}.$$

▪ An arbitrary representation Γ with characters $\{X(\hat{R})\}_{\hat{R}}$ is irreducible if and only if $\sum_{\hat{R}} |\chi(\hat{R})|^2 = \sum_i \eta_i |\chi_i|^2 h$

As a consequence of the theorems seen and the obtaining of the matrices as diagonal blocks, the trace of an irreducible representation is obtained as a sum of diagonal elements in which it can be decomposed. We can write the reducible representation as a direct sum of the irreducible representations, that is $\Gamma = \sum_f a_f \Gamma^{(f)}$ where f go through the irreducible representations and a_f indicates the number of times the irreducible representation $\Gamma^{(f)}$ is contained in Γ.

If this equation is transferred to the characters of each representation, we can determine the coefficients a_f as a consequence of the orthogonality between rows of the character table, such that:

$$a_g = \frac{1}{h} \sum_{\hat{R}} \chi(\hat{R}) \chi^{(g)*}(\hat{R}) = \frac{1}{h} \sum_i \eta_i \chi_i \chi_i^{(g)*} \quad (1.9)$$

1.1.3 INTERNATIONAL CRYSTALLOGRAPHY TABLES

The description of the 230 space groups is included in the International Crystallography Tables [1]. These include notation, equivalent point diagrams by symmetry and arrangement of elements of symmetry, information about the origin, the symmetry operations, the symmetry generators, the Wyckoff positions, the symmetry of space projections and maximum and minimum subgroups. For our purposes, the crystalline structure of a compound is specified from (i)-the space group (selecting the appropriate origin), (ii)-the values of the network parameters, and (iii)-the positions occupied by the atoms in the unit cell with the particular values of these positions for the compound (also called Wyckoff positions).

The positions occupied by the atoms can be general or especial. A point X is said to be a point of general position with respect to a space group G if there is no symmetry operation of G (apart from the identity operation) that leaves X fixed. The set of all the symmetry operations of the space group G that leave point X invariant form a finite group, the point group $G(X)$ of X with respect to the space group.

In the International Tables of Crystallography, information appears about the multiplicity, the letter of Wyckoff [2], the point symmetry, the coordinates and conditions of reflection. Multiplicity is the number of equivalent points per unit cell; for primitive cells, the multiplicity of the general position is equal to the order of the point group of the space group. For centered cells, it is equal to the product of the order of the point group by the number (2, 3, 4) of network points per cell. Thus, the multiplicity of a special position is always a divisor of the multiplicity of the general position. The letter of Wyckoff is, simply, a scheme of code, in alphabetical order of greater to lesser symmetry. The coordinate triplets of a general position can be interpreted as a form of the matrix representation of the symmetry operations of the space group. Its sequence is based on the generators and represent the coordinates of the M equivalent points (atoms) in the unit cell. In the case of space positions, there are specific restrictions on coordinates. The number of Wyckoff positions other than each space group is finite.

Another classification of points in the point space with respect to the space group G is the subdivision of all the points in sets of equivalent points by symmetry, called crystallographic orbits, according to the following definition: the set of all the points that are equivalent by symmetry at a point X with respect to a space group G called the crystallographic orbit of X with respect to G. The crystallographic orbits are infinite sets of points due to the infinite number of translations in a space group. Any one of its points can be the generating point of the crystallographic orbit, and represent, therefore, the total crystallographic orbit. Because the point groups of the different points of the same crystallographic orbit are conjugated subgroups of G, a crystallographic orbit consists of points of general position or points of space position. Therefore, one can speak of crystallographic orbits of general position or special crystallographic orbits. The points of each crystallographic general orbit of a space group G present a one-to-one correspondence with the symmetry operations of G.

This one-to-one correspondence is the reason why the coordinates listed for the general position in the space group tables can be interpreted as the coordinates of the X image points or as a notation for the pairs (W, ω) of the W symmetry operations. Such one-to-one correspondence does not exist for special crystallographic orbits where each point corresponds to a complete coset of decomposition in cosets of the space group with respect to the point group $G(X)$ of X.

A concept of great relevance in crystallography is that of normalizer. The normalizer N of a space group V in the group U of all the affine transformations is the set of those fine transformations that transform X into itself. The space group G is a subgroup of N, where N is a subgroup of U. Thanks to this concept, the Wyckoff set can be defined with respect to G as all the points X for which the point groups are conjugated subgroups of N.

In analogy with the shapes of the faces of the crystalline polyhedra, Paul Niggli introduced the concept of lattice complexes to characterize relationships between dot patterns with space group symmetry. Thus, a network complex is defined as the set of all the crystallographic orbits that can be generated within a type of Wyckoff sets. Different space groups of the same type have their corresponding Wyckoff sets, and we can talk about types of Wyckoff sets. Thus, if the space groups G and G' belong to the same type of space group, the Wyckoff K sets of K' and G' belong to the same type of Wyckoff sets if the fine transformations that transform G into G' also transform K into K'. All the crystallographic orbits belonging to the same network complex can be found following procedure:

▪ Take all the crystallographic orbits of a particular Wyckoff position in a particular space group. Mathematically, their point groups are conjugated subgroups of the space group.

▪ Take all the crystallographic orbits of Wyckoff positions belonging to the same set of Wyckoff (their point groups are conjugated subgroups of the normalizing space group in the affine group).

▪ Take all the crystallographic orbits of Wyckoff sets from all space groups of the same type of affine space group. Each isomorphism, transforming two space groups of the same type one into another, simultaneously transforms the point groups of the points from the crystallographic orbits of the corresponding Wyckoff sets.

Thus, since the crystalline forms of a particular type can be found in different types of point groups, the same network complex can occur in different types of space groups. Accordingly, two Wyckoff positions are assigned to the same network complex. Their space groups belong to the same crystal family and there is an adequate transformation that commutes the crystallographic orbits of the two Wyckoff positions. By this criterion, the Wyckoff positions of all space groups are assigned only to 402 network features.

The concept of network complex is important to reconnect structural relationships in connection with relationships between subgroups and, therefore, in the proposal of mechanisms of phase transitions. For geometric studies it is sufficient to consider only a representative Wyckoff position by network complex.

1.1.4 RELATIONS IN CRYSTALLOGRAPHY

Relationships between crystalline structures simplify relationships between their groups that can be expressed through group-subgroup relationships. A set of symmetry operations $\{H_i\}$ of a space group G is called subgroup H of G if $\{H_i\}$ satisfies the group conditions. A subgroup H is called maximum symmetry or maximal if there is no own subgroup M such that H is a subgroup of $M: H < M < G$. In this case, G is called a supergroup of minimal symmetry of H. The International Tables of Crystallography [1] lists the contingent subgroups in each space group. The diminution of symmetry in these subgroups can take place essentially in three ways: (i)-by reduction of the order of the point group, that is, by eliminating all point symmetry operations of a type. (ii)-for loss of translations, (iii)-by combination of (i) and (ii). The subgroups of the first type are called t-subgroups (or subgroups with equivalent translation), and that the groups of translation of G and H are the same $T(H) = T(G)$, although the subgroup H loses rotation operations with respect to G and, therefore, the point group of H is smaller than that of G: $P(H) < P(G)$.

The subgroups of the second uncle are called k-subgroup (or subgroups with equivalent point group). These present the same point group as the group from which they come: $P(H) = P(G)$, decrease in the order of the translation group $T(H) < T(G)$. Finally, in subgroups of the third type, both the translation group and the point group have a lower order than those of the original group: $T(H) < T(G)$, $P(H) < P(G)$

Fortunately, Herman's theorem states that a subgroup of maximum symmetry of a space group must necessarily be a subgroup t or k. The index of a transformation in a group-

subgroup relationship ($H < G$) can be factored into two parts: $i = i_k . i_t$. In the formula, i_k is the index k, which coicides with the multiplication of the cell in the subgroup in the case of primitive cells and it (the index of translation), is equal to the quotient between the orders of the point groups G and H In the t-subgroup: $i_k = 1$ and $i_t = i$, while in the k-subgroups: $i_t = 1$ and $i_k = i$. Formally, the index associated with a group-subgroup relationship of general type is given by:

$$i = i_k \, . \, i_t = \frac{Z(H)}{Z(G)} \, . \, \frac{P(G)}{P(H)} \tag{1.10}$$

where $P(G)$ and $P(H)$ are the orders of the point groups of the space groups G and H and $Z(G)$ and $Z(H)$ the number of forulas unit per unit unit of the two structures with groups of symmetry G and H. In the general case in which H is not a subgroup of maximum symmetry of G, it is possible to represent its relationship through an intermediate maximal subgroup: $G > Z_1 > \ldots . > Z_n > H$. The index of H in G equals the index product of the intermediate steps. Through a tree diagram it is possible to show the intermediate groups that connect G and H with a certain index.

A particular application is the cross-search of subgroups common to the symmetries of the two structures involved in solids-solid transformation. Although we later discuss the different types of transitions, we can advance that in a reconstructive transition there is no group-subgroup relationship between the initial and final phases. However, we can find a subgroup G common to the space groups of symmetry of the two phases that allows us to describe the structural change of the transition $G1 \rightarrow G2$, being $G1$ the initial space group and $G2$ the end.

Several procedures have been proposed to find these common subgroups imposing limitations for the cell size and a determined maximum distortion [3, 4, 5]. For the proposal of transition mechanisms, Stokes and Hatch only consider subgroups of maximum symmetry, with the addition that the initial and final atomic positions are compatible. In the specific case of the transition $B1 \rightarrow B2$and using cells up to four times the size of the primitive cells of the two groups involved (with $Z = 1$), they obtained the 12 subgroups of maximum symmetry that appear in Table 1.1.

Table 1.1. : Subgroups common to structures $B1$ and $B2$ according to [5]. n is the number of molecules per unit cell.

n	1	2	4
G	$R3m$	$C2(2), Cmc2_1, Pmmn$	$P\,2/c\,(2), P\,2_1/m, PcC\,2/c,$ $P1,$ Iba2

Transformations of coordinate systems are very useful when considering unconventional unit cell descriptions of a crystalline structure. For example, to understand the possible relationships between the structures of the polymorphs of a compound, in the proposal of mechanisms of phase transitions and in group-subgroup relations.

It will then be assumed that while the coordinate system and the unit cell are changed, the crystal structure remains unchanged. A point X of a crystal is defined with respect to the base that make up the vectors $\vec{a}, \vec{b}, \vec{c}$ and the origin O by the coordinates (x, y, z) of the position vector $\vec{r}$. This same point, with respect to the new coordinate system of base vectors $\vec{a}', \vec{b}', \vec{c}'$and origin O', will be described by the vector:

$$\vec{r}' = x'\vec{a}' + y'\vec{b}' + z'\vec{c}' \tag{1.11}$$

The related transformation that relates both position vectors is composed of the matrix P and the column p, which contains the components of the displacement vector $\vec{p}$ and define the transformation unequivocally. This is represented, according to the Seitz notation, by (P, $\vec{p}$). The matrix P implies a change in the orientation, or both of $\vec{a}, \vec{b}, \vec{c}$:

$$(\vec{a}'b'\ \ \vec{c}') = (\vec{a}\vec{b}\vec{c})\,P = (\vec{a}\vec{b}\vec{c})\begin{pmatrix} P_{11} & P_{12} & P_{13} \\ P_{21} & P_{22} & P_{21} \\ P_{31} & P_{32} & P_{33} \end{pmatrix}. \tag{1.12}$$

For a pure linear transformation the displacement vector $(\vec{p})$ is zero and the symbol of the transformation is $(P, \vec{0})$. The determinant of P should be positive. Otherwise, the right-handed coordinate system is transformed into a sinister. If the determinant is zero, the new base is linearly dependent, so it does not complete the space. A displacement of the origin is defined by the vector

$$\vec{p} = p_1\vec{a} + p_2\vec{b} + p_3\vec{c} \tag{1.13}$$

Where the vectors of the new coordinate system are born at the origin O', of coordinates p_1, p_2, p_3 according to the old coordinate system. In the case of a displacement of pure origin, the base vectors do not change their orientation or length, so the transformation matrix P is the unit matrix I, and the global displacement symbol is $(I, \vec{p})$.

The inverse matrix of P and the opposite vector of $\vec{p}$:

$$Q = P^{-1}, \quad \vec{q} = -P^{-1}\vec{p}. \tag{1.14}$$

the matrix Q is formed with the components of the vector $\vec{q}$, which refers to the coordinate system $\vec{a}', \vec{b}', \vec{c}'$:

$$\vec{q} = q_1\vec{a}' + q_2\vec{b}' + q_3\vec{c}' \tag{1.15}$$

the transformation of the components of a vector $\vec{r}$ of the direct space is given by:

$$\begin{pmatrix} x' \\ y' \\ z' \end{pmatrix} = Q \begin{pmatrix} x \\ y \\ z \end{pmatrix} + \vec{q} \tag{1.16}$$

If there is no displacement at origin ($\vec{p} = \vec{q} = \vec{0}$) , the position vector of point X will be given by:

$$\vec{r}' = (\vec{a}'\vec{b}'\vec{c}')PQ \begin{pmatrix} x' \\ y' \\ z' \end{pmatrix} = (\vec{a}\vec{b}\vec{c})\, PQ \begin{pmatrix} x \\ y \\ z \end{pmatrix} = (\vec{a}\vec{b}\vec{c}) = \vec{r} \tag{1.17}$$

in this case $\vec{r}' = \vec{r}$, that is to say the position vector remains invariant, although its components change.

The volume of the V_{cel} unit cell also changes with the transformation:

$$V'_{cel} = \left| P \right| V_{cel} = \begin{vmatrix} P_{11} & P_{12} & P_{13} \\ P_{21} & P_{22} & P_{21} \\ P_{31} & P_{32} & P_{33} \end{vmatrix} V_{cel} \tag{1.18}$$

References

[1] D. Reidel Publishing Company. **International Table for Crystallography.** Boston, USA, 1993.

[2] Ralph W. G. Wyckoff. **T*he analytical expression of the results of the theory of space groups***. published by Carnegie Institution of Washington (1922; second edition, 1930)

[3] C. Mailhiot and A. K. McMahan. **Atmospheric-pressure stability of energetic phases of carbon**. Phys. Rev. B, 44:11578, 1991.

[4] Sowa. **The NaCl- to CsCl-type phase transition discussed on the basis of the cP to cI deformation with the symmetry Cmcm 4(c) m2m.** Acta Crys. A, 56:288, 2000.

[5] H. T. Stokes and D. M. Hatch. **Procedure for obtaining microscopic mechanisms of reconstructive phase transitions in crystalline solids.** Phys. Rev. B, 65:144114, 2002.

CHAPTER II

ELECTRONIC STRUCTURE

2.1. THE PROBLEM OF MANY BODIES

The microscopic description of the matter requires a theoretical model in accordance with the laws of quantum mechanics. In the solids, the electrons move around the nuclei that are in determined positions, according to the symmetry operations of the crystal. The chemical-physical properties of solids are governed by the behavior of electrons, so that the understanding of a significant part of the behavior of condensed matter could be achieved if its electronic structure could be determined exactly.

The basic equation used to describe quantum systems is the Schrödinger equation dependent on time, proposed by Schrödinger in 1926,

$$\hat{\mathrm{H}}\psi(\vec{r},t) = i\hbar\,\psi(\vec{r},t) \tag{2.1}$$

The separation of the wave function $\psi(\vec{r},t)$ in terms of its variables $\vec{r}$ and t,

$\psi(\vec{r},t) = \psi(\vec{r})\,f(t)$, allows to use the non-relativistic and time-independent Schödinger equation, $\hat{\mathrm{H}}\psi_k = E_k\psi_k$ to determine the properties of the stationary states of a system. $\hat{\mathrm{H}}$, $\psi_k(\vec{r}_1, ..., \vec{r}_N, \vec{R}_1, ..., \vec{R}_M)$ and E_k are the Hamiltonian, the wave functions and the energies of the stationary states of the system, where $\vec{r}_i$ and $\vec{R}_A$ are the electronic and nuclear variables, respectively.

The Hamiltonian can be expressed as:

$$\hat{H} = \hat{T}_e + \hat{T}_n + \hat{U} + \hat{V}_{en} + \hat{V}_{nn}, \tag{2.2}$$

Being the contributions to the kinetic energy of electrons and nuclei (in atomic units):

$$\hat{T}_e = -\sum_{i=1}^{N} \frac{\nabla_i^2}{2}, \quad \hat{T}_n = -\sum_{A=1}^{M} \frac{\nabla_A^2}{2} \tag{2.3}$$

and the coulomb electron-electron, nucleon-electron and nucleon-nucleon interactions:

$$\hat{U}=\sum_i^N \sum_{j\neq i}^N \frac{1}{2\,|\vec{r}_i-\vec{r}_j|}, \quad \hat{V}_{en}=\sum_{A=1}^M \sum_{i=1}^N \frac{Z_A}{2\,|\vec{r}_i-\vec{R}_A|}, \quad \hat{V}_{nn}=\sum_{A=1}^M \sum_{B\neq A}^M \frac{Z_A Z_B}{2\,|R_B-\vec{R}_A|} \tag{2.4}$$

The wave form $\psi_k(\vec{r}_1, ..., \vec{r}_N, \vec{R}_1, ..., \vec{R}_M)$ of the ground state contains the basic information we wish to determine. Although all the variables involved in the Schödinger

equation are known, their exact resolution is, in general, invariable in systems with an arbitrarily large number of electrons. Efforts to make the quantum problem of many bodies treatable are centered on finding intelligent approximations to the Hamiltonian H and the wave function ψ that conserve the correct physics and are computationally feasible.

The first simplification of this problem is due to Born and Oppenheimer [1]. Under its approach, the movement of nuclei and electrons can be separated due to the large difference in mass between the both. It can be considered, therefore, that the solid is constituted by a skeleton of atomic nuclei whose positions are decoupled from the electronic movement. The electronic structure is then resolved for frozen nuclear geometries. In this sense, the global Schrödinger equation is simplified into two equations, one electronic and the other nuclear. In the electronic Schrödinger equation the term $\hat{T}_n$ does not intervene and $\hat{V}_{nn}$ is a constant that we can omit:

$$\hat{H}_{elec} = \hat{T}_e + \hat{V}_{en} + \hat{V}_{ee} \tag{2.5}$$

Such that,

$$\hat{H}^i_{elec}\psi^i_{elec} = \epsilon^i\psi^i_{elec} \tag{2.6}$$

where ψ^i_{elec} are the electronic wave functions that depend explicitly on the positions and spin coordinates of the electrons and parametrically on the coordinates of the nuclear positions.$\varepsilon^i$are the energies of the electronic levels of the system. The nuclear repulsion is usually included in this term: $E^i_{elec} = \varepsilon^i + V_{nn}$. If we consider only the fundamental state we can dispense with the term E_{elec} from the superindice and call the nuclear potential because it acts as a potential to which the nuclear movement is subjected:

$$\hat{H}_{nucl}\Phi_{nucl} = E\Phi_{nucl}\ ,\ \hat{H}_{nucl} = \hat{T}_n + E_{elec} \tag{2.7}$$

where E is the total energy of the system and $\Phi_{nucl}\psi_{elec} = \psi$. In the so-called static approximation, which we will frequently use, we consider the immobile nuclei ($T = 0K$ and negligible zero-point vibrations) and, therefore, we only have to worry about solving the electronic Schödinger equation. Despite considering thisapproach, the problem continues to be very difficult to solve, since in a solid the number of interacting electrons is at the macroscopic level of the order of 10^{23}, which entails an intractable task even considering the punctual and translational symmetry of the crystalline system.

2.2. THE HARTREE-FOCK METHOD (*HF*)

The Hartree-Fock theory (HF) [2] is one of the simplest and most efficient approximate theories to solve the problem of N electrons. It is based on an approximation to the true ψ of many bodies. According to this, the electronic wave function HF (ψ_{HF}) of a system of N electrons are constructed as an anti-symmetric product of spinorbitals (ψ_i) through a Slater determinant of the form,

$$\psi_{HF} = \frac{1}{\sqrt{N!}} \begin{vmatrix} \psi_1(\vec{x}_1) \dots \psi_N(\vec{x}_1) \\ \dots \dots \dots \dots \dots \dots \dots \dots \\ \psi_1(\vec{x}_N) \dots \psi_N(\vec{x}_1) \end{vmatrix} \tag{2.8}$$

where the variables $\vec{x}$ include the coordinates of space and spin. This approach to wave function ψ captures much of the physical memory to obtain successful solutions from the Hamiltonian. More importantly, the wave function ψ_{HF} is antisymmetric with respect to an exchange of 2 electronic positions, thereby fulfilling Pauli's exclusion principle:

$$\psi(\vec{x}_1, \vec{x}_2, \dots, \vec{x}_i, \dots, \vec{x}_j, \dots, \vec{x}_N) = -\psi(\vec{x}_1, \vec{x}_2, \dots, \vec{x}_j, \dots, \vec{x}_i, \dots, \vec{x}_N). \tag{2.9}$$

The HF method tries to obtain the best monodeterminantal approximation to the exact wave function ψ through the variational principle. Thus:

$$E_{HF} = \langle \psi_{HF} \left| \hat{H}_{elec} \right| \psi_{HF} \rangle \geq E \tag{2.10}$$

E being the energy of the ground state. The variations are made by varying the shape of the N spinorbitals and conserving the orthonormality $\langle \psi_i | \psi_j \rangle = \delta_{ij}$ until reaching the lowest possible energy. The resulting equations that lead to the best orbitals, called Fock equations

$$\hat{f}(1)\psi_i(1) = [\hat{h}(1) + \hat{u}(1)\,]\,\psi_i(1) = \epsilon_i \psi_i(1) \qquad i = 1, N \tag{2.11}$$

where the operator $\hat{h}$ is defined as:

$$\hat{h}\,(\vec{r}_1) = -\frac{1}{2}\nabla^2 + \hat{V}_{en}(\vec{r}_1) \tag{2.12}$$

And the operator $\hat{u}$ is defined as:

$$\hat{u}(\vec{r}_1) = \sum_{j=1}^{N} \int \psi_j^*(\vec{r}_2)\, \frac{1}{r_{12}}\, (1 - \hat{P}_{12})\, \psi_j(\vec{r}_2) \mathrm{d}\vec{r}_2 \tag{2.13}$$

where $\hat{P}_{12}$ is a permutator that changes electron 1 to 2 and vice versa. The resolution of the Fock equations requires a self-consistent iterative procedure, since the operator $\hat{f}$ depends on its eigen functions ψ_i through $\hat{u}$. These eigenfunctions are fictitious monoelectric operators, which include the kinetic energy and nuclear attraction ($\hat{h}$) and an approximate repulsion averaged ($\hat{u}$) exerted by the rest of electrons.

Once the orbitals have been calculated, it only remains to obtain the total electronic energy of the system, that is:

$$E_{HF} = \langle \psi_{HF} \mid \hat{H} \mid \psi_{HF} \rangle = \sum_{j=1}^{N} \langle \psi_1 \mid \hat{h}(1) \mid \psi_1 \rangle + \frac{1}{2} \langle ij \parallel ij \rangle \qquad (2.14)$$

where $\langle ij \parallel ij \rangle$ is the sum of the terms of coulomb and change:

$$\langle ij \parallel ij \rangle = \int \mathrm{d}\vec{r}_1 \mathrm{d}\vec{r}_2 \frac{\psi_i^*(1)\psi_i(1)\psi_j^*(2)\psi_j(2)}{\mathrm{r}_{12}} - \int \mathrm{d}\vec{r}_1 \mathrm{d}\vec{r}_2 \frac{\psi_i^*(1)\psi_j(1)\psi_j^*(2)\psi_i(2)}{\mathrm{r}_{12}} \qquad (2.15)$$

the first term represents the coulomb repulsion of electron 1 in the orbital ψ_i with the electron 2 in the orbital ψ_j and the last one, the integral of exchange, arises as a consequence of the antisymmetry of the Hartree-Fock wave function. This nonlocal term cancels the self-interaction, or Coulomb repulsion without physical meaning of an electron with it, assuring that $\langle ii \parallel ii \rangle = 0$. The exchange interactions also introduce the correlation associated with the Fermi hole, that is, the physical impossibility that two electrons of the same spin occupy a certain volume. However, the Hartree-Fock theory, assuming a mono-determinantal form for the wave function, does not include the correlation between electrons of different spin. The electrons are subject to an average nonlocal potential generated by the other electrons, which leads in general to a poor description of the electron structure.

The limitations of the Hartree-Fock method can be reduced by going beyond the approximation of a mono-determinantal wave function. The wave function is expressed as a linear combination of Slater determinants in which a set of spinorbitals occupied by virtual ones have been replaced by electronic excitations of a different nature. Basically, there are two ways of dealing with the problem of the electronic correlation: through the theory of perturbations and through the variational principle. Although these post-HF methods, such as interaction of configurations, coupled-cluster and Moller-Plesset theory have been developed extensively in the field of quantum chemistry, they have only recently begun to be used in the preliminary way in the study of solids [3], due to the rapid increase in computational cost

associated with the size of the system. For this reason, in this thesis we have opted to estimate and correct a correlation error a posteriori by using functionalities of the electron density suitable in the cases in which we have resorted to HF formalism in the resolution of the electronic structure of the crystalline system.

2.3. DENSITY FUNCTIONAL THEORY (DFT)

An alternative to the conventional ab initio methods of introducing the effects of electronic correlation in the resolution of the electronic Schrödinger equation is the density functional theory (DFT) [4], in which the basic variable is electron density instead of the wave function. The advantage is obvious since the density only depends on 3 spatial coordinates and the spin, while the wave function depends on $3N$ variables ($4N$ if the spin is included), where N is the number of electrons. Unlike traditional chemistry-quantum methods, in the DFT formalism it is not treated with the N-interacting electron system but with a dynamically equivalent system of N non-interacting fictive electrons that have the same density as the real system. In this way, formalism does not lead to a multielectronic wave function, although the algebraic implementation of the DFT theory through the Kohn-Sham equations [5] is monoelectronic and shares many similarities with the Hartree-Fock formulation.

Formally, it is an exact theory. However, in practice it is necessary to resort to approximations, which does not prevent the accuracy of the calculations from being surprisingly good. On the other hand, the methods developed in light of DFT are substantially simpler and potentially capable of providing results of similar or even greater precision than methods based on wave function with much lower computational cost.

Therefore, the choice of computational methods based on the DFT theory to approach the study of solids has been predominant in recent years.

2.3.1. THEOREMS OF HOHENBERG AND KOHN

The density functional theory was formulated by Hohenberg and Kohn in 1964 [6], following the spirit of the electron-sea model of Tomas-Fermi [7,8] (in which the electronic contributions to the kinetic energy and to the classical electrostatic interactions are obtained using a uniform electron gas), and the subsequent correction of Dirac that includes the energy of electron exchange.

The first theorem states that the expected value of any observable of a fundamental non-degenerate steady state can be calculated, in principle exactly, from the electron density of this fundamental state. That is, the expected value of any observable can be written as a functional of the electron density of the ground state, $O[\rho] = \langle \psi_{[\rho]} \left| \hat{O} \right| \psi_{[\rho]} \rangle$. Thus, in an electron system under an external potential $v(\vec{r})$, the potential is only determined by the electron density. Since electron density determines the number of electrons, $N = \int \rho(\vec{r}) d\vec{r}$, and fix $v(\vec{r})$according to the first theorem of Hohenberg and Kohn, it is concluded that the density determines the Hamiltonian (except in an additive constant) and the wave function of the fundamental state. Consequently, the electronic density fixes all the observable properties of the ground state, including the kinetic energy of the electrons, the potential energy and the total energy.

Thus, the energy of the ground state is a unique functional of the electronic density,

$$v(\vec{r}) = F_{HK}[\rho] + V_{en}[\rho] + V_{nn}), \tag{2.16}$$

Where $F_{HK}[\rho] = T[\rho] + U[\rho]$ is a universal functional density and $T[\rho]$ and $U[\rho]$ kinetic and potential contributions to it.

This demonstration is only valid for v-representable density, that is, for electron densities associated with the antisymmetric wave function of the obtained fundamental state of a Hamiltonian that includes the external potential $v(\vec{r})$. However, not all densities are v-representable. The restricted Levy formulation [9] eliminates the requirement that the density be v-representable. Part of the set of functions, ψ_{ρ_0} that integrate ρ_0 (the exact density of the fundamental state, with wave function ψ_0). According to the variational principle.

$$\langle \psi_{\rho_0} \left| \hat{T} + \hat{U} \right| \psi_{\rho_0} \rangle + \int \rho_0(\vec{r}) v(\vec{r}) d\vec{r} > \langle \psi_0 \left| \hat{T} + \hat{U} \right| \psi_0 \rangle + \int \rho_0(\vec{r}) v(\vec{r}) d\vec{r} \tag{2.17}$$

This expression is immediately reduced to the inequality:

$$\langle \psi_{\rho_0} \left| \hat{T} + \hat{U} \right| \psi_{\rho_0} \rangle > \langle \psi_0 \left| \hat{T} + \hat{U} \right| \psi_0 \rangle \tag{2.18}$$

being the terms of electron-core interaction on each side of the identical inequality. Thus,

$$F_{HK}[\rho] = Min_{|\psi\rangle \to |\psi_0\rangle} \langle \psi \left| \hat{T} + \hat{U} \right| \psi \rangle \tag{2.19}$$

where the universal functional of the electronic density is searching among all the wave functions that generate the electron density $\rho_0(\vec{r})$. And selecting the one that minimizes the expected value $\hat{T} + \hat{U}$, which is none other than the function wave of the fundamental state. It is, therefore, possible to determine ψ_0 only from the knowledge of ρ_0, through a restricted minimization within the set ψ_{ρ_0} of the value of $\hat{T} + \hat{U}$. Consequently, it is shown that there is a biunivocal correspondence between ρ_0 and ψ_0 without the need to consider the external potential $v(\vec{r})$

The restricted Levy formulation also eliminates the requirement that the fundamental states must be non-degenerate, since in the restricted search we limit ourselves to one of the degenerate functions, which corresponds to the density that interferes with us.

Unfortunately, the demonstration of the first theorem of Hohenberg and Kohn is only of existence and does not provide information of the form of the functional $E[\rho]$ so it is necessary to resort to approximations.

The second theorem (known as the variational principle) states that the exact electron density of a non-degenerate ground state minimizes the functional of the total energy $E[\rho]$, from which the variational equation follows:

$$\frac{\delta E[\rho]}{\delta \rho} - \mu = 0 \qquad (2.20)$$

where μ is a Lagrange multiplier that ensures that the functional of the energy is determined by the normalized electron density E, ρ.

2.3.2. THE KOHN-SHAM FORMULATION

Unfortunately, the Euler equation that determines the energy function has no practical meaning for computational purposes. Taking into account the decomposition of $E[\rho]$, the need for an explicit functional form for both the kinetic energy functional and the electron-electron repulsion is clear. Kohn and Sham devised in 1965, an ingenious procedure to avoid the difficult problem of the functional of kinetic energy, the Kohn-Sham (KS) method, which converts the DFT theory into a more practical computational scheme. The idea is based on introducing, in the style of the traditional chemical-quantum methods,

orbitals in the problem and invoking a fictive system of independent electrons whose density is equivalent to that of the real one. The total functional energy can then be decomposed as follows:

$$E[\rho] = T_s[\rho] + \int \rho(\vec{r})v(\vec{r})d\vec{r} + \int d\vec{r}d\vec{r}' \frac{\rho(\vec{r})\rho(\vec{r}')}{|\vec{r}-\vec{r}'|} + E_{xc}[\rho] \quad (2.21)$$

The first term $T_s[\rho]$is the kinetic energy of the non-interacting electrons, although it should be noted that it is functional of the electron density of the interacting electrons. The second term is the energy contribution of the external potential. The third term, which we will call$J[\rho]$, represents the classic Coulomb repulsion of the electronic cloud including the self-interaction energy. The fourth term is called exchange-correlation energy. This term includes the self-interaction as well as the rest of nonclassical effects of the electron-electron quantum interaction: the energy of exchange, the correlation energy and the kinetic energy with respect to the reference system:

$$E_{xc}[\rho] = [T[\rho] - T_s[\rho]] + [U[\rho] - J[\rho] = T_C[\rho] + W_{XC}[\rho] = \int \rho(\vec{r})v_{XC}(\vec{r})d\vec{r}. \quad (2.22)$$

Re-perceiving equation 2.19 in terms of an effective potential $v_{eff}(\vec{r})$we get that:

$$\frac{\delta T_s[\rho]}{\delta\rho(\vec{r})} + v_{eff}(\vec{r}) = \mu \quad (2.23)$$

where the monoelectronic effective potential of Kohn-Sham is defined by:

$$v_{eff}(\vec{r}) = v(\vec{r}) + \int \frac{\rho(\vec{r}')d\vec{r}'}{|\vec{r}-\vec{r}'|} + v_{xc}(\vec{r}) \quad (2.24)$$

With:

$$v_{xc}(\vec{r}) = \frac{\partial E_{xc}[\rho]}{\partial\rho(\vec{r})}. \quad (2.25)$$

Interestingly, if we considered non-interacting electrons moving in an external potential $v_{eff}(\vec{r})$they would generate the same equation 2.22. The problem of minimizing the density $\rho(\vec{r})$ is reduced, then, to solving the monoelectronic Schödinger equation:

$$\hat{h}_{KS}\psi_i = \epsilon_i\psi_i, \hat{h}_{KS} = -\frac{1}{2}\nabla_i^2 + v_{eff}(\vec{r}), \langle\psi_i|\psi_j\rangle = \delta_{ij} \quad (2.26)$$

These equations (called Kohn-Sham equations) are similar to the HF equations. The orbitals that are obtained are called Kohn-Sham orbitals and allow the immediate calculation of the electronic density,

$$\rho(\vec{r}) = \sum_i^N \left| \psi_i(\vec{r}) \right|^2 \quad (2.27)$$

However, the KS orbitals do not simulate the orbitals of the system, nor the KS autovalues are the orbital energies, nor the determinant function $\psi(1, N)$ that we can build with the KS orbitals has explicit relation with the multielectronic function of the real system, nothing more than generating both the same density. In spite of this, the KS orbitals obtained in solid calculations are often very similar to the HF orbitals and have been used in many cases to describe electronic excitations.

As in the HF method, the resolution procedure is self-consistent, due to the dependence of the effective potential with the electron density defined as a function of the occupied spinorbitals $\psi_i(\vec{r})$ through equation 2.26, being in the case of Fock's equations the dependency with the solutions ψ_i explicit of the Coulomb and exchange operators.

The energy of the fundamental state can be extracted from the solutions obtained in the KS equations, through the equation:

$$E_0 = \sum_i \epsilon_i - \frac{1}{2} \int d\vec{r} d\vec{r}' \, \frac{\rho(\vec{r})\rho(\vec{r}')}{|\vec{r} - \vec{r}'|} + E_{xc}[\rho] - \int v_{XC}(\vec{r}) d\vec{r} \quad (2.28)$$

where the sum is over all the occupied states.

This is an exact expression for the total energy. The problem is that we do not know the exact form of E_{xc}. The practical development of DFT is based, then, on finding approximations to the functional E_{xc} sufficiently simple and precise and to the later resolution of the Kohn-Sham equations.

2.3.3. EXCHANGE AND CORRELATION APPROACHES

2.3.3.1. LDA

The oldest approach to the energy of exchange and correlation is due to Kohn and Sham. According to this, $E_{xc}[\rho]$ could be expressed as:

$$E_{xc}[\rho] = \int \rho(\vec{r})\epsilon_{XC}[\rho]d\vec{r} + 0\left(\nabla \left| \rho(\vec{r}) \right|^2\right) \quad (2.29)$$

Considering only the first term of the expansion, the approximation is called the local density approximation(LDA). The functional $\epsilon_{xc}[\rho]$is the energy density of exchange and correlation of a uniform electronic gas, although the constant density of the homogeneous gas (ρ_0) is replaced by the local density ($\rho(\vec{r})$of the interacting and not homogenous real system.

Its extension to magnetic systems leads to the approximation of local spin density ($LSDA$):

$$E_{xc}^{LSDA}[\rho_\alpha(\vec{r}), \rho_\beta(\vec{r})] = \int \rho(\vec{r})\epsilon_{xc}^{LSDA}[\rho_\alpha(\vec{r}), \rho_\beta(\vec{r})]d\vec{r}\,, \quad (2.30)$$

where $\rho_\alpha(\vec{r})$ and $\rho_\beta(\vec{r})$ are the spin densities α and β respectively. The LDA approach ($LSDA$) is, without a doubt, the simplest since it does not consider the nonlocal character of the exchange and correlation functional, $\epsilon_{xc}[\rho]$, therefore, it is a function that depends exclusively on density. To simplify the problem, contributions to correlation and exchange are usually treated separately:

$$\epsilon_{xc}^{LDA}[\rho] = \epsilon_x^{LDA}[\rho] + \epsilon_c^{LDA}[\rho]. \quad (2.31)$$

For the part corresponding to the exchange, the Dirac functional is usually used, while the term of correlation is determined through different interpolation formulas that connect the known limits to the high and low density of ϵ_x. Within the existing parametrizations, in our calculations we have restricted ourselves to the parameterization of the Monte-Carlo results of Ceperley and Alder [10] by Perdev and Zunger [11].

Despite its simplicity, the success of the LDA has been great, even in systems very far from the formal limits of its applicability, that is, in systems with abrupt variations of the electronic density, such as atoms, molecules and even crystals, where the charge density experiences a sharp change in the vicinity of the nuclei. Physically, this is attributed to two facts. In the first place, it satisfies the rule of addition for the hole of exchange and correlation. That is, an electron located in $\vec{r}$ creates a hole around it, a charge deficit, being the charge that displaces exactly the same as that of a positive electron. Second, the energy of exchange and correlation depends only on the spherical average of the gap of exchange and

correlation. Therefore, although LDA does not give the correct form for the gap of exchange and correlation if it provides a spherical average that is very close to the real one.

Despite the obvious successes of this approach in the prediction of macroscopic structures and properties (in general, LDA gives reasonable results for geometries, vibration frequencies and elastic constants), it also has limitations. Among these are the underestimation of the band gap in semiconductors and insulators, the tendency to overestimate the link energy (underestimating the lattice parameters), the erroneous determination of magnetic fundamental states and the treatment of strongly correlated systems and weak van des Waals interactions.

2.3.3.2. GGA

The limitations noted above were attributed to the local character of the exchange-correlation functional. Equation 2.28 suggests a natural method of improvement, through the inclusion of terms of order greater than zero order (corresponding to the LDA approximation) in the Taylor expansion of the exchange and correlation functional versus density. However, the inclusion of the first order gradient of the density in the expansion was a complete failure for atoms and molecules. The origin of the problems was later associated with the fact that the gap of exchange and correlation associated with the truncated expansion of equation 2.28 violated the physical rules that must be met, that is, the rule of addition and the requirement of no exchange gap positivity, if fulfilled in LDA. Despite this, the gradient expansion approximation (GEA) [12] provides the base for the generalized gradient approximation (GGA) [13]. It is a semilocal approach, in which the functional exchange and correlation depends not only on the density of the electrons but also on their local gradients:

$$E_{xc}^{GGA}[\rho] = \int f(\rho_\alpha, \rho_\beta, \nabla_{\rho_\alpha}, \nabla_{\rho_\beta}) d\vec{r}\,, \tag{2.32}$$

Due to the lack of knowledge of the exact form of function f, it is necessary to use approximations. The design of these has sought that the energy of exchange and correlation present an adequate asymptotic behavior and properties of correct scaling, as well as that the rules of addition for the gap of exchange and correlation are not violated.

Within the different approaches, in our calculations we have used Becke's semi-empirical generalized gradient correction to the exchange energy [14], according to which a term of correction is added to the LDA expression for the Slater exchange. The explicit form

of the functional was chosen so that it presented the exact asymptotic behavior of the energy density of exchange and the density of spin. It also includes a parameter that comes from the adjustment of least squares to the exact exchange energy of Hartree-Fock of noble gases calculated with orbitals of the Clementi-Roetti type [15].

Another of the functional used, has been the $PW91$ [16]. In this functional the gap energies of exchange and correlation are those of the expansion to first order of the equation 2.28, including abrupt cutoffs in the real space to eliminate the contributions of long range without physical sense, fulfilling so the rule of sum and the requirement of not positivity for the gap of exchange. Likewise, for the correlation function, a cutoff is introduced into the reciprocal space to force the correlation gap to satisfy its exact sum rule.

For the correlation, the functional Lee, Yang and Parr (LYP) have also been used [17]. This has its origin in the Colle and Salveti model [18] according to which the electronic correlation is obtained by approximating the density of real electron pairs by the density of non-interacting pairs multiplied by a correlation factor that includes the electron density, the density of electron-electron coalescence and the Laplacian density of pairs, together with four constants that fit the Hartree-Fock helium orbitals. Later, Lee, Yang and Parr expressed the density of non-interacting pairs in terms of density and first order density matrix. In this way, the correlation energy can be assigned a form that only involves the electron density and the kinetic energy of the non-interacting system. A gradient expansion of the density of the latter allows expressing the correlation energy as a functional density and its gradient.

These different types of functional have been quite successful in the correlation of some of the deficiencies of LDA. Its main improvements are the correction of the overestimation of the cohesion of the LDA method, generating higher lattice parameters and cohesion energy than that (the overestimation of the compressibility module is of the order of 10% while in the LDA method the underestimation was close to 20%), and the prediction of the correct magnetic fundamental state of certain metals, such as Fe. However, they still present problems in the description of Van der Waals systems.

2.3.3.3. Hybrid methods

These functionals were fundamentally developed in the decade of the 1990s by Becke [19]. The existence of hybrid methods in which an exact exchange is partially included

from a HF calculation can be justified through the adiabatic connection formula for the correlation-exchange energy:

$$E_{xc}[\rho] = \int_0^1 W_{XC}^{\lambda}[\rho] d\lambda \tag{2.33}$$

where $W_{XC}^{\lambda}[\rho]$ is the potential contribution of a system whose bielectronic interaction has been scaled by the parameter λ. $\lambda = 0$ corresponds to the Kohn-Sham system and $\lambda = 1$ to the real physical system. It can be shown that for $\lambda = 0$, $W_{XC}^{\lambda}[\rho]$ is the exact exchange energy, that is, the Hartree-Fock exchange, which justifies the emergence of hybrid methods. Within the existing methods, we have chosen the 3-parameter method of Becke or $B3LYP$ [20], so-called because it includes 3 parameters that fit a set of experimental thermochemical data.

2.3.4. BASIS FUNCTIONS

In both HF and DFT, the effective potential is defined in terms of the solutions ψ_i of the Fock and Kohn-Sham equations, respectively. This common characteristic imposes a self-consistent resolution procedure. If the searched orbitals are expressed as linear combinations of a base $\chi=\{\chi_1,\ldots,\chi_m\}$ of known functions $\psi_i=\sum_{k=1}^{m} \chi_k C_{ki}$, where C_{ki} is an element of the matrix of the coefficients unknown, the system of integrodifferential equations in partial derivatives are transformed into a homogeneous algebraic system:

$$\sum_j [h_{ij} - \epsilon_k S_{jk}] = 0 \tag{2.34}$$

where h_{ij} and S_{jk} are, respectively, elements of the Fock (Kohn-Sham) and overlap matrices and ϵ_k are the eigenvalues.

2.4. ELECTRONIC STRUCTURE IN SOLIDS

2.4.1. CLUSTER-NETWORK APPROACH

Probably, the most intuitive way to approach the study of solids is the application of quantum-mechanical molecular methods. This is the foundation of the approach known as cluster-lattice, according to which the solid is formed by an active part or cluster and is perturbed by the rest of the infinite system. The case limit in which the cluster is reduced to a single center (atom or ion) coupled to the crystalline lattice through a self-consistent quantum-

mechanical cluster-lattice is the origin of the method *ab initio* Perturbed Ion, $aiPI$, [21,22] developed in the laboratory of our research group at the Oviedo University.

This method is based on the Electronic Separability Theory (TSE) of Mc Weeny and Huzinaga [23]. Within this formalism, the HF equations of solids are resolved in a Fock space localized by the division of the crystal into weakly interacting groups, each of which contains an arbitrary number of electrons and a single nucleus. The total wave function is an antisymmetric product of the optimal local wave functions, strongly orthogonal to each other. The energy of system E is given by the sum of the net energies of each group E_{net} and the sum, extended to all possible pairs of groups, of the energy of interaction between them, E_{int}^{R}

$$E = \sum_R E_{net}^R + \sum_R \sum_{S>R} E_{int}^R \tag{2.35}$$

The local wave functions are obtained through the restricted variational principle, that is, by minimizing the effective energy of the group in the field of the crystal lattice. The effective energy of each group A is defined as:

$$E_{eff}^A = E_{net}^A + \sum_{S \neq A} E_{int}^{AS} = E_{net}^A + E_{int}^A \tag{2.36}$$

The second sum is the expected value, in the space of the cluster of an operator that contains the effective potential of the network (nuclear attraction and electronic parts of Coulomb not local exchange) and a projection operator that seeks the fundamental condition of ion-lattice orthogonality. The best ionic wave function is used in the re-computation of the effective potential and the projection operator until self-consistency is achieved. E_{eff}^A contains all the terms of E in which group A intervenes, so that the electronic structure of group A that minimizes both magnitudes is the same. Therefore, to obtain the global minimum it is necessary to successively apply the restricted variational principle to each of the groups, until consistent local wave functions are achieved for all the groups and, consequently, the best total wave function compatible with the initial hypothesis of separability. Although effective group energies are fundamental magnitudes in the TSE, with them it is not possible to regenerate the total energy of the system. To achieve this, the so-called group additive energy is defined, which contains the net energy of the group and half of the energy of interaction with the rest of the groups:

$$E_{add}^A = E_{net}^A + \frac{1}{2} \sum_{S \neq A} E_{int}^{AS} = E_{net}^A + E_{int}^A \tag{2.37}$$

With this definition, the total energy of the system is simply the sum of the additive energies of each group. If the system is assumed to consist of $a$equivalent groups of type$A$, b groups$B$, ..., the total energy of the system will be:

$$E(A_a B_b \ldots) = aE^A_{add} + bE^B_{add} + \ldots \tag{2.38}$$

This is the energy that must be minimized to obtain the optimal geometry of the crystal. The current implementation of the model includes additional hypotheses, for reasons of simplicity and speed of calculation. In the first place, it is required that the quantum mechanical groups maintain the spherical symmetry, characteristic of the free ions, inside the crystal. This approximation is quite restrictive, since the only allowed mode of adaptation of the group to its environment is reduced to the radical relaxation of the density (isotropic deformation). To try to overcome this limitation, a semiclassical model of electronic polarization that considers the existence of dipolar terms has been adapted to this method.

2.4.2. BLOCH'S THEOREM

Another way to approach the study of solids is to explicitly consider the infinite nature and the translational symmetry of these. Both in the HF formalism and in the DFT formalism, it is assumed that the electrons are subjected to an effective monoelectronic potential, which requires translational symmetry. According to Bloch's theorem [24], the eigenstates $\psi(\vec{r})$of a monoelectronic Hamiltonian $\hat{H}(\vec{r}) = \nabla_i^2 + \hat{U}(\vec{r})$, where $\hat{U}(\vec{r}+\vec{R}) = \hat{U}(\vec{r})$for all the vectors $\vec{R}$ of the Bravais lattice, can be written as a product of a plane wave and a function with the periodicity of the lattice:

$$\psi_{n\vec{k}}(\vec{r}) = e^{i\vec{k}\vec{r}} u_{n\vec{k}}(\vec{r}) \tag{2.39}$$

where $u_{n\vec{k}}(\vec{r}+\vec{R}) = u_{n\vec{k}}(\vec{r})$for all vectors $\vec{R}$ of the Bravais lattice. The number n is the band index and labels the independent stations for a given wave vector $\vec{k}$. Since $\psi_{n\vec{k}}(\vec{r})$is periodic because it is the Hamiltonian and $u_{n\vec{k}}(\vec{r})$also, the theorem can also be stated in the form:

$$\psi_{n\vec{k}}(\vec{r}+\vec{R}) = e^{i\vec{k}\vec{R}} u_{n\vec{k}}(\vec{r}) \tag{2.40}$$

Which shows that each vector of the periodic Hamiltonian corresponds to a vector of the reciprocal lattice $\vec{k}$. In the language of band theory, $\vec{k}$ labels one of the infinite, one-dimensional, irreducible representations of the abelian translation group and $\psi_{n\vec{k}}$ is a basic

function of representation. To define the irreducible representation unequivocally, one must limit the value of $\vec{k}$ to the Brillouin zone (BZ), since any vector $\vec{k}'$outside it can be written as $\vec{k}' = \vec{k} + \vec{K}$ where $\vec{k}$ is inside of the BZ and $\vec{K}$ is a vector of the reciprocal lattice, fulfilling that $exp(i\vec{k}'.\vec{R}) = exp(i\vec{k}.\vec{R})$. The introduction of the periodic contour conditions of Born-Von Karman, expressed as:

$$\psi_{n\vec{k}}(\vec{r} + N_1\vec{a}_1 + N_2\vec{a}_2 + N_3\vec{a}_3) = \psi_{n\vec{k}}(\vec{r}) \tag{2.41}$$

where $N_1, N_2, N_1, \vec{a}_1, \vec{a}_2, \vec{a}_3$ correspond respectively to primitive cells and vectors in each dimension of a finite arbitrary crystal $N = N_1N_2N_1$, it leads to the electronic states being allowed only in a certain group of points k of the primitive cell of the reciprocal lattice. The number of these is equal to N the number of unit cells and their density is proportional to the volume of the solid.

Also, the form of $\psi_{n\vec{k}}$ specified by Bloch's theorem transforms the Schrödinger equation:

$$\hat{H}(\vec{r})\psi_{n\vec{k}}(\vec{r}) = E_n\psi_{n\vec{k}}(\vec{r}) \tag{2.42}$$

In the equation of eigenvalues of the periodic function $u_{n\vec{k}}(\vec{r})$:

$$\left[\left(-i\vec{\nabla} + \vec{k}\right)^2 + \hat{U}(\vec{r})\right]u_{n\vec{k}}(\vec{r}) = E_n(\vec{k})u_{n\vec{k}}(\vec{r}) \tag{2.43}$$

This equation is subject to the periodic condition $u_{n\vec{k}}(\vec{r}) = u_{n\vec{k}}(\vec{r} + \vec{R})$, which is equivalent to confining the solutions in a primitive cell of the crystal. In this way, the problem of solving the Schrödinger equation for an infinite system is reduced to that of solving it for a finite volume, that of the primitive cell of the BZ. This confinement implies an infinite set of solutions $u_{n\vec{k}}(\vec{r})$ with eigenvalues $E_n(\vec{k})$ discretely distributed, and which, when containing $\vec{k}$ as a parameter, depend on it in a continuous mode. The fact that $\vec{k}$ appears as a continuous variable does not go against the contour condition of Born-Von Karman, and that at the limit of an infinite lattice (and therefore, also for a finite and macroscopic one), density of points k (the number of which matches the number of solutions) increases, transforming ak into a continuous variable that can take all possible values within the BZ.

Bloch's theorem, then, replaces the problem of calculating an infinite number of electron wave functions by calculating a finite number of electronic functions in an infinite number of points k. The information contained in the functions $E_n(\vec{k})$ is the structure of bands of the crystal. For each value of n, the function $E_n(\vec{k})$is the n band of electronic energy of the system. The periodicity of $E_n(\vec{k})$in the reciprocal space requires that the band have upper and lower limits, that is, that the energy is bounded. The call of the bands is made according to Pauli's exclusion principle. The energy of the highest occupied state is known as Fermi energy and is defined by $N = \int_{-\infty}^{\epsilon_F} D(E)dE$, where N is the number of electrons and $D(E)$ the density of electronic states (DOS) or number of states per unit of energy with energy between E and $E + dE$. The surface of Fermi is the surface of the space k of constant energy and equal to the energy of Fermi, E_F. This surface separates the occupied electronic states from the voids at $T = 0K$. The electronic occupation of the states $|\vec{k}\rangle$,with two electrons of differentm_s, can give rise to two basic types of filling, in the first, a series of bands are completely filled and the rest are empty. An interbanded energetic spacing (bandgap) then arises between the roof of the occupied band of higher energy and the bottom of the empty band of lower energy. This type of filling appears typically in systems with an even number of electrons per primitive cell, since the number of states $|\vec{k}\rangle$ is equal to the number of cells and each $|\vec{k}\rangle$admits two electrons with different m_s. In the second type of filling are partially occupied bands. The Fermi level then appears in the energy range of one or several of these bands. For each partially occupied band, there is a surface in space k that separates the occupied levels from the gaps. The set of these surfaces forms the surface of Fermi.

2.4.2.1 Sampling of points k

The integration of functions of $\vec{k}$ in the first zone of Brillouin is a very important aspect of ab-initio calculations in periodic structures. The problem appears in each cycle of the self-consistent process, when the energy of Fermi is obtained, the density matrix is reconstructed and, after achieving self-consistency, the density of states and the observable quantities are calculated. In principle, it is possible to perform the integration through a standard numerical technique, but in practice this requires the evaluation of the integrand in a very large number of wave vectors, which is linked to a high computational cost. For sufficiently smooth functions, one can take advantage of the fact that the functions do not change appreciably in small distances of space k and approximate the integral by a heavy sum

of values $F(\vec{k})$ in a discrete set K of sample points $\vec{k}_i(i = 1, \dots I)$ carefully selected to ensure convergence. Thus any integrand $f(\vec{r})$ (density, total energy) can be calculated through:

$$\int_{BZ} F(\vec{k}) d\vec{k} = \frac{1}{\Omega} \sum_{j=1}^{I} \omega_j F(\vec{k}_j) \tag{2.44}$$

where $F(\vec{k})$ is the Fourier transform of $f(\vec{r}), \Omega$ is the volume of the cell and ω_j are weight factors. For each Bravais lattice and for each pontual group there are several sets of special points. In our calculations we have chosen the Monkhorst-Pack method [25] to perform the sampling. This method generates a homogeneous distribution of points k through space in rows and columns parallel to the vectors of the reciprocal lattice. The zone of Brillouin is broken down into small polyhedra in the same way as this one. The subdivisions along each vector of the reciprocal lattice necessary to generate this polyhedral decomposition are called contraction factors (S_1, S_2, S_3). In the original scheme, the coordinates of the sample points k with respect to the base vectors $\frac{\vec{b}_1}{S_1}, \frac{\vec{b}_2}{S_2}$ and $\frac{\vec{b}_3}{S_3}$ are given by:

$$\vec{k}_i = \frac{i_1 + \frac{1}{2}}{S_1} \vec{b}_1 + \frac{i_2 + \frac{1}{2}}{S_1} \vec{b}_1 + \frac{i_3 + \frac{1}{2}}{S_3} \vec{b}_1 ; \qquad 0 \leq i_j < S_j \tag{2.45}$$

which is equivalent to placing a single point k in the center of each polyhedron. The set K contains $I = S_1 S_2 S_3$ elements. It is convenient that the contraction factors be multiples of 2 or 3, according to the order of the main axis of the crystalline punctual group. The number of non-equivalent sampling points is obtained by dividing I (product of contraction factors) by the order of the punctual group. In systems of high symmetry it can be considerably smaller, because many points are placed on planes or axes of symmetry. In the selection of K for non-centrosymmetric crystals, the symmetry $E_n(\vec{k}) = E_n(-\vec{k})$ is exploited. All this produces a small subset of the set K, with points located in the irreducible part of the BZ. The values of the weight factors are adjusted according to this set of points k. This leads to a reduction in the time of calculation.

In the case of non-cubic cells, the estimation of the values of the contraction factors must also take into account the dimensions of the vectors in the real lattice. Thus, the smallest vector in the real network corresponds to the largest vector in the reciprocal network and therefore, to a contraction factor necessarily greater than that of the other two reciprocal lattice vectors. The grid of points k must belong to the same kind of lattice of bravais as the

BZ. Moreover, the symmetry of the grid k can lead to grids that cannot be divided into polyhedra (at least by the conventional division schemes implemented in the calculation programs). This occurs, for example, in certain Bravais lattices with low symmetry. One possible solution is to center the Monkhorst-Pack grid on $\Gamma(k = 0)$, such that the coordinates of the sample points $\vec{k}_i$ with respect to the base vectors $\frac{\vec{b}_1}{S_1}, \frac{\vec{b}_2}{S_2}$ and $\frac{\vec{b}_3}{S_3}$ are given by:

$$\vec{k}_i = \frac{i_1}{S_1}\vec{b}_1 + \frac{i_2}{S_1}\vec{b}_1 + \frac{i_3}{S_3}\vec{b}_1 ; \qquad 0 \leq i_j < S_j \tag{2.46}$$

This is, for example, necessary in the hexagonal cells, in which the grids generated according to the original Monkhorst-Pack scheme do not have total hexagonal symmetry. It is also possible to carry out other displacements of the grid of points k, but in our calculations we have not used them. Choosing a grid of sufficiently dense points is crucial for the convergence of results and is, therefore, one of the main objectives when conducting convergence tests. However, it is also necessary to point out that there is no variational principle that governs the convergency with respect to the grid of points k, so that the total energy does not necessarily show a monotonous behavior when the density of points k increases. For insulators, 100 k points per atom in the total BZ are, in general, sufficient to reduce the energy error to less than 10 meV. The metals require 1000 (including 5000 some transition metals) points k to obtain the same precision. These numbers are considerably reduced in the irreducible part of the $BZ(IBZ)$. In fact, the precision of the grid is normally directly proportional to the number of points k in the IBZ, but not to the number of divisions.

The previous procedure allows integrations of well-behaved functions (with Fourier transform that decay rapidly in real space) over the first Brillion zone by selecting sampling points in the reciprocal space. This does not pose problems in semiconductors and insulators, but in metals, where it is necessary to integrate the Fermi distribution function, discontinuous when $E = E_F$ and with Fourier transform not located in real space. We want to evaluate:

$$\bar{f} = \frac{1}{\Omega_{BZ}} \int \Theta(E_F - E(\vec{k}))f(\vec{k})d\vec{k} \tag{2.47}$$

where E_F is the Fermi energy and $\Theta(x)$ is the Dirac step function. In accordance with the sampling techniques:

$$\bar{f} = \sum N_K \, \omega_i \Theta(E_F - E_n(\vec{k}_i)) \tag{2.48}$$

This sum converges very slowly with the number of points k, except in semiconductors and insulators where the bands are completely full or empty and the recording of the band index n is limited to the occupied bands. Moreover, with a small change in the value of the E_F, a point k can enter or leave the surface of Fermi, resulting in a discontinuous change of the values of $\bar{f}$. This pathology can create a numerical instability in the self-consistent process of the electronic structure codes. A method to avoid these problems is the linear tetrahedron method [26], in the term $E(\vec{k})$ is linearly interpolated between two points k. Blöchl [27] eliminated the quadratic errors of the method and assigned effective weights for each band and point k. This method was, in general, chosen in semiconductors and insulators, and for calculations of total energy without relaxation in metals.

In the study of relaxation in metals, it is opted for approximations of fictive temperature. Among these are the smearing methods [28], in which the step function of Dirac is replaced by a function $f(\{E_n(\vec{k})\})$ soft (Dirac, Gaussian function). In these, it is necessary to replace the total energy with the generalized free energy $F = E - \sum_{n\vec{k}} \omega_{\vec{k}} \sigma S(f_{n\vec{k}})$, so that the calculated forces are now derived from this free F. According to the Fermi-Dirac statistics, free energy could be interpreted as the free energy of electrons at finite temperature = $k_B T$, but the physical meaning is not the case of Gaussian smearing. Despite this problem, it is possible to obtain a precise extrapolation for $(\sigma \rightarrow 0) = E_0 = \frac{1}{2}(F + E)$. In this way, we obtain a 'physical' quantity of a calculation at finite temperature.

However, two problems appear. In the first place, the forces calculated by the computational programs are derived from the free electronic energy, F. Therefore, they can not be used to obtain the fundamental state of equilibrium, corresponding to the minimum energy. In spite of this, the error in the forces is generally small and adaptable. Second, the parameter σ must be chosen carefully. If σ is large the integral in the BZ converges with a small number of points k, but in general leads to an erroneous result. If σ is smaller, the integral tends to the correct result but to express of a greater number of points k. The only way to obtain a good σ is to perform several calculations with different grid of points k and different values forσ. These problems can be solved by adopting a slightly different form for $f(\{E_n(\vec{k})\})$. This is possible by transforming the step function into a complete orthonormal set of functions (Methfessel and Paxton method) [29]. The Gaussian function is the first approximation ($N = 0$) to the step function. Subsequent approximations ($N = 1,2$) are easily

obtained. As with the Gaussian method, energy is replaced by free energy, but, unlike the Gaussian term, the entropic term is small for reasonable values of σ and gives an estimate of the error between free energy and physical energy ($E(\sigma \rightarrow 0)$). In this way σ is increased until the error takes a certain value.

2.4.2.2 Basis functions

As previously mentioned, it is necessary to express the orbitals as a linear combination of a known basis of functions. Thus, the crystalline orbitals $\psi_{n\vec{k}}(\vec{r})$ are expressed as a linear combination of Bloch functions, so that the generated orbital $\psi_{n\vec{k}}(\vec{r}) = \sum_{\mu} c_{\mu\vec{k}}\, \Phi_{\mu\vec{k}}(\vec{r})$ also satisfies the Bloch theorem and therefore reflects the translational periodicity of the system. There are two basic types of Bloch functions (BFs) used in the expansion.

First, functions located in the positions of the nuclei (χ_{mu}):

$\Phi_{\mu\vec{k}} = \frac{1}{V}\sum_{\vec{R}} e^{i\vec{k}\vec{R}}\chi_{\mu\vec{R}}(\vec{r} - \vec{r}_{\mu} - \vec{R})$, where $\vec{r}_{\mu}$ is the position value of the atom μ with respect to the origin of its cell and $\vec{R}$ the vector of the Bravais lattice corresponding to the origin of the cell. The generating functions $\chi_{\mu\vec{R}}(\vec{r} - \vec{r}_{\mu} - \vec{R})$are centered on the atomic nuclei, hence they are called atomic orbitals (AOs). Normally, AOs are expressed as a linear combination of GTOs, with preference over STOs due to their analytical properties, despite the fact that they imply a bad description of nuclear cuspids. Likewise, each GTO is expressed as a linear combination of Gaussians centered on the same nucleus and with identical quantum angular numbers. In this context, Gaussians are called primitive functions and AOs are contracted functions. The use of such contracted sets allows to reduce the number of basic functions to build a given crystalline orbital (OC), especially when considering the more internal ones, which have to simulate the core AO s. However, and as a counterpart to its chemical suitability, this basic choice has four undesirable characteristics: (i)-it is not a universal set, in the sense that it depends on the positions of the atoms in the unit cell and their nature, (ii)-it does not form orthogonal sets, and the overlapping terms must be included explicitly in the calculation, (iii)-despite its incompleteness, linear pseudo-dependence problems can be generated between the most diffuse valence AOs and (iv)-it does not reproduce the self-functions monoelectronics of free electron gas and, therefore, there are justified doubts in their use in metals.

Second, plane waves: $\Phi_{\vec{K}\vec{k}}(\vec{r}) = e^{i\vec{r}(\vec{k}+\vec{K})}$. Plane waves are the ideal base functions for the study of periodic systems. They constitute a universal set (they do not depend on the naturalization of the atoms or their position in the unit cell), orthonormal, with correct asymptotic behavior and, in principle, complete. Since the use of an infinite set of plane waves in the expansion of the electronic wave functions is impossible, a cutting or cutoff energy is introduced that truncates the base of plane waves, in such a way that the plane waves with kinetic energy $(\frac{1}{|\vec{k}+\vec{K}|})$ greater than the cutting energy are excluded from the base. The truncation leads to an error in the total energy.The value of the cutting energy must, therefore, be increased until the convergence in the total energy is reached. One of the difficulties associated with the use of a plane wave base is that the number of base deaths changes discontinuously with the cutting energy for the different points$k$. Furthermore, at a fixed cutting power, the change in the size and/or shape of the unit cell also causes discontinuity in the base. One method to solve this problem is to use a denser grid of points k, so that the weight associated with the base functions is smaller. The plane waves involve a very simple algebraic treatment, being convenient to perform the calculations in the representation of moments. However, they present a serious problem when a large number of plane waves are necessary to reproduce the local waveforms, specifically the cusps in the nuclear positions. The most usual way to overcome it is to perform a core-valence separation. In this sense, the electrons of the core are described by pseudopotentials and those of valence by a sum of plane waves.

2.5. COMPUTATIONAL METHODS

2.5.1. LINEAR COMBINATION OF ATOMIC ORBITALS ($LCAO$)

The term $LCAO$ means that each crystalline orbital is a linear combination of Bloch functions defined in terms of local functions (atomic oribitals). Within this approach and under the HF formalism the $CRYSTAL$ program [30] is suitable for calculations.

In this, and as has been mentioned in the previous section, atomic orbitals are, in turn, mixtures of Gaussian-type functions, called primitives, whose exponents and coefficients are defined in the input. The atomic orbital belonging to a given atom are grouped in shells. Each shell contains all the OAs with equal $n\ and\ l$ quantum numbers (shells 3s, 2p, 3d) or all

OAs with the same main quantum number n, if the number of GTOs and their corresponding exponents are the same for all of them (sp shells) .

The expansion coefficients of the Bloch functions $c_{\mu n\vec{k}}$ are obtained by independent resolution of the Hartre-Fock matrix equations at each point $\vec{k}$ of the first Brillouin zone:

$$F(\vec{k})C(\vec{k}) = S(\vec{k})C(\vec{k})E(\vec{k}), \tag{2.49}$$

where $S(\vec{k})$ is the matrix overlapping between Bloch functions, $E(\vec{k})$is the diagonal energy matrix and $F(\vec{k})$ is the Fock matrix in the reciprocal space: $F(\vec{k}) = \sum_{\vec{R}} F^{\vec{R}} e^{i\vec{k}\vec{R}}$.

This is possible thanks to the structure in diagonal blocks of the matrices (the matrices between crystalline orbitals that differ in $\vec{k}$ are null according to the Bloch theorem). The dimensions of the matrices are equal for each $\vec{k}$ and equal to the number of atomic orbitals in the elementary cell. The matrix elements of $F^{\vec{R}}$, the Fock matrix in the direct space, can be written as a sum of monoelectronic and bielectronic contributions in the base of AOs:

$$F_{\mu\nu}^{\vec{R}} = H_{\mu\nu}^{\vec{R}} + B_{\mu\nu}^{\vec{R}} \tag{2.50}$$

where the monoelectronic contribution includes the kinetic terms and the nuclear attraction $H_{\mu\nu}^{\vec{R}} = T_{\mu\nu}^{\vec{R}} + Z_{\mu\nu}^{\vec{R}}$ and the term bielectronic is the sum of the contributions of Coulomb and exchange $B_{\mu\nu}^{\vec{R}} = C_{\mu\nu}^{\vec{R}} + X_{\mu\nu}^{\vec{R}}$. The Coulomb interactions are individually divergent, since the summations on vectors of the direct lattice include infinite terms. It is necessary, therefore, to group the different contributions to eliminate the divergence. The exchange integrals that are combined with small elements of the density matrix are suppressed. Threshold parameters are also introduced for the overlap between the contracted GTOs with the object of truncating the summations. This approach introduces very severe restrictions on the number and spatial extent of the basic functions used. For this reason, high-quality molecular bases cannot be used in $CRYSTAL$ calculations, and medium or low quality bases must be adopted whose more diffuse exponents, especially in the case of anions, have to be reoptimized in each crystal. The elements of the density matrix in the direct space and in the base of AOs are calculated by integrating on the volume of the first zone of Brillioun:

$$P_{\mu\nu}^{\vec{R}} = \frac{1}{\omega_B} \int_{\Omega_B} e^{-i\vec{k}\vec{R}} d\vec{k} \sum_i a_{\mu i}^*(\vec{k}) a_{i\nu}(\vec{k}) \Theta(E_F - E_i(\vec{k})) \tag{2.51}$$

where the sum extends to the i eigenvalues. The total electronic energy per cell, not including the term of internuclear repulsion, can be written in terms of the density matrix as:

$$\varepsilon=\frac{1}{2}\sum_{\vec{R},\nu,\mu} P_{12}^{\vec{R}}\left(H_{12}^{\vec{R}}+B_{12}^{\vec{R}}\right) \tag{2.52}$$

To calculate the Fermi energy and the density matrix, Monkhorst-Pack grids are used. In the case of metals, denser grids (Gilat grids) [31] are used, with an analogous definition to the first ones. The new subdivisions divide the first Brillion area into mini-cells. In them, linear or quadratic interpolations are made for the periodic functions in $\vec{k}$, so that the integral is calculated approximately as a sum of integrals over the individual.

2.5.2. PSEUDOPOTENTIAL-PLANE WAVES METHOD (*PP-PW*)

As previously discussed, wave functions can be represented on a plane wave basis:

$$\psi_{i\vec{k}} = \sum_K c_{n\vec{k}}(C)\, e^{i(\vec{k}+\vec{K})\vec{r}} \tag{2.53}$$

where the sum recovers the vectors of the reciprocal lattice $\vec{K}$ and the $c_{n\vec{k}}(\vec{K})$ are the expansion coefficients. The substitution of Equation 3.53 in the Kohn-Sham equations leads, after its integration, to the secular equation:

$$\sum_K\left[\left|\vec{k}+\vec{K}\right|^2\delta_{\vec{K}\vec{K'}}+v\left(\vec{K}-\vec{K'}\right)+v_H\left(\vec{K}-\vec{K'}\right)+v_{xc}\left(\vec{K}-\vec{K'}\right)\right]c_{n,\vec{k}+\vec{K'}}=\epsilon_n c_{n,\vec{k}+\vec{K'}} \tag{2.54}$$

According to this expression, the representation in the reciprocal space of the kinetic energy is diagonal and the different potentials (local in real space) can be described in terms of their Fourier transforms. Fourier transformations can be done very efficiently with the *FFT* technique (Fast Fourier Transform), which reduces the computational cost of the calculation to $M\log M$ (M = number of plane waves in the base). The traditional methods to solve the Kohn-Scham equations are based on the diagonalization of the Hamiltonian matrix whose elements $H_{\vec{k}+\vec{K},\vec{k}+\vec{K'}}$ are given by the terms in the brackets from equation 2.54. The size of the matrix is determined by the cutoff energy $\frac{1}{2\left|\vec{k}+\vec{K}_c\right|^2}$ and is enormous, even in the simplest systems. Therefore, it is necessary to resort to the approximation of the pseudopotential and to the application of numerical techniques different from the conventional diagonalization techniques.

2.5.2.1. Pseudopotentials

The computational cost derived from the inclusion of all the electrons of a system is prohibitive using a plane wave base. The rapid oscillations of the functions of valence waves in the region near the nucleus, originated by the orthogonality condition with the wave functions of the core, according to the principle of exclusion, and the fact that the electron-nucleus potential varies as $-\frac{1}{r}$, so that it diverges when $r \rightarrow 0$ leads to large kinetic energies, and therefore makes a large number of plane waves necessary. Furthermore, describing the core wave functions also requires a large number of plane waves.

These problems can be avoided by using the pseudopotential approach. This arises from two observations from the study of the chemical-physical properties of matter. First of all, the core electrons of different atoms are not, to a large extent, affected by the surrounding environments. Second, only valence electrons participate actively in the interactions between atoms. Therefore, most of the observable properties are determined by the valence electrons. For a large number of atoms, there is a clear distinction between the electrons that can be considered part of the core, and the valence electrons that determine the atomic characteristics. Even if it is not, a reasonable division is possible.

The pseudopotential approach substitutes the strong Coulomb potential and the core electrons for an effective pseudopotential that is much weaker, and the valence wave functions, which oscillate rapidly in the core region, for pseudo-wave functions, which vary more smoothly in the core region and coincide with the real wave functions outside the core region. This reduces the complexity of the problem. First, by not considering the core electrons explicitly, the number of wave functions to be calculated is smaller. Second, since the potential no longer diverges to $-\infty$ and the valence wave functions are softer within the core region, fewer plane waves are needed to describe the valence wave functions.

The introduction of pseudopotentials appears as a natural development of the orthogonalized plane wave method. If we describe the electronic structure of the atom through the monoelectronic Hamiltonian $\hat{h}$, we can write the equations of eigenvalues in the form:

$$\hat{h}|v\rangle = e_{\mathrm{v}}|v\rangle \hat{h}|c\rangle = e_{\mathrm{c}}|c\rangle \tag{2.55}$$

where $|v\rangle$ and $|c\rangle$ are, respectively, valence and core electronic states and e_c and e_v their corresponding eigenvalues. Since $|v\rangle$ do not contain core contributions, we can construct a softer base pseudostate $|v\rangle$ defined by:

$$|v\rangle = |\bar{v}\rangle - \sum_c |c\rangle \langle c|\bar{v}\rangle \tag{2.56}$$

if we act with the effective monoelectronic Hamiltonian on transformation equation 2.56, we find,

$$[\hat{h} + \sum_c |c\rangle (e_v - e_c)\langle c|]|\bar{v}\rangle = e_v|\bar{v}\rangle \tag{2.57}$$

which shows that the transformed vectors $|v\rangle$are eigenvectors of the transformed Hamiltonian $\hat{h}^T = \hat{h} + \sum_c |c\rangle (e_v - e_c)\langle c|$, with identical eigenvalue to which they have the true $|v\rangle$with $\hat{h}$. The additional potencial $\hat{V}_{nl} = \sum_c |c\rangle (e_v - e_c)\langle c|$, whose effect is located in the core, is repulsive since $e_v - e_c > 0$and cancels part of the strong attractive Coulomb potential $\hat{V}(\vec{r})$ resulting in a softer pseudopotential $\hat{V}_{PP}(\vec{r},\vec{r}') = \hat{V}(\vec{r}) + \sum_c |\psi_c(\vec{r})\rangle (e_v - e_c)\langle\psi_c(\vec{r}')|$. Since the wave functions of core $|c\rangle$ are exhausted at relatively small distances from the nucleus, the pseudo-wave valence functions $|v\rangle$ suffer, at higher distances, a very similar nominal potential $\hat{V}(\vec{r})$ and result, in that range of distance, very similar to the true wave functions $|v\rangle$. At smaller distances, the valence wave pseudo-functions $|v\rangle$ suffer a Coulomb potential screened by the core components. This shielding is responsible for the non-singularity of the pseudopotential $\hat{V}_{PP}(\vec{r},\vec{r}')$ at the origin.

Pseudopotentials *norm-conserving*

There is no single procedure for the construction of pseudopotentials, although a valid pseudopotential should be transferable, smooth and the pseudo-wave function should generate identical charge density to that of the real wave function outside the region of core with the object to obtain a correct description of the exchange and correlation terms. The transferability of the pseudopotential indicates its ability to describe valence electrons in different chemical environments, while the softness of the pseudopotential is related to the inclusion of few plane waves in the expansion of the valence wave pseudo-functions, so that the cost computational data associated with the calculation is as low as possible. Therefore, traditionally its generation has been guided by the fulfillment of four properties:

▪ The eigenvalues of the pseudo-wavefunction and the all-electron wavefunction must coincide for a given atomic configuration.

▪ The pseudo-wavefuncion must be equal to the all-electron wavefunction from a radius of core r_c .

▪ The charge within r_c must be equal for the two wave functions (conservation of the norm). This condition guarantees the coincidence of the all-electron wavefunction and the pseudo-wavefunction outside the core region.

▪ The logarithmic derivatives of the pseudo-wavefunction and the all-electron wave function and their first derivatives with the energy must coincide for $r > r_c$.

The last two properties are fundamental to ensure the transferability of the pseudopotential in a variety of different chemical environments. The third property guarantees that the Coulomb interaction between the atoms is calculated correctly, since the correct core charge is available. For its part, the fourth property ensures that the effect of scattering (derived from logarithms) is the same as the original potential in the proximity of eigenvalues (although, in general, occurs throughout the energy interval of the valence bands). Both properties are related by a simple identity and the generated pseudopotentials are called norm-conserving. Usually, the procedure for generating pseudopotentials consists of a series of steps:

▪ Obtaining the all-electron solution of the free atom.

▪ Choice of a cutting radius r_c , from which the pseudo-valence wave function and the pseudopotential coincide with the wave function of real valence and potential. The choice is determined by the compromise between transferability (lower r_c) and smoothness (greater r_c). In general, to obtain good reproducibility of the charge distribution, and therefore a good transferability, r_c should be close to the maximum of the all-electron wave function, which for elements with orbitals strongly localized leads to huge bases of plane waves.

▪ Parametrization of the wave function in$r < r_c$ requiring a softjunction in r_c with the all-electron wave function and the conservation of the norm.

▪ Inversion of the Schrödinger equation to obtain the pseudopotential that reproduces the pseudowavefuncion.

▪ Unscreening by subtracting Hartree's contributions and exchange-correlation.

▪ Verification of transferability and smoothness.

The wave functions and eigenvalues are different for different angular moments, which implies that the pseudopotential must also depend on the angular momentum. In general, we can express the non-local pseudopotential in the semilocal form:

$$\hat{V}_{ps} = \hat{V}_{loc} + \sum_l \sum_{m=-l}^{l} |lm\rangle \delta\hat{V}_l \langle lm| \tag{2.58}$$

where $|lm\rangle$ denotes the spherical harmonic Y_{lm}. The choice of the local potential $\hat{V}_{loc}$ is arbitrary, but in general the sum over l is truncated to a small value (for example, l = 2) in such a way that the local part represents the potential that acts on components at the moment angular greater. $\delta\hat{V}_l$ is the angular momentum component l of the pseudopotential acting on the wave function. It is a semilocal term, which is given by: $\delta\hat{V}_l = \hat{V}_{ps,l} - \hat{V}_{loc}$. This form presents the problem of being very costly computationally, since the number of elements of the matrix goes with the square of the number of basis functions. The most common solution to this problem is the use of the separable form of Kleinmen-Bylander (KB) [32], in which the semilocal term is transformed into a non-local separable term:

$$\hat{V}_{KB} = \hat{V}_{loc} + \sum_{lm} \frac{|\delta\hat{V}_l \Phi_{lm}\rangle\langle\Phi_{lm}\delta\hat{V}_l|}{\langle\Phi_{lm}|\delta\hat{V}_l|\Phi_{lm}\rangle} \tag{2.59}$$

where $|\Phi_{lm}\rangle$ is an eigenfunction of the atomic pseudo-Hamiltonian calculated with $\delta\hat{V}_l$.

This operator acts on a state of reference in a way identical to the original semi local operator $\hat{V}_{ps}$, but the number of projections scales only linearly with the number of basis functions. An artifact of the non-local form of KB is the appearance of ghost states without physical sense close to valence states with physical sense. Formally, the KB form can be generalized to a serial expansion of a non-local pseudopotential that avoids ghost states by projection in additional reference states. In practice, it is possible to achieve transferable pseudopotentials without ghost states through a correct choice of the local component of the potential and r_c.

An alternative to the pseudopotential type KB are the pseudopotential HGH [33], which we have used in our calculations. Its form is analytical, so it is not necessary to store the projectors in numerical form in dense radial grids (as in the KB type pseudopotentials),

but only a small number of parameters need to be specified. They consist of a local part and a nonlocal contribution. The nonlocal part is a sum of separable terms that include projectors with the product form of a Gaussian by a polynomial. A characteristic property of these pseudopotentials is that the same form is maintained in the reciprocal space. Because of this, pseudopotentials have optimal decay properties in both real and reciprocal space, which allows the nonlocal potential to be located in a small region around the atom and the pseudopotential to be reasonably smooth, avoiding the use of a very narrow grid dense, respectively.

The construction procedure differs from the traditional method, since the pseudopotential parameters are determined through a setting of least squares, in which the function to be minimized includes the differences of eigenvalues and charges within an atomic sphere of the atom all electron and the pseudoatom, instead of producing pseudo-wavefuntions identical to the electron beyond r_c . These pseudopotentials also allow the explicit consideration of semiconductor electrons, although the precision required for the eigenvalues and the charges of the pseudo-wavefunctions is smaller than that of the pseudo-valence wave functions. The use of pseudopotentials with semiconductor wave functions, despite the greater computational cost associated with containing a greater number of electrons, is very important in those systems in which there is a non-negligible overlap between the wave functions of core and valence. Another way used in other pseudopotentials to solve the problem is the inclusion of non-linear core corrections, which consider the contribution of the core charge to the potential for exchange and correlation.

Pseudopotentials *ultasoft* **(US)**

The determination of the r_c of an arbitrary pseudopotential is governed by two general rules. First, to allow an adequate representation of the logarithmic derivatives, it should not exceed the value of half the distance between first neighbors d_{NN} :

$$r_{c,max} \approx \frac{1}{2} d_{NN} \tag{2.60}$$

Secondly, and only for the norm-conserving pseudopotentials, the spatial region where the real solutions are replaced by pseudo-solutions has to be restricted to a region where the Hamiltonian remains close to the reference Hamiltonian for any chemical environment, since the equation 2.60 together with the rule conservation requirement, only

guarantees a correct description of the logarithmic derivatives of the wave functions for the Hamiltonian, or reference. The general recommendation is that the peak of highest charge density associated with a certain orbital, this is the most external maximum of the all electron wave function should be reproduced correctly, so:

$$r_{\mathrm{c,max}} \approx R_{ext} \tag{2.61}$$

where R_{ext} is the value of the radius for the most external maximum of the wave function. Equation 2.61 leads to the existence of strong limitations for the description of systems with strongly localized orbitals ($3d$ transition metals, rare earths with f orbitals) since in these cases R_{ext} is significantly smaller than 0.5 d_{NN} , which makes a large number of plane waves per atom (a $<r_c>K_c$). The calculation is also expensive in systems that combine large atoms with small atoms (elements of the first row), since the R_{ext} of the latter can be significantly smaller than 0.5 d_{NN} (for example, molecular phases of N, O).

The main idea of the ultrasoft pseudopotentials proposed by Vanderbilt in 1990 [34], is that the relaxation of the conservation requirement of the standard can be used to generate much smoother potentials, so that the size of the plane wave basis set can be substantially less. In this scheme, the forms of the pseudo-wavefunctions are forced to be equal to the all electronfunctions out of r_c (like the concept of conservation of norm) but they are allowed to be much softer inside, as a consequence of the elimination of the requirement of the norm. As the fulfillment of the equation 2.61 is not necessary, r_c can be considerably greater, which reduces the number of plane waves needed in the calculation.

With the elimination of the requirement of conservation of the norm, the problem of standard eigenvalues:

$$\left(\hat{T} + \hat{V}_{LOC} + \hat{V}^{NL} - \epsilon\right)|\Phi\rangle = 0 \tag{2.62}$$

where T is the kinetic energy operator, $\hat{V}_{LOC}$ and $\hat{V}^{NL}$ the local and non-local components of the pseudopotential, ϵ the eigenvalue and $|\Phi\rangle$ the pseudofuncion of angular momentum lm, is transformed to generalized eigenvalues problem:

$$\left(\hat{T} + \hat{V}_{LOC} + \hat{V}^{NL} - \epsilon S\right)|\Phi\rangle = 0, \tag{2.63}$$

in which an overlapping operator appears as a consequence of the use of non-orthogonal wave functions:

$$S = 1 + \sum_{ij} Q_{\mathrm{i,j}} \, |\beta_j\rangle\langle\beta_j| \tag{2.64}$$

in such a way that the normalization of the solutions in the generalized problem takes the form:

$$\langle \Phi_{n\vec{k}} | S | \Phi_{n'\vec{k}} \rangle = \delta_{nn'} \tag{2.65}$$

On the other hand, the expression for the totally separable non-local pseudopotential is:

$$\mathrm{V}'_{NL} = \sum_{ij} D_{i,j} \, |\beta_j\rangle\langle\beta_j| \tag{2.66}$$

The functions of increase $Q_{i,j}(\vec{r})$ are given by:

$$Q_{i,j}(\vec{r}) = \psi_i^*(\vec{r})\psi_j(\vec{r}) - \Phi_i^*(\vec{r})\Phi_j(\vec{r}) \tag{2.67}$$

where $\psi_i(\vec{r})$ and $\Phi_i(\vec{r})$ are the all electron wave functions and ultrasoft, respectively. Therefore, the conservation requirement of the standard $Q_{i,j}(\vec{r}) = 0$ is eliminated and the only restriction is that the pseudo-wavefuntions are continuous and with first and second derivatives equal to those of the all electron wavefunctionin r_{c} . $|\beta_j\rangle$ are localized projectors, dual to $|\Phi_i^{US}\rangle$, $\langle\beta_j|\Phi_i^{US}\rangle = \delta_{ij}$ and the coefficients $D_{i,j}$ determine the importance of each contribution in V'_{NL}. It opens the possibility to the use of more than one reference energy ϵ by quantum state l (in general, the number of projectors is reduced to two) in the construction of ultrasoft pseudopotentials, which guarantees good transferability of them in a specified energetic range even at r_{c} large. Another important aspect is the electron density deficit of valence that appears in the core region, as a consequence of the elimination of the requirement of conservation of the norm in the construction of the pseudo-wavefunction. Thus, in the self-consistent calculation, the electron density originated by the square of the modulus of the pseudo-wavefunctions has to be increased in the region of core, in order to recover the total density. The electronic density appears subdivided, then, in a smooth contribution that extends throughout the unit cell and a hard contribution located in the regions of core, according to the expression:

$$\rho_v(\vec{r}) = \sum_{n\vec{k}} \Phi^*_{n\vec{k}}(\vec{r})\, \Phi_{n\vec{k}}(\vec{r}) + \sum_{i,j} \rho_{i,j} Q_{i,j}(\vec{r}) \qquad (2.68)$$

where

$$\rho_{i,j} = \sum_{n\vec{k}} \langle \beta_i | \Phi_{n\vec{k}} \rangle \langle \Phi_{n\vec{k}} | \beta_j \rangle \qquad (2.69)$$

To calculate the increase part of the charge density (second term in equation 2.68) it is convenient to substitute the $Q_{i,j}(\vec{r})$ for the functions $Q^{PS}_{i,j}(\vec{r})$. To do this, all electron functions in equation 2.67 are replaced by norm-conserving function homologs $|\Phi_{NC}\rangle$.

The main advantage of the ultrasoft pseudopotential scheme, although mathematically more complicated, is evident from equation 2.68. The pseudo-charge defined by the ultrasoft wave functions lacks physical significance, being the only relevant quantity the total electronic density obtained after the increase. For this reason, the 2.61 restriction is only relevant for the norm-conserving wave function that defines the increase of charges. For the ultrasoft wave pseudofunction, the only restriction is 2.60. From this expression it is also deduced that the quality of the calculation will be determined by the presence of charges of high quality increase, that is, with r_c sufficiently small.

In the construction scheme of pseudopotentials of type *RRKJ* [35], the pseudo-wavefunctions belonging to an angular momentum l and energy ε are expanded in spherical Bessel functions within the region of the core defined by the radius $R_{ps}(r \leq R_{ps})$

$$\Phi^{PS}_{l\epsilon}(\vec{r}) = \sum_{i=1}^{n} \alpha_i\, r_{jl},\ (q_{ir}) \qquad (2.70)$$

where wave vectors q_i are chosen in such a way that the Bessel functions have the same logarithmic derivatives in $r = R_{ps}$ that the wave functions all electron:

$$\frac{\partial}{\partial r}[Ln\Phi^{AE}_{l\epsilon}(\vec{r})]|_{r=R_{ps}} = \frac{\partial}{\partial r}\{Ln[r_{jl}(q_{ir})\}|_{r=R_{ps}} \qquad (2.71)$$

The expansion coefficients α_i are determined according to the requirement that the wave function is continuously differentiable up to order 2 and without nodes. The basis of function of Bessel presents the advantage of being orthogonal and for $(r \rightarrow \infty)$ complete.

This scheme is used both in the construction of the ultrasoft wave functions and in the norm-conserving functions, with which R_{ps} is identified with the cutting radius of each of them. In the model used, two functions of Bessel for the construction of ultrasoft wave

functions are produced, extending the number to 3 (even to 4) in the norm-conserving wave functions, in order to guarantee compliance with the conservation of the rule.

2.5.2.2. Electronic minimization

The traditional procedure to perform a calculation of total energy under the approximation of the pseudopotential begins with the determination of the electron-electron potential and the construction of the Hamiltonian matrices for each of the points k included in the calculation (assuming equation 2.54) from an electronic density test. Diagonalize, then, the Hamiltonian matrices and lower eigenvectors in energy are occupied. These eigenvectors will, in principle, generate a charge density and electron-electron potential different from the initial ones, so that the process is repeated until it reaches self-consistency. In practice, the new density (or the new potential) is not simply the density (potential) generated in the previous iteration, but it is necessary to perform an averaging of the densities (potentials) of input and output to avoid oscillations in the process. According to this original scheme, the maximum number of plane waves in the calculation is restricted to 1000, as a consequence of the limitation of memory and computational speed, so taking into account that to represent the orbitals in a calculation of this type it is needed a number of 100 plane waves per atom, a system of 10 atoms represented the largest system to treat.

It is necessary, therefore, to resort to iterative algorithms, in which the explicit calculation and storage of the Hamiltonian matrix $(N_{plw}.N_{plw})$ (N_{plw}= number of plane waves) is avoided, allowing the use of very large bases ($N_{plw} \approx 10000$).

They are distinguished within these:

1. Methods to determine the minimum energy functional of Kohn-Sham directly (direct methods).

2. Iterative methods for the diagonalization of the Hamiltonian KS in conjunction with an iterative (mixed) improvement of the charge density (SC methods).

The direct methods were proposed by Car and Parrinello [36] and are based on the fact that the functional Kohn-Sham (E_{KS}) is minimal in the electronic ground state, so the minimization with respect to the degrees of vibrational freedom leads to a suitable scheme for

the calculation of the electronic ground state. Its biggest problem lies in the difficulty in maintaining orthogonal wave functions.

In contrast to the direct methods, the SC methods [37] divide the problem of the evaluation of the fundamental state of KS into two parts, on the one hand, the determination of the $self-consistent$ charge density (or potential) and, on the other hand, the diagonalization of the Hamiltonian KS for a fixed potential.

Traditionally, SC methods are used in spite of being mathematically less effective than direct methods (self-consistent minimization of functional KS is replaced by independent improvement of eigenfunctions and charge density). The reasons are simpler implementation and the inclusion of the mixed charge density, allowing to retain information of previous steps, avoiding the occurrence of charge oscillation problems. On the other hand, the advantages of the SC methods over the direct diagonalization of the Hamiltonian are clear:

▪ The use of only N_b test wave functions $(N_b \leq N_{plw})$ representing all occupied eigenstates and some gaps.

▪ The rapid evaluation of the action of $\widehat{H}$ on the electronic wave functions, through the transformation of the wave functions of the reciprocal space to the real one and vice versa through FFT.

▪ The inclusion of iterative methods within the self-consistent calculation, with which the optimization of charge density and wave functions can be performed almost simultaneously.

A common feature of all iterative methods is that they start from a set of basis functions, to which correction vectors are added in each iteration. This allows obtaining an approximate improvement to the eigenvalues and eigenvectors, through the Rayleigh-Ritz scheme [37,38] in which $\widehat{H}$ is diagonalized in the subspace of the expansion set and a problem of eigenvalues is solved.The result is the m eigenvectors associated with the m lowest eigenvalues in energy. The main difference lies in whether the optimization is done simultaneously, adding in each step N new vectors (blocked methods) or sequentially band by band so that in each iteration a single correction value (non-blocked methods) is added. These last ones are the ones included generally in the calculation codes since in spite of being considered slower than the blocked algorithms they do not need to store $2N_b$ vectors in each

iteration. On the other hand, they also allow a greater number of iterations so they are more efficient. An important amount within the iterative methods is the Rayleigh quotient or expected value of the Hamiltonian for a specific band:

$$\epsilon_{app} = \frac{\langle \varphi_m | \mathrm{H} | \varphi_m \rangle}{\langle \varphi_m | \mathrm{S} | \varphi_m \rangle} \tag{2.72}$$

Its variation with respect to $\langle \varphi_m |$ leads to a residual vector:

$$|\mathrm{R}(\varphi_m)\rangle = (H - \epsilon_{app})\,|\varphi_m\rangle sin\langle \varphi_m | \mathrm{S} | \varphi_m \rangle = 1 \tag{2.73}$$

The residual vector rule $\langle R|R\rangle$ measures the error in the eigenvector. Formally, a good approximation to the difference between the approximate eigenvector and the exact one is given by the expression:

$$|\delta\varphi_n\rangle = \frac{1}{H - \epsilon_{app}}\,|R\rangle. \tag{2.74}$$

However, the difficulty of evaluating the term $(H - \epsilon_{app})^{-1}$, requires an approximate treatment. Thus, the step that calculates the approximate error of the residual vector is called preconditioned and the matrix K that multiplies the residual vector in order to obtain $|\delta\varphi_n\rangle$ is called a preconditioned matrix $|\delta\varphi_n\rangle = K|R\rangle$. A preconditioned matrix usually used with slight modifications is the one proposed by Teter et al [39].

In sequential methods it is convenient to restrict the search vector to the orthonormal subspace to the wave functions under study. Thus, to ensure that the orthogonality between the bands is maintained, Lagrange multipliers are introduced, so that the gradient vector takes the form:

$$g(\varphi_m) = |g_m\rangle = (1 - \textstyle\sum_n |S|\varphi_n\rangle\langle\varphi_n|) \times H|\varphi_n\rangle \tag{2.75}$$

and the preconditioned search vector is given by:

$$|p(\varphi_m)\rangle = |p_m\rangle = (1 - \textstyle\sum_n |\varphi_n\rangle\langle\varphi_n|S) \times K(H - \epsilon_{app})|\varphi_m\rangle \tag{2.76}$$

The different sequential methods differ in the way that this correction vector is analogous to the wave functions. The iterative methods used in our calculations are the Davidson method [40], the conjugate gradient method (CG) [41] and the residual minimization method with direct inversion in the iterative subspace ($RMM\text{-}DIS$) [42]. In the

Davidson method, we start with a test vector $|\varphi_m^0\rangle$to which the preconditioned gradient $|p_m^0\rangle$ is added. The optimal eigenvector in each iteration is calculated, then, through the Rayleigh-Ritz scheme. After a band has been optimized several times it is passed to the next one. Finally, when all bands have been optimized, the optimal wave functions in the subspace of the N_b test functions (rotation in the subspace) are determined.

In the conjugate gradient method, the new direction $|f^M\rangle$for the iteration M is conjugated (independent) to the previous directions and is given by:

$$|f^M\rangle = |p_m^M\rangle + \frac{\langle p_m^M|g_m^M\rangle}{\langle p_m^{M-1}|g_m^{M-1}\rangle}|f^{M-1}\rangle \tag{2.77}$$

The optimal wave function $|\varphi_m^{M+1}\rangle$ is determined from the set $\{|\varphi_m^M\rangle/|f^M\rangle\}$through the Rayleigh-Ritz scheme. The only drawback associated with this method is the need for an explicit ortonomalization of the preconditioned residual vector to the set of test wave functions. This is a disadvantage in large systems since a single vector has to be orthonormal to a large number of vectors in each iteration. The solution proposed by Wood and Zunger is to minimize the residual vector rule instead of the Rayleigh-Ritz quotient.

Thus, orthonormalization is not necessary when presenting the minimum residual vector rule in the eigenvectors. This is the origin of the residual minimization method with direct investment in the iterative subspace ($RMM\text{-}DIS$). This method is based on the evaluation of the preconditioned residual vector for a band $K|R_m^0\rangle$. A fraction of steb is analogous to the starting wave function $|\varphi_m^0\rangle$originating the new wave function $|\varphi_m^1\rangle = |\varphi_m^0\rangle + \lambda K|R_m^0\rangle$,, and the new residual vector $|R_m^1\rangle$ is evaluated. A combination of the initial wave function $|\varphi_m^0\rangle$ is then generated and the test $|\varphi_m^1\rangle$, $|\varphi_m^M\rangle = \sum_{i=1}^{M} \alpha_i |\varphi_m^i\rangle$ ($M = 1$), in which the parameters α_i are those that minimize the residual vector rule. This minimization is known as the direct investment in the iterative subspace ($DIIS$). The next step starts from $|\bar{\varphi}^M\rangle$at the direction$K|\bar{R}^M\rangle$.In each iteration M, a new wave function $|\varphi_m^M\rangle = |\bar{\varphi}^{M-1}\rangle + \lambda K|\bar{R}^{M-1}\rangle$ and a new residual vector $|(R\varphi_m^M)\rangle$is addedto the iterative subspace. The main drawback of this method is that it always finds the vector closest to the initial test vector, so it can lead to false fundamental states (absence of eigenvectors in the final solution). To avoid this, initialization has to be done carefully, starting with a set of random test vectors and sweeping over all the bands. These sweeps involve a rotation in the subspace in addition to the steps in the direction of residual vectors preconditioned by bands. Finally, after the sweeps

on all the bands, the final vectors reorthonormalize. Although, in principle, the *RMM-DIS* method should converge without explicit rotation in the subspace or explicit orthonormalization, these operations allow to improve the convergence and ensure the obtaining of the ground state (especially if the spacing between eigenvalues is small).

The wave functions optimized in the different iterative methods allow to calculate a new charge density. This leads to the next part of the problem where self-consistency with respect to the input charge density must be achieved, i.e. the residual charge density vector $R[\rho_{in}] = \rho_{out} - \rho_{in}$has to be canceled. It is also possible to consider the self-consistency for the potential, since the convergence of the potential and the charge density are equivalent. The direct iteration $\rho_{in}^{n+1} = \rho_{out}^{n}$ leads to problems of charge oscillations, with which the algorithm diverges. To avoid these oscillations and facilitate convergence, different methods have been designed. The simplest is the linear mixing in which a linear combination of the input and output density generate the starting density of the following iteration:

$$\rho_{in}^{m+1} = (1-\alpha)\rho_{in}^{m} + \alpha\rho_{out}^{m} \tag{2.78}$$

An extension of this method is the Anderson method [43], in which information from a greater number of previous iterations is included. It presents, however, the problem of the appearance of linear dependencies. Other more efficient mixtures are those attributed to Pulay [44] and Broyden [45]. In the first, the optimal input charge density is obtained as a linear combination of the input density of all the previous steps $\rho_{in}^{opt} = \sum_i \alpha_i \rho_{in}^{i}$. The optimal α_i are obtained by minimizing the residual vector rule $\langle \mathrm{R}[\rho_{in}^{opt}] | R[\rho_{in}^{opt}] \rangle$ under the requirement $\sum_i \alpha_i = 1$ and assuming the linearity of the residual vector with respect to to the input density $\mathrm{R}[\rho_{in}^{opt}] = \sum_i \alpha_i \mathrm{R}[\rho_{in}^{i}]$. The quasi-Newton algorithms proposed by Broyden assume that the residual vector can be linearized close to the minimum:

$$R[\rho] = \mathrm{R}[\rho_{in}^{m}] - J^{m}(\rho - \rho_{in}^{m}) \tag{2.79}$$

Where J^m is an approximation to the Jacobian matrix. Imposing that $R[\rho^*] = 0$ we obtain the optimal charge density that makes the vector zero:

$$\rho^* = \rho_{in}^{m} + (J^{m})^{-1}\mathrm{R}[\rho_{in}^{m}] \tag{2.80}$$

In each iteration an approximation is constructed for the Jacobean matrix from which a new charge density is obtained. The algorithms differ in the way in which J^m is

generated in each iteration. For some of its parameters this method is reduced to the Pulay method.

2.5.2.3. Geometric optimization

The objective of the geometrical optimization is to find the optimal structure (cell constants and internal parameters) of the crystal from an arbitrary state. For this, it is necessary to calculate the forces acting on the atoms. Through the Hellmann-Feynman theorem [46], the force F_I on an atom I in the position $\vec{R}_I$ is given by $F_I = -\frac{\partial E}{\partial R_I}$, where E is the energy and R_I the position atomic. Once the forces on the atoms have been calculated, the atomic equilibrium structure of the system is achieved considering the total energy as a function of the atomic coordinates.

Within the planewave-pseudopotential approximation the forces are very simple to calculate and inexpensive computationally. In fact, the application of the Hellmann-Feynman theorem is strictly valid in the case of a plane wave base, since they are floating (they do not belong to a determining atom) and represent all regions of space with the same precision. Thanks to this, the Pulay forces coming from the derivation of the basis functions with respect to the nuclear coordinates cancel out. Within the algorithms used in the geometrical optimization, we highlight conjugated gradient methods [41] and quasi-Newton methods ($RMM\text{-}DIS$[44], $BFGS$ [47]). These methods are fast and efficient if the starting point is close to a local minimum, but they fail if this is not the case.

2.5.3. PAW method

The main problem represented by the ultrasoft pseudopotentials is their difficulty in construction, since by including many parameters (several cutting radii), many tests have to be carried out to prove their accuracy and transferability. This problem is solved partially through the method PAW (Blöchl) [48,49], which combines the versatility of the method of linear increased plane waves ($LPAW$) with the approximation of PP. The fundamental idea is that the true wave function (ψ) and a well-behaved pseudo-wave function (ψ) are related by a linear transformation ($\psi = T\psi$). This allows to easily calculate all the physical properties in the pseudo-space of the pseudo-wave function (computationally more manageable than the all-electron wave function). Thus, the original Hamiltonian $H_{KS}$is transformed, virtue to the linear transformation that relates the real wave function and the pseudo-wavefuncion, into a

pseudo-Hamiltonian $\widetilde{\mathrm{H}}_{KS}$ easier to solve: $T^{+}H_{KS}T = \widetilde{\mathrm{H}}_{KS}$ .The strategy (typical of the augmented wave method) consists in dividing the crystal into an augmentation region, formed by spheres in which the atoms and an interstitial region (the rest of the crystal) are located. The radius of the spheres must be small enough so that the spheres do not overlap, but at the same time large enough for the electron density of the core to remain within the spheres.

Frequently, it is chosen equal to the value of half the distance between first neighbors. According to this division, the total wave function expands in plane waves in the interstitial region and in atomic wave functions centered on the atoms in the augmentation region. On the one hand, the plane wave part provides flexibility to the description of the tail region of the wave functions, but, by requiring a prohibitive number of basis functions to correctly describe the oscillations of the wave functions near the nucleus opts for expansions in atomic orbitals to correctly describe the nodal structure of the wave functions near the nucleus.

The transformation operator T is given by the sum of the identity operator and the sum of atomic contributions $T = 1 + \sum_R S_R$(R = atomic positions), which shows that modifies the pseudo-wavefuncion within the atomic region in order to generate the correct nodal structure.

Thus, the construction of a potential PAW requires, first of all, an all-electron calculation for the reference atom. Generally, for each angular quantum number lm two reference energies are chosen, whose solutions are the partial waves $|\varphi_i(r)\rangle$. The next step is the introduction of pseudoatomical wave functions and projector functions in order to have a practical approach that ensures that the complete wave function is continuous and differentiable across the interstitial augment-area surface, and to cancel the part of plane waves of the full wave function within the spheres of increase. Pseudoatomical wave functions are functions of the KS equations for an isolated pseudoatom, identical to the atomic wave functions outside the augmented sphere and with eigenvalues equal to those.

Within the spheres of magnification, the wave function and the pseudofunction wave take the form:

$$\psi(\vec{r}) = \sum_i \Phi_i(\vec{r}) c_i \; \tilde{\psi}(\vec{r}) = \sum_i \tilde{\Phi}_i(\vec{r}) c_i \tag{2.81}$$

From these 2 equations it follows that

$$|\psi\rangle = |\tilde{\psi}\rangle - \sum_i \widetilde{\Phi}_i(\vec{r})c_i + \sum_i \Phi_i(\vec{r})c_i \quad (2.82)$$

As the linear T tranformation, the coefficients c_i must be linear functions of the pseudo-wave functions. They are given by the integral overlap between the pseudo-wavefuncion and projector functions $\langle\tilde{p}_i|\widetilde{\psi}\rangle$. Projector functions are mathematical constructs that connect the augmentation and interstitial regions. Within the increase region, the condition is met:

$$\sum_i |\widetilde{\Phi}_i\rangle\langle\tilde{p}_i| = 1 \quad (2.83)$$

which implies that $\langle\tilde{p}_i|\widetilde{\Phi}_j\rangle = \delta_{ij}$, that is, they are dual to atomic pseudofunctions.

The combination of the above equations allows to determine the general form of the transformation operator T:

$$T = 1 + \sum_i (|\Phi_i\rangle - |\widetilde{\Phi}_i\rangle)\langle\tilde{p}_i| \quad (2.84)$$

with which the all-electron wave function is obtained from the corresponding pseudo-wavefunction through the relationship:

$$|\psi\rangle = |\tilde{\psi}\rangle + \sum_i (|\Phi_i\rangle - |\widetilde{\Phi}_i\rangle)\langle\tilde{p}_i|\tilde{\psi}\rangle. \quad (2.85)$$

Like the wave function $|\psi\rangle$, most observables, including total energy, can be divided into three conditions: one from the plane wave part and a pair of expansions in atomic orbitals in each atom. On the other hand, the contributions coming from the atomic orbitals are divided in turn into contributions of each atom, so that there are no overlapping terms between atomic orbital in different positions.

The final expression for energy takes the form:

$$E(\vec{r}) = \tilde{E}(\vec{r}) + E^1(\vec{r}) - \tilde{E}^1(\vec{r}) \quad (2.86)$$

The term $\tilde{E}$ is calculated in a regular grid, while E^1 and $\tilde{E}^1$ are calculated in radial grids centered on the atoms. The decomposition in a regular grid is complete, so it is not necessary to calculate the crossing terms between the grids. During the linearization of the last two terms, it is possible to derive the US pseudopotential from the PAW potentials. The main difference between PAW and US - PP comes from the increase charges. In the US - PP approach, the 'distorted' magnification charges are represented in a regular grid. In order to

accurately represent the load distribution of the all-electron wave function, the cut-off radius is close to the maximum of the all-electron wave function, which leads to contracted and localized magnification loads, with the consequent associated computational cost. The PAW method avoids this problem, through the introduction of radial grids, in which the increase loads are quite extended (they are softer).

In general, PAW potentials are more suitable than ultrasoft pseudopotentials. There are two reasons for this. First, the r_c are smaller than r_c used in the ultrasoft pseudopotentials and second, they reconstruct the exact valence wave function with all the nodes in the core region. The only disadvantage is given by the fact that r_c is smaller, which makes the E_{cutoff} slightly larger.

2.6. CODES USED IN THE THESIS

2.6.1 ABINIT package

We use ABINIT program [50] for the total energy and electronic structure calculations. All calculations were performed using the GGA exchange-correlation functional of Perdew-Burke-Ernzerhof [51] and the so-called *FHI* atomic plane wave pseudo potentials [52] are adopted. The geometrical optimization was performed at pressure via Broyden-Fletcher-Goldfarb-Shanno minimization technique [53]. To ensure the stability of the structure during successive deformations, the lattice parameters and the atomic positions for each deformation are taken from the output of the previous deformation. We print the cif.file for visualizing the bond length. The script-job allows an automatic run using the input-initial as a template. At the end we get the results (stress-strain) using the script-extract.

2.6.1.1 Script-job for strain (2H-MoS_2)

```
  #! /bin/csh
#########################################################################
foreach ee(0.00 0.05 0.10 0.15 0.20 0.25 0.30 0.35 0.40)
#foreach ee(0.15 0.16 0.17 0.18 0.20 0.21 0.22 0.23)
gawk 'BEGIN
{key=not;nn1=1000;nn=1000;mm=1000;p1="1.0";p2="0.0";p3="0.0";p4="0.0";p5="1.0";p6=
"0.0";p7="0.0";p8="0.0";p9="1.0"} \\
   /-outvars: echo values of variables after computation  --------/  {nn1=NR}\\
  /acell/ {AA=$2;BB=$3;CC=$4} \\
   / rprim/ {if(NR>nn1) {p1=$2;p2=$3;p3=$4;nn=NR;key="yes"}} \\
   {if (NR==nn+1 && key=="yes"){p4=$1;p5=$2;p6=$3}  \\
   if (NR==nn+2 && key=="yes"){p7=$1;p8=$2;p9=$3}}  \\
     /xred/  {mm=NR} \\
   /xred/ {x1=$2;x2=$3;x3=$4;mm=NR} \\
```

```
    {if (NR==mm+1) {x4=$1;x5=$2;x6=$3} \\
      if (NR==mm+2) {x7=$1;x8=$2;x9=$3} \\
      if (NR==mm+3) {x10=$1;x11=$2;x12=$3} \\
      if (NR==mm+4) {x13=$1;x14=$2;x15=$3} \\
      if (NR==mm+5) {x16=$1;x17=$2;x18=$3} \\
      if (NR==mm+6) {x19=$1;x20=$2;x21=$3} \\
      if (NR==mm+7) {x22=$1;x23=$2;x24=$3} \\
      if (NR==mm+8) {x25=$1;x26=$2;x27=$3} \\
      if (NR==mm+9) {x28=$1;x29=$2;x30=$3} \\
      if (NR==mm+10) {x31=$1;x32=$2;x33=$3} \\
      if (NR==mm+11) {x34=$1;x35=$2;x36=$3}} \\
    END {e=('$ee'+0.05); rprim11=(1+('$ee'+0.05)); bb=(BB*p5); cc=(CC*p9); printf "%s %s
%s %s %s %s %s %s %s %s %s %s %s %s %s %s %s %s %s %s %s %s %s %s %s %s %s
%s %s %s %s %s %s %s %s %s %s %s %s %s %s %s %s %s %s %s %s %s %3.2f %15.8f
%15.8f %15.8f\n",
AA,BB,CC,p1,p2,p3,p4,p5,p6,p7,p8,p9,x1,x2,x3,x4,x5,x6,x7,x8,x9,x10,x11,x12,x13,x14,x15
,x16,x17,x18,x19,x20,x21,x22,x23,x24,x25,x26,x27,x28,x29,x30,x31,x32,x33,x34,x35,x36,e,
rprim11,bb,cc}' filename.out_$ee > parametrosPAR
###########################################################################
set par=(`cat parametrosPAR`)
############################################################################set
#set aa = `echo "$par[1]`
#set bb = `echo "$par[2]`
#set cc = `echo "$par[3]`
#set mat11 = `echo "$par[4]`
#set mat12 = `echo "$par[5]`
#set mat13 = `echo "$par[6]`
#set mat21 = `echo "$par[7]`
#set mat22 = `echo "$par[8]`
#set mat23 = `echo "$par[9]`
#set mat31 = `echo "$par[10]`
#set mat32 = `echo "$par[11]`
#set mat33 = `echo "$par[12]`
#set x1 = `echo $par[13]`
#set y1 = `echo $par[14]`
#set z1 = `echo $par[15]`
#set x2 = `echo $par[16]`
#set y2 = `echo $par[17]`
#set z2 = `echo "$par[18]`
#set x3 = `echo $par[19]`
#set y3 = `echo $par[20]`
#set z3 = `echo $par[21]`
#set x4 = `echo $par[22]`
#set y4 = `echo $par[23]`
#set z4 = `echo "$par[24]`
#set x5 = `echo $par[25]`
#set y5 = `echo $par[26]`
#set z5 = `echo $par[27]`
#set x6 = `echo $par[28]`
#set y6 = `echo $par[29]`
```

```
#set z6 = `echo "$par[30]`
#set x7 = `echo $par[31]`
#set y7 = `echo $par[32]`
#set z7 = `echo $par[33]`
#set x8 = `echo $par[34]`
#set y8 = `echo $par[35]`
#set z8 = `echo "$par[36]`
#set x9 = `echo $par[37]`
#set y9 = `echo $par[38]`
#set z9 = `echo $par[39]`
#set x10 = `echo $par[40]`
#set y10 = `echo $par[41]`
#set z10 = `echo "$par[42]`
#set x11 = `echo $par[43]`
#set y11 = `echo $par[44]`
#set z11 = `echo $par[45]`
#set x12 = `echo $par[46]`
#set y12 = `echo $par[47]`
#set z12 = `echo "$par[48]`
#set eenext = `echo "$par[49]` #Tensile strain e (contador para los nombre de los ficheros)
#set rprim11-next =  `echo "$par[50]` #  Tensile extrain e+1 en que se mete en abinit
#set bb-abinit =  `echo "$par[51]` # parametro b si rprim cambia b=bcell*(rprim-imput/rprim-out)
#set cc-abinit =  `echo "$par[52]` # parametro c si rprim cambia c=ccell*(rprim-imput/rprim-out)
##########################################################################
sed -e "s/ee/$par[49]/g"   filename.files_initial  > filename.files_$par[49]
##########################################################################
sed -e "s/bred/$par[51]/g" -e "s/cred/$par[52]/g" -e "s/MAT11/$par[50]/g" -e
"s/X1/$par[13]/g" -e "s/Y1/$par[14]/g"  -e "s/Z1/$par[15]/g"  -e "s/X2/$par[16]/g"  -e
"s/Y2/$par[17]/g"   -e "s/Z2/$par[18]/g"   -e "s/X3/$par[19]/g"   -e "s/Y3/$par[20]/g"   -e
"s/Z3/$par[21]/g" -e "s/X4/$par[22]/g"   -e "s/Y4/$par[23]/g"   -e "s/Z4/$par[24]/g" -e
"s/X5/$par[25]/g"   -e "s/Y5/$par[26]/g"  -e "s/Z5/$par[27]/g"  -e "s/X6/$par[28]/g"  -e
"s/Y6/$par[29]/g"   -e "s/Z6/$par[30]/g"   -e "s/X7/$par[31]/g"   -e "s/Y7/$par[32]/g"   -e
"s/Z7/$par[33]/g" -e "s/X8/$par[34]/g"   -e "s/Y8/$par[35]/g"   -e "s/Z8/$par[36]/g" -e
"s/X9/$par[37]/g"   -e "s/Y9/$par[38]/g"  -e "s/Z9/$par[39]/g"  -e "s/x10/$par[40]/g"  -e
"s/y10/$par[41]/g"   -e "s/z10/$par[42]/g"   -e "s/x11/$par[43]/g"   -e "s/y11/$par[44]/g"   -e
"s/z11/$par[45]/g" -e "s/x12/$par[46]/g"   -e "s/y12/$par[47]/g"   -e "s/z12/$par[48]/g"
vgrid_b4-rprim.in_initial  > vgrid_b4-rprim.in_00.0_$par[49]
##########################################################################
mpirun -np 8 abinit <  filename.files_$par[49]  >& log
#el end del foreach
end
```

2.6.1.2 Script-job for transversal stress (2H-MoS_2)

```
#! /bin/csh
##########################################################################
foreach pgpa(00 10 20 30 40)
gawk 'BEGIN
{key=not;nn1=1000;nn=1000;mm=1000;p1="1.0";p2="0.0";p3="0.0";p4="0.0";p5="1.0";p6=
"0.0";p7="0.0";p8="0.0";p9="1.0"} \\
```

```
    /-outvars: echo values of variables after computation  --------/  {nn1=NR}\\
   /acell/ {AA=$2;BB=$3;CC=$4} \\
    / rprim/ {if(NR>nn1) {p1=$2;p2=$3;p3=$4;nn=NR;key="yes"}} \\
    {if (NR==nn+1 && key=="yes"){p4=$1;p5=$2;p6=$3}  \\
    if (NR==nn+2 && key=="yes"){p7=$1;p8=$2;p9=$3}}  \\
       /xred/  {mm=NR} \\
    /xred/ {x1=$2;x2=$3;x3=$4;mm=NR} \\
   {if (NR==mm+1) {x4=$1;x5=$2;x6=$3} \\
     if (NR==mm+2) {x7=$1;x8=$2;x9=$3} \\
     if (NR==mm+3) {x10=$1;x11=$2;x12=$3} \\
     if (NR==mm+4) {x13=$1;x14=$2;x15=$3} \\
     if (NR==mm+5) {x16=$1;x17=$2;x18=$3} \\
     if (NR==mm+6) {x19=$1;x20=$2;x21=$3} \\
     if (NR==mm+7) {x22=$1;x23=$2;x24=$3} \\
     if (NR==mm+8) {x25=$1;x26=$2;x27=$3} \\
     if (NR==mm+9) {x28=$1;x29=$2;x30=$3} \\
     if (NR==mm+10) {x31=$1;x32=$2;x33=$3} \\
     if (NR==mm+11) {x34=$1;x35=$2;x36=$3}} \\
   END {pp=('$pgpa'+10);p=(pp/29421.033); aa=(AA*p1); bb=(BB*p5); cc=(CC*p9); printf
"%s %s %s %s %s %s %s %s %s %s %s %s %s %s %s %s %s %s %s %s %s %s %s %s %s %s %s
%s %s %s %s %s %s %s %s %s %s %s %s %s %s %s %s %s %s %s %s %s %s %s %s %3.2f
%15.8f  %15.8f %15.8f %15.8f\n",
AA,BB,CC,p1,p2,p3,p4,p5,p6,p7,p8,p9,x1,x2,x3,x4,x5,x6,x7,x8,x9,x10,x11,x12,x13,x14,x15
,x16,x17,x18,x19,x20,x21,x22,x23,x24,x25,x26,x27,x28,x29,x30,x31,x32,x33,x34,x35,x36,e,
p,aa,bb,cc}' filename.out_$pgpa > parametrosPAR
#############################################################################
set par=(`cat parametrosPAR`)
#############################################################################set
#set aa = `echo "$par[1]`
#set bb = `echo "$par[2]`
#set cc = `echo "$par[3]`
#set mat11 = `echo "$par[4]`
#set mat12 = `echo "$par[5]`
#set mat13 = `echo "$par[6]`
#set mat21 = `echo "$par[7]`
#set mat22 = `echo "$par[8]`
#set mat23 = `echo "$par[9]`
#set mat31 = `echo "$par[10]`
#set mat32 = `echo "$par[11]`
#set mat33 = `echo "$par[12]`
#set x1 = `echo $par[13]`
#set y1 = `echo $par[14]`
#set z1 = `echo $par[15]`
#set x2 = `echo $par[16]`
#set y2 = `echo $par[17]`
#set z2 = `echo "$par[18]`
#set x3 = `echo $par[19]`
#set y3 = `echo $par[20]`
#set z3 = `echo $par[21]`
#set x4 = `echo $par[22]`
```

```
#set y4 = `echo $par[23]`
#set z4 = `echo "$par[24]`
#set x5 = `echo $par[25]`
#set y5 = `echo $par[26]`
#set z5 = `echo $par[27]`
#set x6 = `echo $par[28]`
#set y6 = `echo $par[29]`
#set z6 = `echo "$par[30]`
#set x7 = `echo $par[31]`
#set y7 = `echo $par[32]`
#set z7 = `echo $par[33]`
#set x8 = `echo $par[34]`
#set y8 = `echo $par[35]`
#set z8 = `echo "$par[36]`
#set x9 = `echo $par[37]`
#set y9 = `echo $par[38]`
#set z9 = `echo $par[39]`
#set x10 = `echo $par[40]`
#set y10 = `echo $par[41]`
#set z10 = `echo "$par[42]`
#set x11 = `echo $par[43]`
#set y11 = `echo $par[44]`
#set z11 = `echo $par[45]`
#set x12 = `echo $par[46]`
#set y12 = `echo $par[47]`
#set z12 = `echo "$par[48]`
#set pnext = `echo "$par[49]` #Tensile strain e (contador para los nombre de los ficheros)
#set p-abinit =  `echo "$par[50]`
#set aa-abinit =  `echo "$par[51]` #  parametro a si rprim cambia a=acell*(rprim-imput/rprim-out)
#set bb-abinit =  `echo "$par[52]` # parametro b si rprim cambia b=bcell*(rprim-imput/rprim-out)
#set cc-abinit =  `echo "$par[53]` # parametro c si rprim cambia c=ccell*(rprim-imput/rprim-out)
##########################################################################
sed -e "s/ee/$par[49]/g"   filename.files_initial  > filename.files_$par[49]
##########################################################################
sed -e "s/ared/$par[51]/g" -e "s/bred/$par[52]/g" -e "s/cred/$par[53]/g" -e
"s/PGPa/$par[50]/g" -e "s/X1/$par[13]/g" -e "s/Y1/$par[14]/g"  -e "s/Z1/$par[15]/g"  -e
"s/X2/$par[16]/g"  -e "s/Y2/$par[17]/g"   -e "s/Z2/$par[18]/g"   -e "s/X3/$par[19]/g"   -e
"s/Y3/$par[20]/g"   -e "s/Z3/$par[21]/g" -e "s/X4/$par[22]/g"   -e "s/Y4/$par[23]/g"   -e
"s/Z4/$par[24]/g" -e "s/X5/$par[25]/g"   -e "s/Y5/$par[26]/g"  -e "s/Z5/$par[27]/g"  -e
"s/X6/$par[28]/g"  -e "s/Y6/$par[29]/g"   -e "s/Z6/$par[30]/g"   -e "s/X7/$par[31]/g"   -e
"s/Y7/$par[32]/g"   -e "s/Z7/$par[33]/g" -e "s/X8/$par[34]/g"   -e "s/Y8/$par[35]/g"   -e
"s/Z8/$par[36]/g" -e "s/X9/$par[37]/g"   -e "s/Y9/$par[38]/g"  -e "s/Z9/$par[39]/g"  -e
"s/x10/$par[40]/g"  -e "s/y10/$par[41]/g"   -e "s/z10/$par[42]/g"   -e "s/x11/$par[43]/g"   -e
"s/y11/$par[44]/g"   -e "s/z11/$par[45]/g" -e "s/x12/$par[46]/g"   -e "s/y12/$par[47]/g"   -e
"s/z12/$par[48]/g"  vgrid_b4-rprim.in_initial  > vgrid_b4-rprim.in_00.0_$par[49]
##########################################################################
mpirun -np 8 abinit <  filename.files_$par[49]  >& log
```

```
#el end del foreach
End
```

2.6.1.3 Input-initial for strain (2H-MoS_2)

```
#calculations of the atomic volumes (critic)
# Unit cell
acell    ared  bred 9.8280170035E+00
rprim        1.0  0.0  0.0
             0.0 1.0  0.0
             0.0  0.0  MAT33
# En P1
nsym 1
#symrel      1  0  0   0  1  0   0  0  1
#tnons      0.0000000  0.0000000  0.0000000
# Definition of the atoms
ntypat 2
znucl  42 8
natom 12
typat  1 1 1 1 2 2 2 2 2 2 2 2
xred
  X1  Y1 Z1
  X2  Y2 Z2
  X3  Y3 Z3
  X4  Y4 Z4
  X5  Y5 Z5
  X6  Y6 Z6
  X7  Y7 Z7
  X8  Y8 Z8
  X9  Y9 Z9
  x10  y10 z10
  x11  y11 z11
  x12  y12 z12
# exchange-correlation functional
ixc 11
#Definition of the self-consistency procedure
diemac   9.0 # Model dielectric preconditioner
nstep   200  # Maxiumum number of SCF iterations
tolvrs 1d-18
# ecut -> optimized, change it!
ecut   40
#Don't generate _DEN,_EIG,_WFK
prtden 0
prteig 0
prtwf 0
# kpts -> optimized, change it!
kptopt  1
ngkpt   11 10 6
nshiftk   1            # Use one copy of grid only (default)
shiftk   0.5 0.5 0.5    # This choice of origin for the k point grid
```

```
                # preserves the hexagonal symmetry of the grid,
                # which would be broken by the default choice.
# ficheros cif
prtcif 1
# symbreak
chksymbreak 0
# optimization
ntime  50
tolmxf  5.0d-5
ionmov  2
optcell 9
# fix the pressure to transition pressure Pt=0.00, 20, 40 GPa dividirlo entre 29421.033
#fix pressure##########################################
strtarget   0.00  0.00  0.00  0.00  0.00  0.00
#########################################################################
ecutsm 0.5
strprecon 0.5
dilatmx 1.5
```

2.6.1.4 Input-initial for transversal stress (2H-MoS_2)

```
#calculations of the atomic volumes (critic)
# Unit cell
acell    ared  bred cred
rprim        1.0  0.0  0.0
             0.0 1.0  0.0
             0.0  0.0  1.0
# En P1
nsym 1
#symrel      1  0  0   0  1  0   0  0  1
#tnons      0.0000000  0.0000000  0.0000000
# Definition of the atoms
ntypat 2
znucl  42 8
natom 12
typat  1 1 1 1 2 2 2 2 2 2 2 2
xred
  X1  Y1 Z1
  X2  Y2 Z2
  X3  Y3 Z3
  X4  Y4 Z4
  X5  Y5 Z5
  X6  Y6 Z6
  X7  Y7 Z7
  X8  Y8 Z8
X9  Y9 Z9
 x10  y10 z10
 x11  y11 z11
 x12  y12 z12
```

```
# exchange-correlation functional
ixc 11
#Definition of the self-consistency procedure
diemac   9.0 # Model dielectric preconditioner
nstep   200  # Maxiumum number of SCF iterations
tolvrs 1d-18
# ecut -> optimized, change it!
ecut   40
#Don't generate _DEN,_EIG,_WFK
prtden 0
prteig 0
prtwf 0
# kpts -> optimized, change it!
kptopt  1
ngkpt   11 10 6
nshiftk   1            # Use one copy of grid only (default)
shiftk   0.5 0.5 0.5    # This choice of origin for the k point grid
                  # preserves the hexagonal symmetry of the grid,
                  # which would be broken by the default choice.
# ficheros cif
prtcif 1
# symbreak
chksymbreak 0
# optimization
ntime  50
tolmxf  5.0d-5
ionmov  2
optcell 2
# fix the pressure to transition pressure Pt=0.00, 20, 40 GPa dividirlo entre 29421.033
#fix pressure##########################################
strtarget   PGPa  PGPa 0.00  0.00  0.00  0.00
#########################################################################
ecutsm 0.5
strprecon 0.5
dilatmx 1.5
```

2.6.1.5 Script extract (2H-SiC)

```
#! /bin/csh
foreach AA(0.00 0.05 0.10 0.15 0.20 0.25 0.30 0.35 0.40)
gawk 'BEGIN {nn=1000;mm=1000;rr=1000} \\
    /(ucvol)/ {volume=$6} \\
    /Pressure=/ {pressure=$8} \\
   /Pressure=/ {rr=NR} \\
  {if (NR==rr+1) {sigma11=$4;sigma32=$7} \\
   if (NR==rr+2) {sigma22=$4;sigma31=$7} \\
   if (NR==rr+3) {sigma33=$4;sigma21=$7}} \\
     /-outvars: echo values of variables after computation  --------/  {nn=NR} \\
```

```
 /acell/ {a=$2;b=$3;c=$4}\\
/etotal/ {etotal=$2} \\
/xred/ {mm=NR} \\
/xred/ {x1=$2;x2=$3;x3=$4;mm=NR} \\
{if (NR==mm+1) {x4=$1;x5=$2;x6=$3}\\
  if (NR==mm+2) {x7=$1;x8=$2;x9=$3} \\
  if (NR==mm+3) {x10=$1;x11=$2;x12=$3} \\
  if (NR==mm+4) {x13=$1;x14=$2;x15=$3} \\
  if (NR==mm+5) {x16=$1;x17=$2;x18=$3} \\
  if (NR==mm+6) {x19=$1;x20=$2;x21=$3} \\
  if (NR==mm+7) {x22=$1;x23=$2;x24=$3}} \\
END {printf " %4.3f %s %s %s %s %s %s %s %s %s %s %s %s %s %s %s %s %s %s
%s %s %s %s %s %s %s %s %s %s %s %s %s %s %s %s %s\n",
'$AA',volume,pressure,sigma11,sigma22,sigma33,sigma32,sigma31,sigma21,a,b,c,etotal,x1,x
2,x3,x4,x5,x6,x7,x8,x9,x10,x11,x12,x13,x14,x15,x16,x17,x18,x19,x20,x21,x22,x23,x24}'
filename.out_00.0_$AA >> salida
end
awk '{printf " %4.3f %s %s %s %s %s %s\n",$1,$2,$4,$10,$11,$12,$13}' salida >>
salidatotal
```

2.6.1.6 .file-initial for transversal stress (2H-MoS$_2$)

```
filename.in_ee
filename.out_ee
filename_i_ee
filename_o_ee
filename_tmp_ee
42-Mo.GGA.fhi
08-O.GGA.fhi
```

2.6.1.7 .file-initial for strain (2H-MoS$_2$)

```
filename.in_pgpa
filename.out_pgpa
filename_i_pgpa
filename_o_ pgpa
filename_tmp_pgpa
42-Mo.GGA.fhi
08-O.GGA.fhi
```

2.6.1.8 .file-initial for strain-transversal stress (2H-MoS$_2$)

```
filename.in_pgpa_ee
filename.out_pgpa_ee
filename_i_pgpa_ee
filename_o_ pgpa_ee
filename_tmp_pgpa_ee
42-Mo.GGA.fhi
08-O.GGA.fhi
```

2.6.2 GIBBS program

The equation of state (EOS) is a thermodynamic equation describing properties of solids with respect to changes in the macroscopic variables (p,V,T). GIBBS [54] can analyses the output of electronic structure calculations using a set of energy-volume (E-V) data using a selected form of EOS. The equilibrium volume, bulk modulus (B_0) and its pressure derivative (B_0'), both evaluated at zero pressure, were obtained by fitting the 4th order static Birch-Murnaghan EOS [55] to the calculated (E-V) data set. We applied this method to the (E-V) data obtained from the electronic structure calculations of crystals under hydrostatic pressure.

The 4th order static Birch-Murnaghan EOS takes the form

$$E = E_0 + \frac{3}{8} V_0 B_0 f^2 \{(9H - 63B_0{}' + 143)f^2 + 12(B_0{}' - 4)f + 12\}$$

$$p = \frac{1}{2} B_0 (2f + 1)^{5/2} \{(9H - 63B_0{}' + 143)f^2 + 9(B_0{}' - 4)f + 6\}$$

$$B = \frac{1}{6} B_0 (2f + 1)^{5/2} \{(99H - 693B_0{}' + 1573)f^3 + (27H - 108B_0{}' + 105)f^2 + 6(3B_0{}' - 5)f + 6\}$$

Where $H = B_0 B_0{}'' + B_0{}'^2$ and f is the finite Eulerian strain in terms of a reference volume V_r in our case the zero pressure volume.

$$f = \frac{1}{2}\left[\left(\frac{V_r}{V}\right)^{2/3} - 1\right].$$

References

[1] M. Born and R. Oppenheimer. **Translated by S M Blinder with emendations by Brian Sutclie and Wolf Geppert.** R. Annu. Phys, **84**:475, 1927.

[2] V. Fock. **Supercomputer Simulations in Chemistry: Proceedings of the Symposium on ..** Z. Phys, **61**:126, 1930.

[3] A. Shukla, M. Dolg, P. Fulde and H. Stoll. **LCAO Treatment of Crystals and Nanostructures**. Phys. rev. B, **60:**5211, 1999.

[4] R. G. Parr and W. Yang. **Density Functional Theory of Atoms and Molecules**. Oxford University Press, New York, 1997.

[5**]** W. Kohn and L. J. Sham. **Self-Consistent Equations Including Exchange and Correlation Effects.** Phys. rev., 140:1133A, 1965.

[6**]** P. Hohenberg and W. Kohn. **Inhomogeneous Electron Gas.** Phys. rev., 136:864B, 1964.

[7] L. H. Tomas. **Theory of the Inhomogeneous Electron Gas**. Proc. Camb. Phil. Soc., 23:542, 1926.

[8] E. Fermi. **A Celebration Of The Contributions Of ...** Zeits fur Physik, 48:73, 1928.

[9] M. Levy. **Electron densities in search of Hamiltonians.** Phys. rev. A, 26:1200, 1982.

[10] D. M. Ceperley and B. J. Alder. **Ground State of the Electron Gas by a Stochastic Method.** Phys. rev. Lett., 45:566, 1980.

[11] J. P. Perdew and A. Zunger. **Self-interaction correction to density-functional approximations for many-electron systems.** Phys. rev. B, 23:5048, 1981.

[12] A. D. Becke. **Hartree–Fock exchange energy of an inhomogeneous electron gas.** Int. J. Quantum Chem., **23**:1915, 1983.

[13] J. P. Perdew and W. Yang. **Accurate and simple density functional for the electronic exchange energy: Generalized gradient approximation.** Phys. rev. B, 33:8800, 1986.

[14] A. D. Becke. **Density-functional exchange-energy approximation with correct asymptotic behavior.** Phys. rev. A, **38:**3098, 1988.

[15**]** E. Clementi and C. Roetti**. Roothaan-Hartree-Fock atomic wavefunctions: Basis functions and their coefficients for ground and certain excited states of neutral and ionized atoms, Z≤54.** At. Data Nucl. Data Tables, 14:177, 1974.

[16] J. P. Perdew and W. Yang. **Accurate and simple analytic representation of the electron-gas correlation energy.** Phys. rev. B, **45**:13244, 1992.

[17**]** C. Lee, W. Yang and R. G. Parr. **Development of the Colle-Salvetti correlation-energy formula into a functional of the electron density.** Phys. rev. B, 37:785, 1988.

[18] R. Colle and O. Salvetti. **Fragmentation dynamics of biomolecules in gas phase and water environment. A thesis submitted for the degree of Doctor.** Theor. Chim. Acta, **37**:4135, 1975.

[19] A. D. Becke. **Density-functional thermochemistry. III. The role of exact exchange.** J. chem. phys., **98**:1372, 1992.

[20] A. D. Becke. **Density-functional thermochemistry. III. The role of exact exchange** . J. chem. phys., **98**:5648, 1993.

[21] V. Luaña and L. Pueyo. **Simulation of ionic crystals: The initio perturbed- ion methods and application to alkali hydrides and halides.** Phys. rev. B, **41**:3800, 1990.

[22**]** M.A. Blanco, V. Luaña and A. M. Pendas. **Quantum mechanical cluster calculations of ionic materials: Revision 10 of the*ab initio* Perturbed Ion program.** Comput. Phys. Commun, 103:287, 1997.

[23] R. Mc Weeny and B. T. Sutcliffe. **Methods of Molecular quantum Mechanics.** Academic, London, 1969.

[24] N. W. Ashcroft and N. D. Mermin. **Solid State physics**. Harcout College Publishers, 1976.

[25] H. J. Monkhorst and J. D. Pack. **Special points for Brillouin-zone integrations.** Phys. rev. B, 13:5188, 1976.

[26] O. Jepsen and O. K. Andersen. **The Electronic Structure of h.c.p Ytterbium.** Solid State commun.9:1763, 1971.

[27] P. E. Blöchl, O. Jepsen and O. K. Andersen. **Theoretical Investigations of Ti-Based Binary Shape Memory Alloys.** Phys. rev. B, **49**:16223, 1994.

[28] N. D. Mermin. **Thermal Properties of the Inhomogeneous Electron Gas.** Phys. rev. A, **137**:1441, 1965.

[29] M. Methfessel and A. T. Paxton**. High-precision sampling for Brillouin-zone integration in metals.** Phys. rev. B, **40**:3616, 1989.

[30] V. R. Saunders, R. Dovesi, C. Roetti, M. Causa, N. M. Harrison, R. Orlando and C. M. Zicovich-Wilson. **CRYSTAL98 User's Manual: Computer Simulation of Materials at Atomic Level.** University of Torino, Torino, 1998.

[31] G. Gilat. **Analysis of methods for calculating spectral properties in solids.** J. Comp. Phys., **10**:432, 1972.

[32] L. Keinman and D. M. Bylander. **Efficacious Form for Model Pseudopotentials**. Phys. rev. Lett., **48:**1425, 1982.

[33] C. Hartwigsen, S. Goedecker and J. Hutter. **Relativistic separable dual-space Gaussian pseudopotentials from H to Rn.** Phys. rev. B, 58:3641, 1998.

[34] D. Vanderbilt. **Relativistic separable dual-space Gaussian pseudopotentials from H to Rn.** Phys. rev. B, **41**:7892, 1990.

[35] A. M. Rappe, K. M. Rabe, E. Kaxiras and J.D. Joannopoulos. **Soft self-consistent pseudopotentials in a generalized eigenvalue formalism. Optimized pseudopotentials.** Phys. rev. B, **41**:1227, 1990.

[36] R. Carr and M. Parrinello. **Unified Approach for Molecular Dynamics and Density-Functional Theory.** Phys. rev. Lett., **55:**2471, 1985.

[37] D. M. Wood and A. Zunger. **Nonlinear algorithm for the solution of the Kohn–Sham equations in solids.** J. Phys. A: Math. Gen., 18:1343, 1985.

[38] B. N. Parlett**. The Symmetric Eigenvalue Problem.** Prentice Hall Englewood Cliffs, New York, 1980.

[39] M. P. Teter, M. C. Payne and D. C. Allan. **Solution of Schrödinger's equation for large systems.** Phys. rev. B, **40**:12255, 1989.

[40] E. R. Davidson. **Methods in computational Molecular Physics.** Plenum, New York, 1983.

[41] W. H. Press, B. P. Flannery, S. A. teukolsky and W. T. Vetterling. **Numerical recipes in C . The Art of Scientific Computing Second Edition.** Cambridge University Press, New York, 1986.

[15-42]

[43] D. G. Anderson. **Convergence acceleration of iterative sequences. the case of scf iteration.** J. Assoc. Comput. Mach., **12**:547, 1965.

[44] P. Pulay. **Convergence acceleration of iterative sequences. the case of scf iteration.** Chem. Phys. Lett., 73:393, 1980.

[45] C. G. Broyden. ***A class of methods for solving nonlinear simultaneous equation.***. Math. Comput. Math. Comput., **19**:577, 1965.

[46] R. P. Feynman. **Forces in Molecules.** Phys. Rev., **56**:340, 1939.

[47] T. H. Fischer and J. J. Almlöf. **General methods for geometry and wave function optimization.** J. Phys. Chem, **96**:9768, 1992.

[48] P. E. Blochl. **Projector augmented-wave method.** Phys. Rev. B, **50**:17953, 1994.

[49] G. Kresse and D. Joubert. **From ultrasoft pseudopotentials to the projector augmented-wave method.** Phys. Rev. B, **59**:1758, 1999.

[50**]** ABINIT**. http://www.abinit.org**

[51] Perdew, J.P.; Burke, K.; Ernzerhof, M. **Generalized Gradient Approximation Made Simple**. Phys. Rev. Lett.; **1996**, 77, 3865-3868.

[52] Trouillier, N.; Martins, J.L. **Efficient pseudopotentials for plane-wave calculations.** Phys. Rev. B; 1991, 43, 3, 1993-2006 .

[53] Gonze, X.; Amadon, B.; Anglade, P.-M.; Beuken, J.-M.; Bottin, F.; Boulanger, P.; Bruneval, F.; Caliste, D.; Caracas, R.; Côté, M.; Deutsch, T.; Genovese, L.; Ghosez, Ph.; Giantomassi, M.; Goedecker, S.; Hamann, D. R.; Hermet, P.; Jollet, F.; Jomard, G.; Leroux, S.; Mancini, M.; Mazevet, S.; Oliveira, M. J. T.; Onida, G.; Pouillon, Y.; Rangel, T.; Rignanese, G.-M.; Sangalli, D.; Shaltaf, R.; Torrent, M.; Verstraete, M. J.; Zerah, G.; Zwanziger, J. W. **ABINIT:**
First-principles approach to material and nanosystem properties. Comput. Phys. Commun. 2009, 180, 2582-2615.

[54**]** M. A. Blanco, E. Francisco and V. Luana. **GIBBS: isothermal-isobaric thermodynamics of solids from energy curves using a quasi-harmonic Debye model.** Comput. Phys. Commun, 158:57, 2004.

[55] Birch, F. **Finite strain isotherm and velocities for single-crystal and polycrystalline NaCl at high pressure and 300°K.** Journal of geophysical Research: Solid Earth,83 (b3),(1978),pp. 1257-1268

CHAPTER III

CRYSTAL ELASTICITY

3.1. ELASTICITY IN SOLIDS: GENERAL IDEAS

The classic theory of elasticity studies the mechanics of solid bodies, considered these as continuous media and homogeneous. It ignores, therefore, the microscopic atomic structure. The connection with the theory of lattice vibrations begins by considering that at low temperature only the vibrational levels of low frequencies, corresponding to the acoustic branches, are active. As the wavelengths are very large, they no longer depend on the microscopic behavior of the crystal and can thus be assumed that the vibrational behavior of the crystal is that of a continuous medium. Under the application of external forces, the bodies are deformed in a varied and complex manner. In particular, a material is called elastic if the deformations caused by the application of external forces disappear completely after the elimination of these. The elastic constants relate the applied external forces (described by the stress tensor) to the original deformation (described by the strain tensor). They are, therefore, a key factor when determining the strength of a material. They also provide information from a fundamental point of view on the nature of the interatomic forces responsible for the cohesion and geometrical characteristics of the crystalline structure, as well as on the characteristics of the bond between adjacent atoms and their anisotropic character. Thermodynamically, they are linked to the specific heat, thermal expansion, Debye temperature, melting point and Grüneisen parameters. On the other hand, the mechanical stability of a phase is subjected to the fulfillment of certain conditions for the elastic constants, fixed by the crystalline symmetry of the crystal under study.

The study of the elastic constants under pressure is undoubtedly fundamental to deepen the knowledge of the interatomic interactions, the mechanical properties (for example, the synthesis of superhard materials), the mechanical stability of the phases and the mechanisms of phase transitions. In this sense, the violation of the conditions involving elastic constants necessary for mechanical stability is related to the presence of ferro-elastic phase transitions. In particular, the existence of a certain elastic constant or linear combination of these becoming negative when increasing the pressure can allow knowing the symmetry associated with the instability, thus allowing to obtain the symmetry of the phase that would emerge as stable (or metastable).

Traditionally, the study of elasticity in crystals starts from considering these as homogeneous and anisotropic continuous media and assuming that the stress and deformation are homogeneous.

The state of deformation of the crystal is given by the vector field $\vec{u}(\vec{r})$ (the so-called displacement field):

$$\vec{u}(\vec{r}) = \vec{r}' - \vec{r} \tag{3.1}$$

which gives for each point within the solid the change between its position vectors before $(\vec{r})$ and after $(\vec{r}')$ the deformation. Also, since the deformation is homogeneous, the position vector $\vec{r}$ and $\vec{r}'$ are related by a linear transformation:

$$r_i^{'} = \sum_{j=1}^{3} \alpha_{ij} r_j \tag{3.2}$$

Where the sub-indices i, j represent Cartesian coordinates and take the values x, y, z or 1, 2, 3 and the $\alpha_{ij} = \frac{\partial r_i'}{\partial r_j}$ are constants (independent of their position on the crystal) since the deformation is homogeneous. If we define the displacement gradients $u_{ij} = \frac{\partial u_i}{\partial r_j}$, the differentiation of the equation 3.1 expressed in its Cartesian components with respect to r_j compared with the definition of α_{ij} leads to the relationship between transformation coefficients and gradients displacement: $\alpha_{ij} = \delta_{ij} + u_{ij}$, from which it is evident that the u_{ij} are also constant in a homogeneous deformation. Equation 3.2 can, therefore, be rewritten as: $r_i' = \sum_{j=1}^{3}(\delta_{ij} + u_{ij})r_j$. The elements u_{ij} constitute a tensor of second rank, the strain tensor u. In general, the strain tensor u can be decomposed into a sum of two tensors $u = \varepsilon + \omega$, where ε is the symmetric tensor,

$$\epsilon_{ij} = \frac{1}{2}(u_{ij} + u_{ji}) \tag{3.3}$$

and ω is the antisymmetric tensor,

$$\omega_{ij} = \frac{1}{2}(u_{ij} - u_{ji}) \tag{3.4}$$

the tensor ω represents the rotation as a rigid body of the material, which is called rotation tensor. The physically relevant part of the deformation, compression (or dilatation) and shear deformation, is therefore found in the symmetric tensor ε, also known as an infinitesimal or Cauchy strain tensor [1], as it is only suitable for representing small deformations.

Another measure of the deformation is given by the change of distance between two points of the crystal. Thus, the relationship between the distances before and after the deformation is given by ,.

$$(dl')^2 = (dl)^2 + 2\sum_{i,j=1}^{3} \eta_{ij} dr_i dr_j \tag{3.5}$$

where lagrangian deformation parameters [2] are:

$$\eta_{ij} = \frac{1}{2}\left(u_{ij} - u_{ji} + \sum_{j=1}^{3} u_{ki}\, u_{kj}\right) = \frac{1}{2}\left(\sum_{j=1}^{3} \alpha_{ki}\, \alpha_{kj} - \delta_{ij}\right) \tag{3.6}$$

and they constitute the tensor of lagrangian deformation η, symmetric by definition ($\eta_{ij} = \eta_{ji}$). Alternatively, assuming the deformed final state as the reference state, defined in this case, $r_i = \sum_{j=1}^{3} \xi_{ij}\, \alpha'_j$ and the displacement gradients $u'_{ij} = \frac{\partial u_i}{\partial r'_j}$ the deformation can be defined as:

$$(dl')^2 = (dl)^2 + 2\sum_{i,j=1}^{3} e_{ij} dr_i dr_j \tag{3.7}$$

what allows to define the eulerian deformation tensor [3]:

$$e_{ij} = \frac{1}{2}\left(u'_{ij} - u'_{ji} + \sum_{j=1}^{3} u'_{ki}\, u'_{kj}\right) = \frac{1}{2}\left(\delta_{ij} - \sum_{j=1}^{3} \xi_{ki}\, \xi_{kj}\right) \tag{3.8}$$

At the limit of small deformations, the non-linear terms of the Lagrangian and Eulerian tensors cancel out, so that both definitions are equivalent and are reduced to the Cauchy strain tensor.

The fundamental difference between the tensors ε and η is the dependence of the former with the relative orientation of the deformed and original lattice, as opposed to the dependence with the metric tensor of the deformed lattice for the second,

$$\epsilon = \frac{1}{2}((\bar{M}')^{-1}\bar{M} + M(M')^{-1} - I\eta = \frac{1}{2}M(G' - G)\bar{M} \tag{3.9}$$

where M and M' are the matrices of orthonormalization of the original and deformed bases and G and G' the respective metric tensors.

When η is related to a change in the metric tensor of the unit cell geometry, it corresponds to a purely homogeneous deformation of the crystalline structure, leaving the fractional atomic coordinates fixed (network deformation). However, these coordinates may

vary in addition to the deformation of the network. It arises, the internal deformation, defined by the coordinate changes Δx_i for all the atoms in the asymmetry unit. The relaxation of the atomic positions minimizes the energy of the deformed network and is, therefore, a function of the deformation of the network. The change of the interatomic distance can be broken down into two separate effects:

$$\left(d'_{ij}\right)^2 - \left(d_{ij}\right)^2 = \left(\vec{x}_j - \vec{x}_i\right)\Delta G\left(\vec{x}_j - \vec{x}_i\right) + \left(\vec{x}_j - \vec{x}_i\right)G'\left(\Delta\vec{x}_j - \Delta\vec{x}_i\right) +$$

$$+\left(\Delta\vec{x}_j - \Delta\vec{x}_i\right)G'\left(\vec{x}_j - \vec{x}_i\right) + \left(\Delta\vec{x}_j - \Delta\vec{x}_i\right)G'\left(\Delta\vec{x}_j - \Delta\vec{x}_i\right) \quad (3.10)$$

where d'_{ij} and $d_{ij}$are the distances between the atoms i and j before and after the deformation. The first term comes only from the deformation of the network, while the second from the internal deformation.

Another tensor necessary to define the elastic properties of the crystal is the stress tensor. The field of forces is presented by the vector $\vec{p}$ (Force/Area), which is a function of the orientation of the surface element dS. Thus $\vec{p} = \vec{p}(\vec{n})$, where $\vec{n}$ is the unit vector perpendicular to dS. Moreover, the dependence is linear and is given by:

$$p_i = \sum_{h=1}^{3} \sigma_{ih}\, \eta_h \quad (3.11)$$

the coefficients σ_{ih} are components of the second rank stress tensor σ_{ij}, having a general component σ_{ij} the physical meaning of a pressure oriented along the direction i and acting on the surface dS normal to the Cartesian direction j. The diagonal values σ_{ii} are called normal components, while the components outside the diagonal are the tangential components of the stress. On the other hand, the tensor σ is symmetric $\left(\sigma_{ij} = \sigma_{ji}\right)$and not involving rigid rotations. An important particular case of stress is that of isotropic pressure (hydrostatic), $\sigma_{ij} = -p\delta_{ij}$ that occurs when all eigenvalues (the stress tensor can be diagonalized and its eigenvalues are real) are equal (The sign-comes from the convention of considering negative compressions and positive tensions).

In its original form, Hooke's law establishes a linear relationship between the longitudinal deformation ϵ and the stress σ of rods, $\sigma = E\epsilon$ (E = Young's modulus). The generalization of Hooke's law to crystals (anisotropic solids) is based on considering that each

of the stress tensor components is a linear homogeneous function of the deformation components. Thus,

$$\sigma_{ij} = \sum_{k,l=1}^{3} c_{ijkl}\, \eta_{kl} \tag{3.12}$$

or, in the same way,

$$\eta_{ij} = \sum_{k,l=1}^{3} s_{ijkl}\, \sigma_{kl} \tag{3.13}$$

c_{ijkl} has the physical meaning of the stress component σ_{ij}that must be applied to the crystal so that this deformation range is characterized by a unit value component η_{kl}.Similarly, the physical meaning of s_{ijkl} is that of the deformation component η_{ij} resulting from the application of the unit stressσ_{kl}. The coefficients c_{ijkl} and $s_{ijkl}$are components of the fourth-rank tensors $\boldsymbol{c}$ and $\boldsymbol{s}$. $\boldsymbol{c}$ is denominated tensor of elastic constants or coefficients of stiffness, whereas $\boldsymbol{s}$ is the tensor of the elastic modules or compliances. The two tensors are related by this generalized relationship:

$$\sum_{m,n=1}^{3} c_{ijmn}\, s_{mnhk} = \frac{1}{2}\left(\delta_{ih}\delta_{jk} + \delta_{ik}\delta_{jh}\right) \tag{3.14}$$

In contrast with η and σ which are field tensors, $\boldsymbol{c}$ and $\boldsymbol{s}$ are tensors dependent on the material and independent of the applied force field. As a consequence of the symmetry relations $\eta_{ij} = \eta_{ji}$ and $\sigma_{ij} = \sigma_{ji}$ for the tensors of strain and stress, respectively, the coefficients c_{ijkl} (s_{ijkl}) are invariant against the exchange of indices (ij), (kl) and (ij, kl) (symmetry of Voigt[4], thus fulfilling the relations:

$$c_{ijkl} = c_{jikl} = c_{ijlk} = c_{jilk} = c_{klij} = c_{lkij} = c_{klji} = c_{lkji} \tag{3.15}$$

Thus, the number of independent elements is reduced from 81 to 21. It is also possible to condense the pair of Cartesian indexes i, j by a single index α_i according to the scheme: $xx \equiv 1$, $yy \equiv 1$, $zz \equiv 1$, $yz(zy) \equiv 1$, $xz(xz) \equiv 1$ and $yx(xy) \equiv 1$, the elastic constants thus defined forming a symmetric matrix. The elastic constants c_{ii} with $i \leq 3$ are called longitudinal elastic constants, the c_{ii} with $i \geq 3$ are the tangential elastic constants. Those $c_{ij}$with $i \neq 3$are the non-diagonal constants and those $c_{ij}$with $i \leq 3$ and $j \geq 3$, which measure the tangential deformation produced by a longitudinal stress are the elastic mixing constants

The presence of crystalline symmetry further reduces the number of independent elastic constants. In principle, it is clear that certain constants will be equal to each other or will be related to being equivalent deformations in the crystal. In general, for each generator R of the point group of a given crystalline class (excluding the inversion centre, since the elasticity is a center−symmetric property), the components c_{pq} are transformed into c'_{pq}, and the condition must be fulfilled (by symmetry) $c'_{pq} = c_{pq}$, which forces the cancellation of certain elastic constants.

In particular, the number of independent elastic constants for hexagonal and cubic crystals (which will be treated in detail in our case) is reduced to 5 and 3, respectively.

3.2. ELASTIC CONSTANTS UNDER PRESSURE

The evaluation of elastic constants of materials under hydrostatic pressure [5] is not trivial. In fact, its description does not present a uniform nomenclature and the terminology used is confused. Thus, they can be defined as second derivatives of the internal energy U (adiabatic elastic constants) or free energy of Helmholtz (elastic isothermal constants) with respect to parameters of finite deformation u, homogeneous infinitesimal deformations ϵ, or parameters of homogeneous finite deformation eulerians or lagrangians ϵ and η. They also correspond to the coefficients of transformation between stress and homogeneous deformation for the different definitions of homogeneous deformation, or to the coefficients of the equations of motion. Moreover, some authors postulate that the elastic constants under pressure are given by secondary derivatives of the Gibbs free energy with respect to eulerians homogeneous deformations $\boldsymbol{e}$. All these definitions are equivalent to zero pressure, but they differ from non-zero pressures.

We focus on the traditional definition of elastic constants as second derivatives of internal energy versus lagrangians homogeneous deformations η_i [6]. We start from a glass compressed by hydrostatic pressure p to the density ρ_1. Before homogenous and small deformations each vector of the Bravais network $\vec{R}$ of the original network passes to the new position $\vec{R}'$ in the compressed or expanded network.

$$R'_i = \sum_j (\delta_{ij} + \varepsilon_{ij}) R_j \tag{3.16}$$

Where ε_{ij} are independent constants of $\vec{R}$ (since the deformation is homogeneous), which satisfies that $\varepsilon_{ij} = \varepsilon_{ji}$, indicating the subindices i and j cartesian components, taking, therefore, values $1, 2\ and\ 3$. The expansion of internal energy per unit of mass of the crystal in terms of the lagrangian strain tensor (rotation excluded),

$$\eta_{ij} = \varepsilon_{ij} + \frac{1}{2}\sum_k \varepsilon_{ik}\varepsilon_{kj} \tag{3.17}$$

leads to the expression:

$$E(\rho_1, \eta_{mn}) = E(\rho_1, 0) + \frac{1}{\rho_1}\sum_{ij} T_{ij}\eta_{ij} + \frac{1}{2}\left(\sum_{ijkl} C_{ijkl}\eta_{ij}\,\eta_{kl} + \cdots\right) \tag{3.18}$$

Where $E(\rho_1, \eta_{mn})$ is the energy of the deformed crystal (with relaxation of the atomic coordinates in the lattice of distorted Bravais lattice), the elements T_{ij} are the components of the deformation tensor before the deformation:

$$T_{ij} = \rho_1\left[\frac{\partial E(\rho_1, \eta_{mn})}{\partial \eta_{ij}}\right]_{\eta_{mn}} \tag{3.19}$$

Which, in conditions of initial hydrostatic pressure are given by:

$$T_{ij} = -p\delta_{ij} \tag{3.20}$$

and C_{ijkl} are the elastic constants of the crystal at an arbitrary hydrostatic pressure

p:$C_{ijkl} = \rho_1\left[\frac{\partial^2 E(\rho_1, \eta_{mn})}{\partial \eta_{ij}\partial \eta_{kl}}\right]_{\eta_{mn}=0}$. By expressing the deformation parameters ε_{ij} as a function of an infinitesimal parameter γ,

$$\varepsilon_{ij} = s_{ij}\gamma + e_{ij}\gamma^2 + \cdots \tag{3.21}$$

and include equations 3.17 and 3.20 in equation 3.18, this can be written as:

$$E(\rho_1, \eta_{mn}) = E(\rho_1, 0) + A\gamma + \frac{D}{2}\gamma^2 + \cdots \tag{3.22}$$

where

$$A = \frac{p}{\rho_1}\sum_i s_{ii} \text{ and} D = \frac{1}{\rho_1}\sum_{ijkl} C_{ijkl}s_{ij}s_{kl} - \frac{2p}{\rho_1}\sum_{ik}(e_{ik}\delta_{ik} + \frac{s_{ki}}{2}^2) \tag{3.23}$$

It is clear, then, that the derivatives of the total energy with respect to Υ lead to linear combinations of the elastic constants C_{ijkl}:

$$\sum_{ijkl} C_{ijkl} s_{ij} s_{kl} = 2p \sum_{ik} \left(e_{ik} \delta_{ik} + \frac{s_{ik}^2}{2} \right) + \rho_1 \left[\frac{\partial^2 E(\rho_1, \gamma)}{\partial \gamma^2} \right]_{\gamma=0} \quad (3.24)$$

The equation is valid for any deformation, regardless of whether it retains the volume or not. It is clear, also, that under conditions of zero pressure, it is reduced to the traditional definition of elastic constants in the absence of pressure. Using the properties of symmetry of the matrices $\hat{S}$ and $\hat{C}$, the notation of Voigt: $xx \equiv 1$, $yy \equiv 1$, $zz \equiv 1$, $yz(zy) \equiv 1$, $xz(xz) \equiv 1$ and $yx(xy) \equiv 1$ and entering a parameter:

$$\xi_\alpha = \begin{cases} 1, \alpha = 1,2,3; \\ 2, \alpha = 4,5,6. \end{cases}$$

Equation 3.18 is rewritten as:

$$\sum_{\alpha\beta} \xi_\alpha \xi_\beta C_\alpha s_\alpha s_\beta = 2p \sum_\alpha (2 - \xi_\alpha) e_\alpha + p \sum_\alpha \xi_\alpha s_\alpha^2 + \rho_1 \left[\frac{\partial^2 E(\rho_1, \gamma)}{\partial \gamma^2} \right]_{\gamma=0} \quad (3.25)$$

3.2.1. RELATIONSHIP BETWEEN THE COMPRESSIBILITY MODULUS AND THE ELASTIC CONSTANTS

The compressibility module of a crystal can be expressed as a certain linear combination of elastic constants. To obtain the relationship between the compressibility module and the elastic constants, it is only necessary to consider the application of hydrostatic pressure to the system. This leads to a homogeneous deformation of the type:

$$\varepsilon_{ij} = t_i(\gamma) \delta_{ik} \quad (3.26)$$

in which the value of the functions $t_i(\gamma)$is determined by the crystalline symmetry. Thus, in a hexagonal crystal, $t_1 = t_2 = \gamma$ and $t_3 = \beta(\gamma)$, the value of $\beta(\gamma)$being specified with the volume of the parameter c/a.

$$\frac{c}{a} = \frac{1+\beta(\gamma)}{1+\gamma} \varphi(V_1) \quad (3.27)$$

Where $\varphi(V_1)$is the value of c/a corresponding to the density $\rho_1 = \frac{1}{V_1}$ to which the crystal has been compressed or expanded by the application of hydrostatic pressure. The value of c/a can then be expanded as a function of the specific volume V,

$$\frac{c}{a} = \varphi(V) = \varphi(V_1)\left[1 + \frac{\mu}{V_1}(V - V_1) + \cdots\right] \tag{3.28}$$

with

$$\mu = \frac{V_1}{\varphi(V_1)}\left[\frac{d\varphi(V)}{dV}\right]_{V=V_1} \tag{3.29}$$

Comparing equations 3.27 and 3.28 and defining the volume associated with deformation 3.26 as a function of Υ,

$$V = V_1(1 + \Upsilon)^2\big(1 + \beta(\Upsilon)\big) \tag{3.30}$$

We obtain:

$$\beta(\Upsilon) = \frac{(1-\mu)(1+\Upsilon)}{1-\mu(1+\Upsilon)^3-1} \tag{3.31}$$

As the energy associated with deformation 3.26 only worked on the specific volume, we arrived, after the inclusion of the compressibility module definitions and the pressure:

$$B = V\frac{d^2E}{dV^2} \quad \text{and} \quad p = -\frac{dE}{dV} \tag{3.32}$$

to the expression:

$$\rho_1\left[\frac{d^2E}{d\Upsilon^2}\right]_{\Upsilon=0} = \frac{B}{V_1^2}\left[\left(\frac{dV}{d\Upsilon}\right)^2\right]_{\Upsilon=0} - \frac{p}{V_1}\left[\frac{d^2V}{d\Upsilon^2}\right]_{\Upsilon=0} = \frac{9B}{(1-\mu)^2} - 6\frac{(1+2\mu)}{(1-\mu)^2}p \tag{3.33}$$

As noted, in hexagonal crystals there are five independent elastic constants: $C_{11}, C_{11}, C_{13}, C_{33}\ and\ C_{44}$; the rest of the elastic constants are determined by symmetry:

$$C_{22} = C_{11}, C_{13} = C_{23},\ C_{55} = C_{44},\ C_{66} = \frac{1}{2}(C_{11} - C_{12}) \tag{3.34}$$

or they are null. The first term of equality 3.33 is obtained through the substitution in equation 3.25 of the parameters associated with deformation 3.25.

$$s_1 = s_2 = 1,\ e_1 = e_2 = 0,\ s_3 = \frac{1+2\mu}{1-\mu} y e_3 = \frac{(6\mu+3\mu^2)}{(1-\mu)^2} \tag{3.35}$$

These last two obtained by the Taylor series of $t_3 = \beta(\Upsilon)$ and after considering the equalities between elastic constants 3.34. The general expression of the relationship between elastic constants and the compressibility module in hexagonal crystals is thus reached:

$$2C_{11} + 2C_{12} + 4\frac{1+2\mu}{1-\mu}C_{13} + \left(\frac{1+2\mu}{1-\mu}\right)^2 C_{33} = \frac{9B}{(1-\mu)^2} - 3\frac{1-4\mu^2}{(1-\mu)^2}p \tag{3.36}$$

that under conditions of zero pressure is reduced to:

$$2C_{11} + 2C_{12} + 4\frac{1+2\mu}{1-\mu}C_{13} + \left(\frac{1+2\mu}{1-\mu}\right)^2 C_{33} = \frac{9B}{(1-\mu)^2} \tag{3.37}$$

An alternative strategy to obtain the relation of the compressibility module with the elastic constants starts from equation 3.13. Before the application of hydrostatic pressure $(\sigma_{kl} = -p\delta_{kl})$, this equation can be written as:

$$\eta_{ij} = -\sum_{k=1}^{3} p\, s_{ijkk} \tag{3.38}$$

Since the tensor of the deformations is symmetrical and considering that these are small, the relative change of volume of the solid is given by the sum of the principal components of the deformation tensor:

$$\Delta = \sum_{i=1}^{3} \eta_{ij} = -\sum_{k=1}^{3} p\, s_{ijkk} \tag{3.39}$$

and, therefore, the compressibility $\kappa = \frac{-\Delta}{p}$ is $\sum_{k=1}^{3} s_{ijkk}$, corresponding, thus, the compressibility to the sum of the new coefficients in the upper left scheme of the compliances matrix. The compressibility module is obtained directly by being the reciprocal of the compressibility:

$$B = \frac{1}{\kappa} = \frac{1}{s_{11}+s_{22}+s_{33}+2(s_{12}+s_{23}+s_{31})} \tag{3.40}$$

and, in hexagonal crystals, because of the equalities between compliances it is reduced to:

$$B = \frac{1}{2s_{11}+s_{33}+2s_{12}+4s_{31}} \tag{3.41}$$

Moreover, using the relations between elastic constants and compliances, the compressibility module can be rewritten as:

$$B = \frac{c_{33}(c_{11}+c_{12})-2c_{13}^2}{c_{11}+c_{12}+2c_{33}-4c_{31}} \tag{3.42}$$

The connection between equations 3.37 and 3.42 comes from the definition of the parameter μ (3.29). Developing the derivative,

$$\frac{V_1}{\left(\frac{c}{a}\right)_1}\left[\left(\frac{\frac{dc}{dV}a-c\frac{da}{dV}}{a^2}\right)\right]_{V_1} = V_1\left[\left(\frac{1}{c}\frac{dc}{dV}-\frac{1}{a}\frac{da}{dV}\right)\right]_{V_1} \tag{3.43}$$

and, after including the dependency of the parameters with the pressure:

$$V_1\left[\left(\frac{1}{c}\frac{dc}{dp}\frac{dp}{dV}-\frac{1}{a}\frac{da}{dp}\frac{dp}{dV}\right)\right]_{V_1} = B(\kappa_a-\kappa_c) = B(\kappa_c-\kappa_a) \tag{3.44}$$

that is, the dependence on the quotient $\frac{c}{a}$ is related to the difference between the lineal compressibilities along the $a\ and\ c$ ($\kappa_a\ and\ \kappa_c$).Under pressure, the deformation of a line in the direction of the unit vector $\vec{l}_i$ is:

$$\eta_{ij}\vec{l}_i\vec{l}_j = -p\sum_{k=1}^{3} s_{ijkk}\vec{l}_i\vec{l}_j \tag{3.45}$$

and, therefore, the linear compressibility is:

$$\beta = \sum_{k=1}^{3} s_{ijkk}\vec{l}_i\vec{l}_j \tag{3.46}$$

in a hexagonal system,

$$\kappa_a = s_{11}+s_{12}+s_{13} \ \text{ and } \ \kappa_c = 2s_{13}+s_{33} \tag{3.47}$$

or, depending on the elastic constants,

$$\kappa_a = \frac{c_{33}-c_{13}}{c_{33}(c_{11}+c_{12}-2c_{13}^2)} \ \text{ and } \ \kappa_c = \frac{(c_{11}+c_{12})-2c_{13}}{c_{33}(c_{11}+c_{12}-2c_{13}^2)} \tag{3.48}$$

the combination of equations 3.44, 3.42 and 3.48 allows the μ parameter to be rewritten as:

$$\mu = \frac{(c_{11}+c_{12})-c_{33}-c_{13}}{c_{11}+c_{12}+2c_{33}-4c_{31}} \tag{3.49}$$

and, after its inclusion in equation 3.37, the equivalence with the equation 3.42 is checked.

If in equation 3.36 the requirement that $\frac{c}{a}$ is independent of volume (μ = 0) is added, we arrive at:

$$B = \frac{1}{9}(2C_{11} + 2C_{12} + 4C_{13} + C_{33} + 3p) \tag{3.50}$$

This simple equation allows, therefore, to estimate the compressibility module in those systems in which c/a does not change appreciably with the volume and to fix a limit superior to the same in those with substantial change in the quotient.

Equation 3.36 also allows to obtain the real relation between elastic constants and compressibility module for a cubic crystal, considering constant the relation c/a (in a cubic crystal: $a = b = c$) and introducing the cubic crystals own relationships $C_{33} = C_{11}$ and $C_{13} = C_{12}$. So we get to the expression,

$$B = \frac{1}{3}(C_{11} + 2C_{12} + p) \tag{3.51}$$

which allows to evaluate the compressibility module under pressure conditions.

3.2.2. MECHANICAL STABILITY OF CRYSTALS UNDER HYDROSTATIC PRESSURE

Equation 3.22 can be written as:

$$\Delta E = E(\rho_1, \Upsilon) - E(\rho_1, 0) = -p\Delta V + \Delta E_{in} \tag{3.52}$$

where ΔV is the variation of the volume with the deformation:

$$\Delta V = V_1[|I + \varepsilon| - 1]$$

$$= V_1\Upsilon(\textstyle\sum_i s_{ii}) + \frac{V_1\Upsilon^2}{2}[2(\sum_i e_{ii}) + (\sum_i e_{ii})^2 - \sum_{ij} {s_{ij}}^2] \tag{3.53}$$

and

$$\Delta E_{in} = \frac{V_1\Upsilon^2}{2}\left[p\left(\sum_i s_{ii}\right)^2 - 2p\sum_{ij} s_{ij}^2 + \sum_{ijkl} c_{ijkl}\, s_{ij}s_{kl}\right] + \cdots$$

$$= \frac{V_1 \gamma^2}{2} \sum_{\alpha\beta} \{\xi_\alpha \xi_\beta C_{\alpha\beta} + p[(2-\xi)(2-\xi_\alpha) - 2\xi_\alpha \delta_{\alpha\beta}]\} s_\alpha s_\beta + \cdots$$

$$= \frac{V_1 \gamma^2}{2} \sum_{\alpha\beta} C_{\alpha\beta}\, s_\alpha s_\beta + \cdots \tag{3.54}$$

and rewrite as:

$$\Delta E_{in} = \frac{V_1}{2} \sum_{\alpha\beta} \tilde{C}_{\alpha\beta}\, \varepsilon_\alpha \varepsilon_\beta \tag{3.55}$$

where the $\varepsilon_\alpha$are infinitesimal eulerian deformations and the $\tilde{C}_{\alpha\beta}$form a symmetric matrix and depend on the traditional elastic constants (defined as second derivatives of the energy with respect to lagrangian deformations η_i). Unlike the latter, the new elastic constants $\tilde{C}_{\alpha\beta}$ do not have the exchange symmetry $(\alpha\beta) \leftrightarrow (\sigma\tau)$, although they remain symmetric with respect to the exchanges $(\alpha\beta) \vee (\sigma\tau)$. Its relationship with the traditional elastic constants, extractable from Eq. 2.54, can be summarized in a set of expressions:

$$\tilde{C}_{\alpha\beta} = \xi_\alpha \xi_\alpha (C_{\alpha\alpha} - p), \alpha = 1,2, \ldots ,6;$$

$$\tilde{C}_{\alpha\beta} = \xi_\alpha \xi_\beta C_{\alpha\beta}, \alpha = 1,2,3, \beta = 4,5,6;$$

$$\tilde{C}_{12} = C_{12} + p, \tilde{C}_{13} = C_{13} + p, \tilde{C}_{23} = C_{23} + p;$$

$$\tilde{C}_{45} = 4C_{45}, \tilde{C}_{46} = 4C_{46}, \tilde{C}_{56} = 4C_{56}. \tag{3.56}$$

An alternative approach to the problem of elasticity under pressure consists of using the Gibbs free energy $G(p,T) = E(p,T) + pV(p,T)$ instead of the energy to estimate the elastic constants. The reason given is that at fixed $p\ and\ T$, the structure in equilibrium is given by a minimum of G and not of E. The elastic constants thus defined (effective elastic constants) take, therefore, the form:

$$\tilde{C}_{\alpha\beta} = \frac{1}{V_1} \left(\frac{\partial^2 G}{\partial \varepsilon_\alpha \partial \varepsilon_\beta} \right)_{p=cte} \tag{3.57}$$

where ε_α are Eulerian deformations. Formally, at $T = 0$, the crystals subjected to deformation are not normally in equilibrium, so it is impossible to determine the free energy of Gibbs G or any other thermodynamic potential. It is resorted, then, to consider the function

$$G(p, \varepsilon_1, \ldots, \varepsilon_6) = E(p, \varepsilon_1, \ldots, \varepsilon_6) + pV(p, \varepsilon_1, \ldots, \varepsilon_6) \tag{3.58}$$

which allows the effective elastic constants $\tilde{C}_{\alpha\beta}$ to be equivalent to the effective elastic constants $\tilde{C}_{\alpha\beta}$ defined in equation 3.55. Given that both definitions are equivalent, the motive after the use in the realized calculations of the energy E instead of the free energy of Gibbs G is only of computational type, since it is easier to determine the equilibrium parameters of a structure crystalline from E (at fixed V, the minimum energy for the structure in equilibrium) than from G. Moreover, the calculations at fixed V are simpler than those at fixed p. It should also be noted that the elastic constants $\tilde{C}_{\alpha\beta}$ are equivalent to the previously defined stress-strain coefficients.

The requirement of crystalline mechanical stability [7] leads to the inequation $\Delta E_{in} \geq 0$, which is fulfilled only if the symmetric matrix:

$$\hat{G} = \begin{vmatrix} \tilde{C}_{11} & \tilde{C}_{12} & \tilde{C}_{13} & \tilde{C}_{14} & \tilde{C}_{15} & \tilde{C}_{16} \\ \tilde{C}_{21} & \tilde{C}_{22} & \tilde{C}_{23} & \tilde{C}_{24} & \tilde{C}_{25} & \tilde{C}_{26} \\ \tilde{C}_{31} & \tilde{C}_{32} & \tilde{C}_{33} & \tilde{C}_{34} & \tilde{C}_{35} & \tilde{C}_{36} \\ \tilde{C}_{41} & \tilde{C}_{42} & \tilde{C}_{43} & \tilde{C}_{44} & \tilde{C}_{45} & \tilde{C}_{46} \\ \tilde{C}_{51} & \tilde{C}_{52} & \tilde{C}_{53} & \tilde{C}_{54} & \tilde{C}_{55} & \tilde{C}_{56} \\ \tilde{C}_{61} & \tilde{C}_{62} & \tilde{C}_{63} & \tilde{C}_{64} & \tilde{C}_{65} & \tilde{C}_{66} \end{vmatrix}$$

has a positive determinant.

This leads, in turn, to different stability criteria. Depending on the symmetry of the crystal and shows that the mechanical stability under pressure conditions is not only a property of the material, but depends on the applied pressure, reducing in the limit of $p = 0$ to the Born criteria, which involve only the traditional elastic constants.

Thus, in a cubic crystal, the eigenvalues of the matrix $\hat{G}$ are:

$$\mu_1 = \tilde{C}_{11} + 2\tilde{C}_{12}, \qquad \mu_2 = \mu_3 = \tilde{C}_{11} - \tilde{C}_{12} \; and \; \mu_4 = \mu_5 = \mu_6 = \tilde{C}_{44}$$

Considering the fact that the annulment of the determinant implies mechanical instability, the criteria of mechanical instability, in terms of the traditional elastic constants, are:

$C_{11} + 2C_{12} + p = 0$, $C_{11} - 2C_{12} - 2p = 0$ and $C_{44} - p = 0$,

associated with the deformation eigenvectors:

$(\Upsilon,\Upsilon,\Upsilon,0,0,0);\ (\Upsilon_{xx},\Upsilon_{yy},\Upsilon_{zz},0,0,0)\ ;\Upsilon_{xx}+\Upsilon_{yy}+\Upsilon_{zz}=0$ and $(0,0,0,\Upsilon,0,0)$

The interpretation of these criteria is clear, and is none other than the generalization under pressure conditions of the compressibility module and the two modules of transverse elasticity under conditions of zero pressure.

In this sense, the first criterion is related to a volumetric deformation as indicated by the associated eigenvector. The meaning of this instability is the de-cohesion of the net by pure dilatation. It is the spinodal instability since it involves the cancellation of the compressibility module, defined under pressure conditions such as:

$$B_T=\frac{1}{3}\left(\tilde{C}_{11}+2\tilde{C}_{12}\right)=\frac{1}{3}(C_{11}+2C_{12}+p).$$

The second instability, known as Born's instability [8], involves breaking symmetry with volume conservation. The modulus that is canceled in this case is the tetragonal transverse elastic modulus, defined under pressure conditions such as:

$$G'=\frac{1}{2}\left(\tilde{C}_{11}-\tilde{C}_{12}\right)=\frac{1}{2}(C_{11}-C_{12}-p).$$

Finally, the third instability is the transverse deformation, with volume conservation, along one of the directions of symmetry, being in this case the module associated with the transversal elastic. The complexity of $G=\tilde{C}_{44}=4C_{44}-p$ stability condition increases in crystals of lower symmetry. Thus, in a hexagonal crystal the values of the determinant $\hat{G}$ are:

$$\mu_1=\tilde{C}_{11}-2\tilde{C}_{12},\mu_2=\frac{1}{2}\{\left(\tilde{C}_{11}+\tilde{C}_{12}+\tilde{C}_{33}\right)+\left[\left(\tilde{C}_{11}+\tilde{C}_{12}-\tilde{C}_{33}\right)^2++8\tilde{C}_{13}^2\right]^{\frac{1}{2}}\},$$

$$\mu_3=\frac{1}{2}\{\left(\tilde{C}_{13}^2+2\tilde{C}_{12}+\tilde{C}_{33}\right)-\left[\left(\tilde{C}_{11}+\tilde{C}_{12}-\tilde{C}_{33}\right)^2+8\tilde{C}_{13}^2\right]^{\frac{1}{2}}\},\ \mu_4=\mu_5=\tilde{C}_{44}$$ and

$\mu_6=\tilde{C}_{66}$.For both μ_2 and μ_3 to be positive, it is a necessary condition that $\mu_2+\mu_3$ and $\mu_2\mu_3$ are positive. The stability conditions are then:

$$\tilde{C}_{11}-\tilde{C}_{12}>0\ \ \tilde{C}_{44}>0\ \ \tilde{C}_{66}>0,$$

$$\tilde{C}_{11}+\tilde{C}_{12}+\tilde{C}_{33}>0(\text{de}\ \ \mu_2+\mu_3>0)$$

$$\text{and}\ \ \left(\tilde{C}_{11}-\tilde{C}_{12}\right)\tilde{C}_{33}-2\tilde{C}_{13}^2>0\ (de\mu_2\mu_3>0)$$

Expressions that can be simplified in the inequations:

$$\tilde{C}_{44} > 0, \qquad \tilde{C}_{11} > \tilde{C}_{12} \; and \; \tilde{C}_{33}(\tilde{C}_{11} + \tilde{C}_{12}) > 2\tilde{C}_{13}^2$$

3.2.3. EVALUATION OF ELASTIC CONSTANTS

For a given crystal, it is possible to calculate all M independent elastic constants by imposing M small deformations to the unit cell. Each one of the deformations is parameterized with a variable, (see equation 3.21). This allows estimating the total energy of the system for different variable values. The positions of the atoms must be redefined in each distorted configuration due to the appearance of internal deformation before the decrease in symmetry associated with the deformation. Assuming the validity of Hooke's law for small values of Υ, the numerical data $E(\Upsilon)$is adjusted to the expansion of the Taylor order of equation 2.22, where $V_1 = \frac{1}{\rho_1}$, $E(\rho_1, 0)$ and C_{ijkl} are fitting parameters. Finally, the inclusion of the quadratic terms, $\frac{\partial^2 E}{d\Upsilon^2}$, in equation 3.25 allows access to a system of M linear equations for the elastic constants, which allows extracting these.

In our case, we consider the calculation of the elastic constants of cubic (zinc benzene) phases of the SiC and ZnO, (NaCl) phase of ZnO, (CsCl) phase of ZnO and hexagonal (wurtzite) phases of the SiC and ZnO with the objective of examining its metastability. The parametrization of the deformations chosen in each case is shown in Table 6.1. For each, we choose 11 values of Υ in the interval [-0.05; 0.05] in order to remain in the elastic limit and avoid the contribution of terms of order higher than 2 in the expansion of the energy. Likewise, we relax the internal degrees of freedom in all cases where, by inducing a reduction in symmetry, the deformation causes the atoms to stop locating in special positions without free parameters, being, therefore, the optimization of these necessary. It should be noted that if the atoms are in inversion centers, these remain stable under small deformations. Then, it is unnecessary to relax the internal parameters in the deformed network, which greatly simplifies the calculations. It also ensures the convergence of energy versus the number of points k. We choose, thus, Monkhost-Pack grids with a number of points k in the irreducible part of the Brillouin area of 280, and 427 for the cubic zinc bende and hexagonal wurzite cells, respectively, extending this numbers in the structures of lower symmetry associated with deformations. We also verify the energetic convergence in $\Upsilon = 0$,

independently of the deformation and, therefore, of the different symmetries and grid points k.

Although the calculation of the three independent elastic constants of the cubic networks would only require the application of three independent deformations, we have included in Table 3.1 two additional deformations for the purpose of analyzing the precision of the calculations.

The first and third deformations correspond to tetragonal distortions of the lattice. In the first, the value of the axes $a\ and\ b$ is modified in the same magnutid, keeping the fixed c axis, while in the third only the axis a changes. From the combination of both we extract the value of the two independent constants C_{11} and C_{12}.. The second deformation is an orthorhombical transversal distortion, through which the constant C_{44} is accessed. It has the advantage, compared to the previous deformations, that in it the energy is an even function of the deformation $E(\Upsilon) = E(-\Upsilon)$ so that the number of calculations made is reduced by half.

On the other hand, the advantages of the fourth and fifth deformations on the other three come from the conservation of the volume $(det\vee I + \varepsilon \vee 1)$since it is the same as before the deformations. In the first place, this allows the elimination of the term $p\Delta V$ in equation 3.52, with which we obtain, directly, the elastic constants $\tilde{C}_{\alpha\beta}$. In second place, known the strong dependence of the energy with the volume, we avoid the separation of this contribution in the total energy. Thirdly, by keeping the volume we minimize the base changes and with it the computational uncertainties. In particular, the fourth deformation corresponds to an extension of the first deformation, to which is added the term of distortion ε_{33} in order to maintain the volume. This leads to a tetragonal distortion in which the axes $a\ and\ b$ remain the same and different from the c axis. The meaning associated with the variations of the parameter Υ is that of the modification of the quotient $c/a$of the new tetragonal structure at constant volume, $\frac{c}{a} = \frac{1}{(+\Upsilon)^3}$. The only difficulty associated with distortion is the need to expand the deformation component ε_{33} in Taylor series to obtain the expansion values in powers of the infinitesimal Υ, $s_{33} = -2$, $e_{33} = 3$. The introduction of these in the equation 3.2 leads to the linear combination of elastic constants shown in Table 3.1, coinciding with $6(\tilde{C}_{11} - \tilde{C}_{12})$. The fifth distortion is an ortho-mast cross-sectional distortion of the network, which makes it possible to obtain the transverse elastic modulus $\tilde{C}_{44}$ directly. Using these last

two deformations and the relation 3.51, we obtain the three independent elastic constants, with a deviation of less than 3% with respect to those previously obtained.

It is also important to note that although the distortions are applicable independently of the space group and the number of non-equivalent atoms of the cubic cell, they do have an influence on the symmetry of the distorted lattice. Thus, in the simple cubic $A1$ lattice, distortions 1, 3, and 4 lead to simple tetragonal lattices and distortions, 2 and 5 to orthorhombic networks centered in the base, while in $A1$ spinel type all distortions lead to body centered lattices, regardless of whether they are tetragonal or orthorhombic.

Table 3.1: Deformations used for the calculations of elastic constants in cubic and hexagonal structures.

Symmetry	Deformation	Parameter	$\rho_1 \left[\frac{\partial^2 E(\rho_1,\Upsilon)}{\partial \Upsilon^2}\right]_{\Upsilon=0}$
Cubic	1	$\varepsilon_{11} = \varepsilon_{22} = \Upsilon$	$2(C_{11} + C_{12} - p)$
	2	$\varepsilon_{13} = \varepsilon_{31} = \Upsilon$	$4C_{44} - 2p$
	3	$\varepsilon_{13} = \Upsilon$	$C_{11} - p$
	4	$\varepsilon_{11} = \varepsilon_{22} = \Upsilon,$ $\varepsilon_{13} = (1+\Upsilon)^{-2}$	$-16(C_{11} - C_{12}) - 12p$
	5	$\varepsilon_{11} = \varepsilon_{22} = \Upsilon,$ $\varepsilon_{13} = \left(1-\Upsilon^2\right)^{-1}$	$-14(C_{44} - p)$
Hexagonal	1	$\varepsilon_{11} = \varepsilon_{33} = \Upsilon$	$2(C_{11} + C_{13} + C_{33} - 2p$
	2	$\varepsilon_{11} = -\varepsilon_{22} = \Upsilon$	$2(C_{11} - C_{12} - p)$
	3	$\varepsilon_{11} = \varepsilon_{22} = \Upsilon$	$2(C_{11} + C_{12} - p)$
	4	$\varepsilon_{13} = \varepsilon_{31} = \Upsilon$	$4C_{44} - 2p$
	5	$\varepsilon_{33} = \Upsilon C_{33} - p$	
	6	$\varepsilon_{13} = \varepsilon_{31} = \Upsilon,$ $\varepsilon_{22} = \frac{\Upsilon^2}{(1-\Upsilon^2)}$	$4(C_{44} - p)$
	7	$\varepsilon_{11} = -\varepsilon_{22} = \Upsilon,$ $\varepsilon_{33} = \frac{\Upsilon^2}{(1-\Upsilon^2)}$	$2(C_{11} - C_{12} - 2p)$

The elastic constants of the ecliptic graphite lattice are obtained through the 5 primary deformations of Table **3.1** The first corresponds to a modification of axes a *and* c. It is, therefore, an orthorhombic distortion. The second one (also orthorhombic) deforms the basal plane by elongation along a and along b. The third maintains the hexagonal symmetry, modifying in it the value of axes a *and* b in the same amount. The fourth, in which the energy is an even function of the deformation, decreases the hexagonal to monoclinic symmetry and

the fifth retains the hexagonal symmetry by compressing or expanding the c axis. In all these deformations the volume changes. With verification effects, two other deformations were applied, in which the volume, the monoclinic deformation 6 and the orthorhombic deformation 7 were conserved. It was found that the modifications in the elastic constants were less than 4%.

References

[1] Slaughter, William S. ***The Linearized Theory of Elasticity*.** New York: Springer Science+Business Media (2002).

[2] Ritter, R. M. ***The Oxford Style Manual*.** Oxford University Press (2003).

[3] Spencer, A.J.M. ***Continuum Mechanics*.** Longman Group Limited (London) (1980).

[4] Woldemar Voigt. ***Lehrbuch der kristallphysik*.** Teubner, Leipzig (1910).

[5] 5J. M. Recio, J. M. Menéndez and A. Otero-de-la-Roza Eds. **An Introduction to High-Pressure Science and Technology.** CRC Press (2015).

[6] G. V. Sin'ko and N. A. Smirnov.*Ab initio* calculations of elastic constants and thermodynamic properties of bcc, fcc, and hcp Al crystals under pressure. **J. Phys.: Condens. Matter, 14:6989, 2002**

[7] S.P. TIMOSHENKO and J. M. GERE. ***Theory of Elastic Stability* (2nd ed).** New York: McGraw-Hill, 1961.

[8] J. Wang, J. Li, S. Yip, D. Wolf, S. Phillpot. **Unifying two criteria of Born: Elastic instability and melting of homogeneous crystals.** Physica A: Statistical Mechanics and its Applications Vol. 240, Issues 1–2, 1997, 396-403.

CHAPTER IV

APPLICATIONS to COVALENT, IONIC and LAYERED MATERIALS

A clear understanding of cohesive and mechanical properties of technological materials is of capital importance especially when applications are demanded in hostile thermal, stress and chemical environments. Since the nature of the crystalline bonding networks is the ultimate responsible for the response of the compounds to these external conditions, it is rewarding and necessary investigating how macroscopic properties correlate with the chemical interactions at an atomic level. Covalent, ionic and layered solids constitute three crystal families currently displaying interest in a variety of areas such as electronics and solar cell industries [1–3]. These compounds provide a good target to examine how changes in strong and weak interactions affect the observed elastic stability of materials. To this end, computer simulations constitute a practical research route to microscopically analyze strained structures of solids since geometries optimized by minimizing the crystal energy can be accurately obtained from first-principles electronic structure calculations under different stress conditions (see for example, Ref. [4]).

Within the above three families of compounds, silicon carbide (SiC), zinc oxide (ZnO), graphite and molybdenum disulfide (MoS_2) are pertinent examples because, besides their genuine bonding networks, they are materials with a variety of applications in several technological sectors as new semiconductor devices, field effect transistors [1,2,5–8], lubricants [9,10] and components of solar cell panels [3]. In the manufacturing processes of these materials, mechanical failure may occur as a result of the stresses induced during the heating cycles to which the compounds are subjected. In addition, the simultaneous existence of covalent and van der Waals interactions leads to preferential bi-dimensional and three-dimensional atomic arrangements in their crystalline structures that result in a high anisotropic response of these materials under variable stress conditions which is worth to be explored.

The challenge consists in the accurate calculation of the limiting tension that these materials can support in particular directions. Considering perfect non-defective crystals, this maximum tension is known as the ideal or critical strength (σ_c) of the material for that direction. Both, experimentally and theoretically, the evaluation of strain-stress curves constitutes the usual strategy to access to this quantity since after this critical point a catastrophic scenario emerges in form of a crystal fracture or a phase transition. It seems then required to understand how the atomic level interactions correlate with the mechanism of

failure in these environmental conditions and, if possible, anticipate the onset of the catastrophic scenario.

A number of theoretical studies using first-principles calculations, mainly employing density functional theory (*DFT*) [11,12], have permitted a quantitative evaluation of the critical strength of various materials (see [13–15] and references therein to cite a few) showing that the effect of multi-axial stress obviously depends on the atomic species involved [16–18]. However, to the best of our knowledge, none of these studies have addressed the description of the observed or calculated stress-strain data by means of analytical functions as normally happens for example in high-pressure and related fields. Such equations of state would open the possibility of anticipating critical values for the strength and strain of materials without reaching the instability condition. At this regard, it is pertinent to recall the spinodal equation of state (*SEOS*) [19]. This analytical function was designed to describe the high-pressure behavior of condensed matter using as a reference state the onset of the elastic instability. It has been successfully applied not only to the description of experimental and theoretical pressure-volume data, but also to the pressure evolution of one dimensional unit cell parameters [20]. Along with this fact, the SEOS is particularly well suited for the description of both experimental and theoretical stress-strain data derived from variable stress tensile conditions since, in the limit, these conditions precisely lead to the elastic instability of the material, i.e, the reference state for this analytical EOS.

In this chapter, we present results from *DFT* calculations performed to obtain the critical strength of 3C- and 2H-polytypes of SiC, ZnO zinc blende and wurtzite, graphite and 2H-MoS_2 along their main crystallographic directions without and with superimposed transverse stress conditions. Results are analyzed in terms of the density of chemical bonds and atomic interactions in the investigated directions of these materials. We are particularly interested in general analytical functions able to represent the behavior of different types of compounds under these tensile conditions and to reproduce the critical parameters. For this end, we propose a new *SEOS*-form that uses the critical strain as the reference state and that can be easily used to fit both, experimental and calculated stress-strain data.

The chapter is divided in three more sections. In the next one, we present computational details of the electronic structure calculations and the algebra related with the new *EOS*. Section 4.2 contains the results and the discussion and is divided in three

subsections devoted, respectively, to the equilibrium properties of the four compounds, the stress-strain calculated curves, and the energetic and Young moduli derived from the proposed *SEOS*. A summary of our main findings are given at the end of the chapter.

4.1. Computational Details

4.1.1. Electronic Structure Calculations

First-principles electronic energy calculations and geometry optimizations under the Kohn-Sham *DFT* framework of *3C* and *2H* polytype structures of *SiC*, ZnO, *ABA* stacking of graphite and hexagonal *2H-MoS_2* are carried out with the *ABINIT* code [21, 22] using the Perdew-Burke-Ernzerhof (*PBE*) exchange-correlation functional [23]. In order to take into account van der Waals forces, the correction (*DFT-D2*) to the exchange-correlation term, as proposed by Grimme [24], is used for graphite and MoS_2. Although this pairwise approach does not capture many-body effects inherent to van der Waals interactions (see for example [25–27]), it has been proven to be accurate enough to determine optimized geometries involving the length scale (Å) of the tensile phenomena explored in this thesis. The so-called *FHI* atomic plane wave pseudopotentials [28] are adopted, while cutoff energies and Monkhorst-Pack grids [29] are set to *1000 eV* and *6 x 6 x 6* and *6 x 6 x 4* for 3C-SiC and *2H*-SiC respectively; *1200 eV* and *6 x 6 x 3* for graphite; *400 eV* and *6 x 6 x 2* for *2H-MoS_2* and *400 eV* and *8 x 8 x 8*and *8 x 8 x 6* for cubic- and hexagonal-ZnO, respectively. Atomic positions are optimized until the total energy converged within *0.1 meV*. At the same time, all the strain components (except in the applied loading direction) were optimized so that the corresponding stress components turned out to be within *100 MPa* from a predetermined value. The Broyden-Fletcher-Goldfarb-Shanno minimization scheme (*BFGS*) [30] was used. In this way, tensile-strain curves under controlled normal stress were obtained. Critical strength (ideal strength) was determined as the maximum value of tensile stress before the lattice loses stability and the forces diverge. Multi-axial stress calculations have been performed superimposing a transverse stress to the chosen stress direction. Atomic positions and movements through the different paths are analyzed using the visualization program for structural models (*VESTA* code) [31].

For the cubic *structure*, we calculate how the stress increases along the [100], [110] and [111] symmetry directions. For the hexagonal *one*, an orthorhombic unit cell containing four atom pairs, calculations were performed along the normal-plane direction [001] perpendicular to the layers, and two in-plane directions, one containing nearest neighbors

(*NN*) [110], so-called zigzag direction and the other connecting next nearest neighbors (*NNN*) [$\bar{1}$10], so-called armchair direction.

The stress tensor is calculated in *ABINIT* as the derivative of the total energy with respect to the strain tensor. The strain tensor, $\varepsilon_{\alpha\beta}$, can be calculated from the relation between the strain-free lattice vector of a given atom μ, r_μ , and its strained lattice vector, r'_μ, as follows [32]:

$$r'^{\alpha}_{\mu} = r^{\alpha}_{\mu} + \sum_{\beta=1}^{3} \varepsilon_{\alpha\beta}\, r^{\beta}_{\mu} \qquad (1)$$

where μ and β symbols denote the Cartesian components.

In the calculation of the second-order elastic constants in these cubic and hexagonal lattices, we follow an energy-strain scheme (see Refs. [33, 34]). The lattice was first relaxed to achieve a zero stress state and then strains were applied by multiplying the lattice vectors by the strain matrix. For a lattice initially under no stress, and using Voigt notation, the energy of the strained lattice can be expressed around the equilibrium position as:

$$E = E_0 + \frac{V_0}{2} \sum_{ij} C_{ij} \varepsilon_i\, \varepsilon_j \qquad (2)$$

where E_0 and V_0 are, respectively, the energy and the volume of the unstrained lattice. There are three independent elastic constants for the cubic lattice (C_{11}, C_{12}, C_{44}) and five independent elastic constants (C_{11}, C_{12}, C_{33}, C_{13}, C_{44}) for the hexagonal one, thus three and five sets of finite strains were applied respectively. For each case, eleven equally-spaced strain values were applied between *-0.05* and *0.05*. The elastic constants were obtained from fitting a quadratic equation to the energy-strain calculated data points. The bulk modulus B_0 for each structure was calculated using its relationship with the elastic constants. A detailed description of elastic constants and their calculation are given in Chapter 3.

4.1.2. Spinodal-like stress-strain equation of state

From a thermodynamic point of view, the elastic stability limit of a solid at thermal conditions is defined by the point where the second derivative of the internal energy with respect to the volume becomes zero. At the corresponding pressure, also named as the spinodal pressure (p_{sp}), the bulk modulus (B) of the substance tends to zero, and therefore any

restoring force given by the chemical bonds is overcome, leading to a crystal rupture or a phase transition [35].

The spinodal locus has been considered as an excellent reference to describe the thermodynamic behavior of solids under high pressure conditions [36,37]. Polymers, metals, covalent and ionic crystals have been analyzed showing that their (*p-V)* data is accurately and universally represented through the spinodal constrain. This follows from the fact that along a given isotherm, the isothermal bulk modulus depends on the pressure through the following universal relation [38, 39]:

$$B = B^{*}\left(\sigma_{sp} - \sigma\right)^{\gamma} \tag{3}$$

Where B^{*} and β are, respectively, the amplitude and the pseudocritical exponent that characterize the pressure behavior of the isothermal bulk modulus.

The spinodal equation of state has not been used only in its volumetric form. For instance, Francisco et al.[40] studied the evolution under isotropic compression of the lattice parameters of rutile TiO_2, showing that a one dimensional (*1D*) spinodal equation of state (*1D-SEOS*) can reproduce accurately their pressure dependence. To that, the authors define a linear bulk modulus, or equivalently a directional Young modulus (Y_l, l specifies the direction), and applied the universal relation of Eq.[3]. Considering both the physical significance and the directional behavior of this spinodal-like equation of state, in this thesis we introduce a *1D-SEOS* to analytically describe the stress-strain curves associated with tensile stress phenomena. Indeed, under directional stretching, the critical strength attained along the stress-strain curve corresponds to the spinodal stress limit, σ_{sp}. The later parameter accounts for the maximum engineering stress at which the solid breaks, and therefore, represents the elastic limit of the material. Furthermore, at this spinodal point the directional Young modulus Y_l has a value of zero, pointing out that there is no material resistance to a phase transition or rupture. Notice that these two parameters (σ_{sp} and Y_l) are also the one-dimensional analogs of the spinodal pressure and the bulk modulus. Consequently, from this perspective, the spinodal constrain is clearly fulfilled. Accordingly, the stress dependence of Y_l can be accurately described with an amplitude factor $Y_l^{*}$and a pseudocritical exponent γ following an equivalent power law form as Eq.[3]., and taking into account the engineering convention of signs (σ is positive for tensile and negative for compressive stress):

$$Y_l = Y_l^*(\sigma_{sp} - \sigma)^{\gamma} \quad (4)$$

Under these premises, an analytical stress-strain *EOS* can be derived. As the Young modulus is thermodynamically defined as the derivative of the stress with respect to the strain, the simple integration of Eq.[4] leads to the following expression for a directional tensile curve:

$$\sigma = \sigma_{sp} - \{Y_l^*(1-\gamma)(\sigma_{sp} - \sigma)(\epsilon_{sp} - \epsilon)\}^{1/(1-\gamma)} \quad (5)$$

Eq.[5] provides an analytical relationship between the stress and the strain along a particular direction of a crystalline solid involving four characteristic parameters. However, it must be emphasized that only three are independent since the spinodal strength, the spinodal strain and the amplitude factor are related realizing that no strain is present at σ = 0:

$$Y_l^*(1-\gamma) = \frac{\sigma_{sp}^{(1-\gamma)}}{\epsilon_{sp}} \quad (6)$$

Using this expression in Eq. [5], we arrive at our final stress-strain *1D-SEOS*:

$$\sigma = \sigma_{sp}\left(1 - \left(\frac{\epsilon_{sp} - \epsilon}{\epsilon_{sp}}\right)^{1/(1-\gamma)}\right) \quad (7)$$

An interesting feature of the proposed stress-strain *SEOS* is that it can be also expressed analytically in its energy form. In fact, considering the isotherm at 0 *K* and neglecting zero point vibrational contributions, the stress is related to the internal energy *E* and the zero-pressure volume V_0 by means of [40]:

$$\sigma = \frac{1}{V_0}\frac{dE}{d\epsilon} \quad (8)$$

Consequently, the integrated energy-strain *SEOS* is:

$$E_{sp} - E = V_0\,\sigma_{sp}(\epsilon_{sp} - \epsilon) - V_0\frac{(1-\gamma)}{(2-\gamma)}\frac{\sigma_{sp}^{1/(1-\gamma)}}{\epsilon_{sp}}(\epsilon_{sp} - \epsilon)^{\frac{2-\gamma}{1-\gamma}} \quad (9)$$

where E_{sp} is the internal energy of the solid at the spinodal strain, or equivalently the spinodalenergy. This quantity must be understood as the energy needed to separate the

crystallographic planes perpendicular to the stress-strain direction, and therefore to overcome the interatomic forces. Mo

reover, the spinodal energy can be expressed in terms of the spinodal stress and spinodal strain once we set to zero the internal energy at zero strain:

$$E_{sp} = V_0 \left(\epsilon_{sp}\sigma_{sp} - \frac{(1-\gamma)}{(2-\gamma)} \left(\frac{\sigma_{sp}}{\epsilon_{sp}} \right)^{\frac{1}{1-\gamma}} \right) \tag{10}$$

An important feature of our current spinodal stress-strain ***EOS*** is that the spinodal energy give us the opportunity to connect the mechanical parameters along a given tensile direction with the cohesive interatomic interactions.

Some words of caution on the notation should be given. First, σ_c and σ_{sp} both represent the critical or ideal strength of the material along a given direction. The first symbol is obtained from (σ_i, ϵ_i) calculated or experimental data, whereas the second one comes from our *1D-SEOS* fittings as we discuss later. The same applies to ϵ_c and ϵ_{sp}. Second, in our static simulations (zero temperature and zero point energy contributions neglected), the internal energy of the system E is reduced to the electronic energy obtained in our *DFT* calculations. Finally, this symbol E is often used in other works to design the Young modulus. To avoid confusion, here we have chosen Y_l for the directional Young modulus.

4.1.3. Spinodal Equation of State Fittings

The versatility of the proposed *1D-SEOS* allows us fitting Young modulus-stress (Eq.[4]), stress-strain (Eq.[7]), and energy-strain (Eq.[10]) data. Since the spinodal hypothesis is based on the assumption that the universal relationship given in expression Eq.[3] can accurately describe stress-dependence of the directional Young modulus, it becomes first necessary to examine if the proposed power law can fit in a reliable manner the calculated data. To minimize numerical errors induced by the second strain derivative of the energy involved in the $Y_l - \sigma$ curves, a linear interpolation of the computed electronic energy has been performed. In all the cases, adjusted *R*-squares for the $Y_l - \sigma$ curves lie in the range between *0.97* and *0.99* and residuals are equally distributed between negative and positive values with a percentage of deviation lower than *7%*. In order to test the reliability of our proposed *1D-SEOS*, the pseudocritical exponent and the critical strength and critical strain have been used as fitting parameters to analytically construct the stress-strain curves and

energy-strain curves for all the directions and materials studied in this thesis according to the expressions derived in subsection 4.1.2. Successfully, we obtain that the differences between the analytical curves and the calculated data are always below *1%*. A summary of the fitting parameters are presented in Table 4.1. Notice that Eq.[6] and Eq.[10] can provide us the values of $Y_l^*(0)$and γ.

As we can see in Table 4.1, γ parameter lies inside the 0.41 ± 0.12 interval, depending on the crystal and the direction considered (except for ZnO with few values up to 0.69). These γ values are much lower than the universal β value of *0.85* assumed by Baonza et al. for the volumetric compression of solids [35]. Such a difference is attributed to the fact that here we are in the stretching region. Indeed, Brosh et al. [41] studied the dependence of the pseudocritical exponent as a function of the reduced volume both in the compressive and expansive regimens. These authors conclude that while the universal pseudocritical exponent of 0.85 accurately describes the solid under high and moderate pressure, the exponent goes down to the value of *0.5* in the case of the negative pressure regime, which is within the range of the results obtained in our spinodal stress-strain equation of state.

Table 4.1 *1D-SEOS* parameters from the fittings to our computed stress-strain data. Units of σ_{sp} and $Y_l^*(0)$ are GPa.

Material	Direction	γ	ϵ_{sp}	σ_{sp}
3C-SiC	[100]	0.29	0.35	90.5
	[110]	0.49	0.30	52.3
	[111]	0.36	0.15	45.1
2H-SiC	[001]	0.36	0.15	44.9
	[110]	0.46	0.29	58.0
	[$\bar{1}$10]	0.34	0.17	50.7
Graphite	[001]	0.35	0.99	0.06
	[110]	0.53	0.26	85.8
	[$\bar{1}$10]	0.37	0.11	78.3
2H-MoS2	[001]	0.39	0.05	0.07
	[110]	0.38	0.27	21.4
	[$\bar{1}$10]	0.46	0.20	14.2
B1-ZnO	[100]	0.63	0.20	7.98
	[110]	0.63	0.23	14.31
	[111]	0.29	0.35	57.60
B2-ZnO	[100]	0.62	0.36	52.46
	[110]	0.69	0.16	19.08
	[111]	-	-	-
B3-ZnO	[100]	-	-	-
	[110]	0.49	0.22	12.98
	[111]	0.45	0.25	30.00
B4-ZnO	[100]	-	-	-
	[110]	-	-	-
	[$\bar{1}$10]	0.32	0.20	16.00

4.2. Covalent Materials: Silicon Carbide (*SiC)*: Results and Discussion

4.2.1. Bulk Properties

This subsection is restricted just to the summary of the equilibrium structural and elastic data of the two SiC polytypes. Computed lattice constants, bulk moduli and elastic constants are collected in Table 4.2 along with experimental and other calculated values. Overall, our results are found to be in good agreement with reported observed data, showing only slight differences due to the overestimation of the lattice constants and underestimation of the elastic constants inherent to the *GGA* level of calculations.

Table 4.2 Zero pressure lattice and elastic constants of *3C-* and *2H-SiC* polytypes. All B_0 values calculated using Voigt elastic constants relationship.

		This work	Calculated	Experimental
3C-SiC	a(Å)	4.39	4.34 [42], 4.38 [43]	4.34 [44]
	C_{11}(GPa)	341	390 [42], 385 [43]	352 [45]
	C_{12}(GPa)	130	134 [42], 128 [43]	140 [45]
	C_{44}(GPa)	224	253 [42], 264 [43]	233 [45]
	B_0(GPa)	200	219, 213	211
2H-SiC	a(Å)	3.085	3.05 [46], 3.09 [43]	3.076[47]
	c(Å)	5.060	5.00 [46], 5.07 [43]	5.224 [47]
	C_{11}(GPa)	528	541 [46], 536 [43]	501 ± 4[48]
	C_{12}(GPa)	112	117 [46], 78 [43]	111 ± 5 [48]
	C_{33}(GPa)	565	586 [46], 573 [43]	553 ± 4 [48]
	C_{13}(GPa)	52	61 [46], 31 [43]	52 ± 9 [48]
	C_{44}(GPa)	156	162 [46], 164 [43]	163 ± 4 [48]
	B_0(GPa)	228	238, 214	220

4.2.2. Ideal strength with and without transverse stress.

This subsection is devoted to the calculation of the strain-stress curves of the two structures considered in this part. First, we collect in Fig.[4.1] the results under vanishing transverse stress. For *3C-SiC* and *2H-SiC*, calculated points are very similar to those reported by Umeno, Kubo and Nagao [43].

It is usual to recall to the chemical bonding network to interpret at an atomic level differences in the strain-stress curves between compounds and/or directions. Without being strictly quantitative while keeping the basic chemical meaning, a simple and practical indicator able to account for the majority of these differences is proposed as follows. Each chemical bond in the unit cell is described by a vector connecting its two bound nearest-neighbor atoms. The projection of this vector along the corresponding tensile direction is evaluated and the sum calculated over all the bonds in the unit cell is defined as the total effective bond length (*EBL*) associated to that direction. The two main structural effects induced in the chemical bonds by the tensile strain (changes in bonding lengths and angles) are essentially captured in this parameter. *EBL* values exhibit the expected trend always increasing as the strain increases up to the stability limit.

Fig.[4.1-a] shows that in *3C-SiC* the slopes in the low strain region are nearly equal regardless the direction. However, the maximum stress value strongly depends on the direction of the deformation with an ideal strength nearly twice larger along the [100] axis (ϵ_c= 0.35 andσ_c = 91 GPa) as that found for [110] (ϵ_c = 0.30 and σ_c =53 GPa) and [111] (ϵ_c = 0.15 and σ_c = 45 GPa). We notice that along [100] all tensile forces are equally distributed over the Si-C bonds. This is in contrast to the tension along [110] and [111] directions. For example, in the latter, one of the four C-nearest neighbors of a given Si- atoms stand along the same [111] direction and the corresponding Si-C bond suffers a pure stretching, whereas the stretching of the other three Si-C bonds is not so effective and involves bond angle modifications upon the tensile strain along this [111] direction (Table 4.3). At zero strain, the previously defined *EBL* parameter already has a value roughly twice greater for the [100] direction (17.5 Å) than for the [110] (9.3 Å) and [111] (9.5 Å) directions (Table 4.3). Thus, although the order between the [100] and [111] directions is not captured considering just the equilibrium structure, the *EBL* parameter catches the essential difference between the [100] direction and these two other directions.

The stress-strain curves during uniaxial tension with vanishing transverse stress in *2H-SiC* are shown in Fig.[4.1-b]. Slopes in the low strain (harmonic) region are almost exactly equal whereas the maximum stress value strongly depends on the direction of the deformation. The stress-strain relation in *2H-SiC* [001] (ϵ_c= 0.15 and σ_c= 45 GPa) and 3C-SiC [111] are nearly identical. It is so because of the similarity of the lattice planes normal to the stress direction, and so are the curves of *2H-SiC* [100] (ϵ_c= 0.29 and σ_c= 58 GPa) and *3C-SiC* [110]. The stress-strain relation in *2H-SiC* along [110] shows intermediate values (ϵ_c= 0.20 and σ_c= 50 GPa). Again, these values correlate with the effective Si-C bond lengths along the corresponding directions. Calculated *EBL* values in Å for the [110], [$1\bar{1}0$] and [001] are, respectively, 21.3, 16.8, and 12.3 (Table 4.3), following the same trend as σ_c and in agreement also with previous interpretations in terms of next-nearest *Si-C* interactions by Umeno et al. [43].

For all directions and structures, we now analyze new results coming from the proposed analytical *1D-SEOS*. All the curves in the two panels of Fig [4.1] were obtained from the *1D-SEOS* fittings to the calculated strain-stress data. The performance of the *1D-SEOS* is apparent and allows us to derive with confidence critical stress and critical strain values from the corresponding fitting parameters σ_{sp} and ϵ_{sp}, respectively. We have checked that the trends and specific values of these two key parameters compare with high accuracy with our first-principles computed numerical values (see Table 4.1). Thus, we arrive to this interesting conclusion: the *1D-SEOS* of Eq.[7] is an appropriate analytical function for describing stress-strain data.

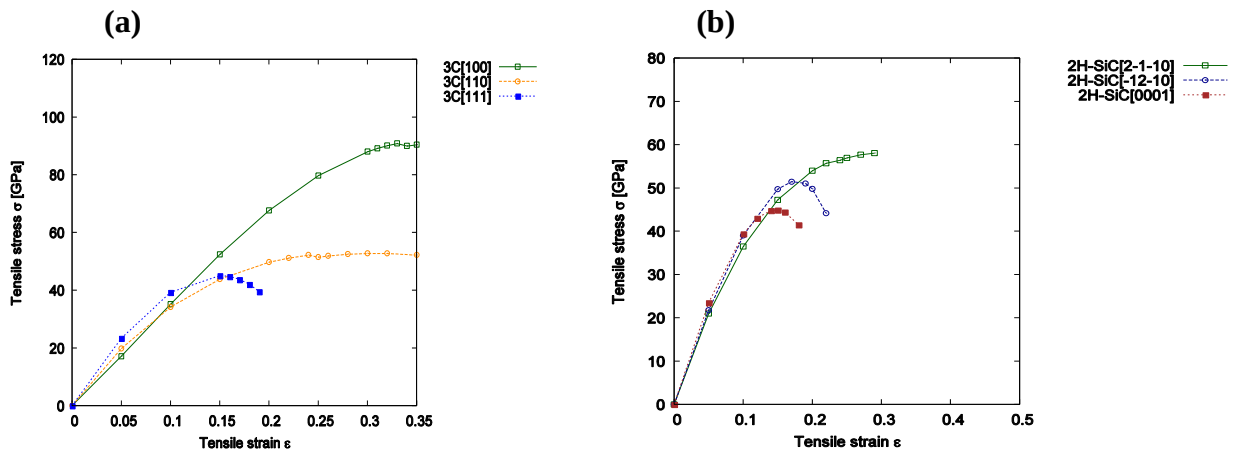

Figure 4.1 Calculated strain-stress curves without transverse stress for: (**a**) *3C-SiC*, (**b**) *2H-SiC*.

Table 4.3 Effective Bond Length (*EBL*) vs strain at zero-transverse stress in SiC-polymorphs

ε	0,00	0,05	0,10	0,15	0,20	0,25	0,30	0,33	0,35
[100] (Si-C) [Å] σ [GPa]	17,4811 -0.0006	18,3550 17.1351	19,2291 35.1621	20,1032 52.4546	20,9772 67.6626	21,8512 79.7698	22,7253 88.0570	23,2497 90.9083	22,5497 90.4528
[110] (Si-C) [Å] σ [GPa]	9,2685 0.0068	9,7317 19.8038	10,1954 34.1828	10,6588 43.8803	11,1223 49.7450	11,4920 51.5011	11,2418 52.8216	-	-
[111] (Si-C) [Å] σ [GPa]	9,4839 0.0025	9,9581 23.3517	10,4323 39.2249	10,9065 45.0364	-	-	-	-	-
[2$\acute{1}\acute{1}$0] (Si-C) [Å] σ [GPa]	21,3395 0.0020	22,4065 23.4965	23,4734 39.4081	24,5404 44.89345	25,6074 34.9075	-	-	-	-
[$\acute{1}$2$\acute{1}$0] (Si-C) [Å] σ [GPa]	16,8788 0.0033	17,7227 21.7812	18,5668 39.0343	19,4106 49.7105	19,6074 49.7913	-	-	-	-
[0001] (Si-C) [Å] σ [GPa]	12,3410 0.0021	12,9581 23.4965	13,5751 39.4081	14,1922 44.8935	13,5051 34.9075	-	-	-	-

We have noticed earlier that multi-load conditions may be present in manufacturing processes combining thermal effects and epitaxial growth. As a particular situation of these conditions, we have studied in a second round of simulations the effects of superimposing transverse stress (both compressive and tensile) on the previous tensile directions for the two structures. The expected trend is a decreasing of the critical strength as we increase the superimposed transverse stress from negative to positive values. In fact, this is the computed behavior for the majority of situations we have studied. For example, the critical strength σ_c is lowered by the transverse stress σ_t in all the directions in *3C-SiC* (except [110]), 2H-SiC (except [100]). All these results are displayed in Fig [4.2] and are in complete agreement with the computed data in *3C-* and *2H-SiC* reported by Umeno et al. [43]. In general, the unexpected positive slope in the ideal strength-transverse stress curve appears at compressive

transverse stress values. In the tensile regime, all the directions and structures show a modulated lowering of the ideal strength as the transverse tension increases which is compatible with the overall weakening of the compounds as multi-load conditions are enhanced or, in Umeno et al. words, to the higher strain energy stored in the material.

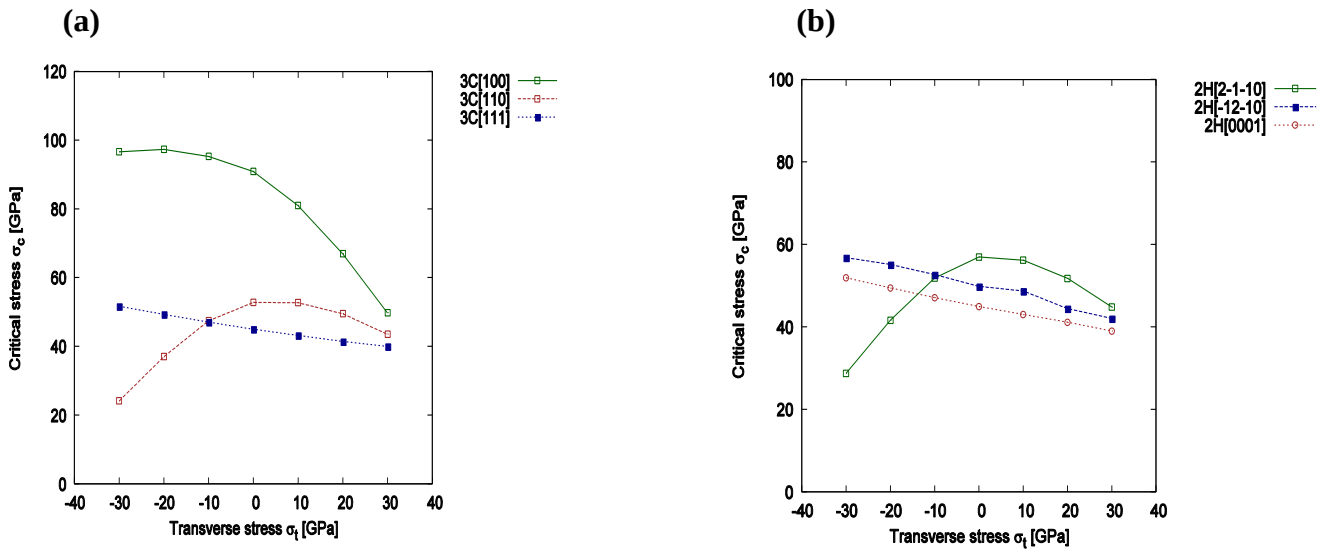

Figure 4.2 Calculated critical stress-transverse stress curves for: (**a**) *3C-SiC*, (**b**) *2H-SiC*.

Interestingly enough, we have observed an equivalent behavior when we analyze the computed *EBL* parameters. In all but the cases where we have detected an exception, the calculated effective bond length parameter at the critical strain condition decreases monotonically as we superimpose the transverse stress on the corresponding tensile strain direction. Thus, we found that the decreasing of the ideal strength value correlates with the decreasing in the *EBL* parameter (Table 4.4). For example, along the [111] direction in 3C-SiC, *EBL* continuously decreases from 11.00 Å at σ_t = -30 GPa to 10.78 Å at σ_t= +30 GPa. The corresponding values at the same transverse stress conditions for the [100] direction are 24.71 Å and 21.18 Å. Similar trends are found for the *EBL* parameter along the [$1\bar{1}0$] and [001] directions in *2H-SiC* (Table 4.4). On the contrary, in those cases where negative transverse stresses induce an unexpected behavior, this *EBL* parameter also shows an increasing as the transverse stress increases up to the condition of vanishing transverse stress. Thus, along [110] in *3C-SiC* and [100] in *2H-SiC*, the values of *EBL* at σ_t = -30 GPa are,

respectively, 10.94 Å and 26.08 Å, increasing up to 11.49 Å and 26.24 Å at σ_t = 0 GPa, and finally decreasing to 10.97 Å and 24.13 Å at σ_t = +30 GPa. The reason why a reduction in the critical strength occurs as compressive transverse is superimposed has been explained by the appearance of a thermodynamic competitive phase as the rock-salt structure in *3C-SiC* [43]. Here, we also see that this reduction in the σ_c also correlates with the fact that the effective *Si-C* bond lengths along the [110] and [100] directions in *3C-SiC* and *2H-SiC*, respectively, show lower values at the critical conditions when the compressed transverse stress is increased, thus correlating with the trend followed by the critical strength.

Table 4.4 Nearest neighbor (*NN*) distance at critical stress σ_c and strain ϵ_c with transverse stress σ_t in SiC-polymorphs.

transverse stress σ_t[GPa]	-30	-20	-10	00	10	20	30
[100] (Si-C) [Å]	1.96272	2.01172	2.06202	2.10596	2.14464	2.17361	2.16158
ϵ_c	0.15	0.20	0.30	0.33	0.35	0.30	0.25
σ_c[GPa]	96.62	97.30	95.28	90.91	88.99	66.95	49.79
EBL [Å]	24,7133	23,4034	23,3384	23,2494	23,1959	22,6794	21,1812
[110] (Si-C) [Å]	1.95934	2.02010	2.09804	2.13927	2.26173	2.23878	2.20402
ϵ_c	0.15	0.20	0.25	0.24	0.30	0.25	0.20
σ_c[GPa]	24.15	36.99	47.43	52.82	52.75	49.51	43.51
EBL [Å]	10,9445	11,2954	11,3335	11,4920	11,2153	11,1741	10,7919
[111] (Si-C) [Å]	1.81346	1.83253	1.84472	2.15407	2.68545	2.17677	2.15407
ϵ_c	0.15	0.20	0.15	0.15	0.15	0.15	0.17
σ_c[GPa]	51.67	49.30	47.08	45.04	43.20	41.43	39.94
EBL [Å]	11,0044	10,9737	10,9414	10,9065	10,8707	10,8294	10,7812
[$2\acute{1}\acute{1}0$] (Si-C) [Å]	-	-	2.08796	2.19351	2.12411	-	-
ϵ_c	0.10	0.15	0.25	0.29	0.20	0.22	0.20
σ_c[GPa]	28.71	41.61	56.16	58.04	52.85	51.74	44.76
EBL [Å]	26,0794	26,1141	26,1507	26,2433	25,4628	25,3520	24,1372
[$\acute{1}2\acute{1}0$] (Si-C) [Å]	-	-	1.89577	1.93193	1.93692	-	-
ϵ_c	0.20	0.20	0.20	0.20	0.15	0.20	0.20
σ_c[GPa]	56.79	55.09	52.63	49.79	48.69	44.41	42.02
EBL [Å]	19,97,76	19,8789	19,6131	19,6074	17,7492	16,1153	16,0356
[0001] (Si-C) [Å]	-	-	1.89549	2.24228	1.92884	-	-
ϵ_c	0.15	0.15	0.15	0.15	0.15	0.15	0.15
σ_c[GPa]	51.89	49.40	47.05	44.89	42.94	41.10	38.96
EBL [Å]	14,4979	14,3639	14,2584	14,1922	14,0992	14,0403	13,9958

4.2.3. Other outcomes of the stress-strain SEOS: energetic and directional Young moduli

As stated in subsection 4.1.3, our analytical scheme allows us not only gathering information on the critical parameters, but also on the energetic of crystalline materials and on the Young moduli along specific tensile directions. From an experimental point of view,

stress-strain data can be directly measured for particular directions whereas the corresponding energy-strain curves remain only accessible once an equation of state is proposed. Eq.[10] displays how, by simple integration of our stress-strain *1D-SEOS*, analytical energy-strain curves can be derived using data either from experiments or from computer simulations. In the previous subsection, we have shown that our calculated (ϵ_i,σ_i) data points are well described by the proposed *1D-SEOS*. Here, the integrated *SEOS* for all the directions of materials studied in this part are represented in Fig [4.3]. The symbols correspond to the energy minima at selected strains obtained from our first-principles calculations. The calculated parameters associated with the integrated forms are collected in Table 4.5.

The analytical energy curves clearly reflect the good quality of the fittings (see Fig 4.3). Two parameters define the shape of each of these curves, ϵ_{sp} and E_{sp}. The first one, previously discussed in relation to the stress-strain curves (see Table 4.1), identifies the abscissa of the inflexion point, where the directional Young modulus vanishes. The ordinate of this point is E_{sp} (see Table 4.5) and correlates quite well with the critical/spinodal strength calculated along each of the directions explored for the materials under study in this part. The higher the strength, the higher the energy required to induce an elastic instability in the material.

As regards the directional Young modulus, we can easily derive a simple expression at zero stress $Y_l(0)$involving the three parameters of the stress-strain *1D-SEOS* by evaluating Eq. [4] at zero stress:

$$Y_l(0) = \frac{\sigma_{sp}}{\sigma_{sp}(1-\gamma)}. \qquad (11)$$

This parameter is discussed below.

Table 4.5 Energy and Young modulus parameters from the integrated stress-strain *SEOS* fittings

Material Direction	$Y_l(0)$(GPa)	E_{sp} (kJ/mol)
3C-SiC [100]	396	219
[110]	407	110
[111]	478	50
2H-SiC [001]	481	50
[110]	437	142
[$\bar{1}$10]	450	66

In *3C-SiC*, the directional Young moduli at zero stress are (in GPa) 396, 407, 478 GPa for the [100], [110] and [111] directions, respectively. These results are in concordance with the directional Young moduli calculated through the theory of representation surfaces [49]. For instance, in the case of the [111] direction

$$Y_{111} = \left(S_{11} - \frac{2}{3}\left(S_{11} - S_{12} - \frac{1}{2}S_{44}\right)\right)^{-1} \qquad (12)$$

where S_{11}, S_{12}, and S_{44} are the compliance constants related to the elastic constants by:

$$S_{11} = \frac{C_{11}+C_{12}}{(C_{11}-C_{12})(C_{11}+2C_{12})}, \quad S_{12} = \frac{-C_{12}}{(C_{11}-C_{12})(C_{11}+2C_{12})}, \quad S_{44} = \frac{1}{C_{44}}. \qquad (13)$$

According to the data from Table 4.2, and using the above equations, the calculated value for Y_{111} (0) is 489 GPa in good agreement with the parameter obtained from our *1D-SEOS*.

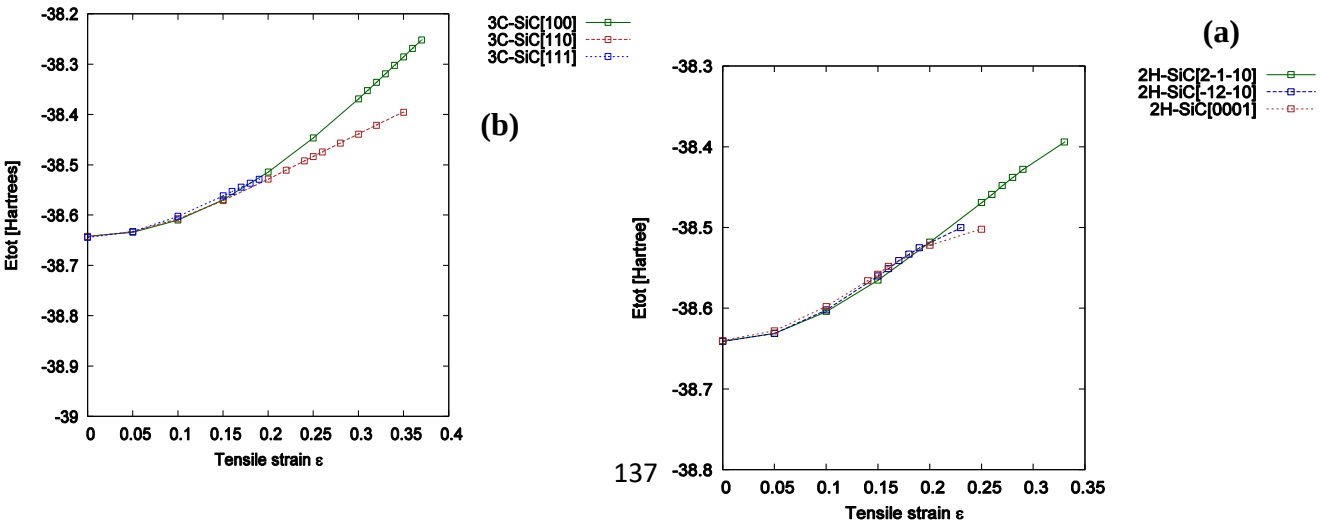

Figure 4.3 Calculated energy-strain curves for: (**a**) 3C-SiC, (**b**) 2H-SiC.

In this case, the elastic behavior of the cubic SiC polytype is not enterely isotropic and $Y_l(0)$ slightly increases along the sequence [100] [110] and [111]. Y_l (0) provides a quantitative measure of the initial slope of the stress-strain curve, thus representing the resistance of the material to a tensile distortion along a particular direction at equilibrium. Under this perspective, the values of $Y_l(0)$ in the [100], [110] and [111] series of *3C-SiC* inform that the direction [111] offers the highest resistance to a strain stretching at zero stress. In *2H-SiC*, the values of $Y_l(0)$ point out that all the directions studied present similar resistance to distortion. Here, the solid behaves less anisotropically than in the case of the cubic polytype, expanding a narrower range of values, although both polytypes display similar zero stress Young moduli.

4.3. IonicMaterials (Zinc Oxide *ZnO)*: Results and Discussion

4.3.1. Bulk Properties

This subsection is restricted just to the summary of the equilibrium structural and elastic data of the four *ZnO* phases studied in this Thesis. Computed lattice constants, bulk moduli and elastic constants are collected in Table 4.6. Overall, our results are found to be in good agreement with reported observed data, along with experimental and other calculated values [50,51], showing only slight differences due to the overestimation of the lattice constants and underestimation of the elastic constants inherent to the *GGA* level of calculation.

Table 4.6 Zero pressure lattice and elastic constants of *ZnO*-polytypes. All B_0 values calculated using Voigt elastic constants relationship.

		This work	Calculated	Experimental
B1-ZnO	a(Å)	4.37	4.63[50],4.53[52]	4.47[53]
	C_{11}(GPa)	224.20	237.32[51], 226.90[50]	-
	C_{12}(GPa)	129.60	145.18[51],139.85[50]	-
	C_{44}(GPa)	74.10	59.04[53], 82.19[51]	-
	B_0(GPa)	161.13	164.91[51], 209.6[54]	202.50[55]
B2-ZnO	a(Å)	2.71	2.69[51], 3.29[54], 2.67[56]	-
	C_{11}(GPa)	363.70	433.47[51]	-
	C_{12}(GPa)	49.50	35.96[51]	-
	C_{44}(GPa)	37.00	69.04[51]	-
	B_0(GPa)	154.23	159.91[51], 205.4[54]	-
B3-ZnO	a(Å)	4.67	4.63[51],4.52[54]	4.62[57]
	C_{11}(GPa)	110.70	167.36 [51],155.93[50]	-
	C_{12}(GPa)	127.50	125.30 [51],116.33[50]	-
	C_{44}(GPa)	132.20	112.88 [51],128.13[38]	-
	B_0(GPa)	121.93	139.32 [1],157.28[56]	-
B4-ZnO	a(Å)	3.32	3.28 [51],3.21[54]	3.25 [55]
	c(Å)	5.34	5.32[51],5.16[34]	5.20[59]
	C_{11}(GPa)	222.10	226[60],227.00[58]	209.70[61]
	C_{12}(GPa)	90.40	87.00[62],108.34[50]	102.00[63]
	C_{33}(GPa)	238.30	246.00[64], 225.00[65]	211.00[66]
	C_{13}(GPa)	58.00	60.95[51],93.00[58]	90.00[67]
	C_{44}(GPa)	54.70	57.49[61], 49.89[51]	44.50[68]
	B_0(GPa)	125.60	129.19[51],164.36[56]	142.6[55]

4.3.2. Ideal strength with and without transverse stress.

This subsection is devoted to the calculation of the strain-stress curves of the four ZnO structures considered in this study. First, we collect in Fig 4.4 the results under vanishing transverse stress. For *B4-ZnO*, calculated points are very similar to those reported by Li-Zhi Xu, Yue-Lin Liu and Hong-Bo Zhou [69].

Fig 4.4-a shows that in *B1-ZnO* the slopes in the whole strain region are different for all directions. However, the maximum stress value strongly depends on the direction of the deformation with an ideal strength nearly four times larger along the [111] axis (ϵ_c = 0.35 andσ_c = 57.70 GPa) as that found for [110] (ϵ_c = 0.23 and σ_c = 14.34 GPa) and six times along the [100] (ϵ_c = 0.20 and σ_c = 8.06 GPa). We notice that along [111] all tensile forces are equally distributed over the Zn-O bonds. This is in contrast to the tension along [110] and [100] directions. For example, in the latter, one of the four O nearest neighbors of a given Zn atoms stand along the same [100] direction and the corresponding *Zn-O* bond suffers a pure stretching, whereas the stretching of the other three *Zn-O* bonds is not so effective and involves bond angle modifications upon the tensile strain along this [100] direction.

Fig 4.4-c shows that in *B3-ZnO* the slopes in the whole strain region are different for all directions. However, the maximum stress value strongly depends on the direction of the deformation with an ideal strength nearly twice larger along the [100] axis (ϵ_c= 0.58 and σ_c = 55.56 GPa) as that found for [111] (ϵ_c = 0.25 and σ_c =29.74 GPa) and four times as that found for [110] (ϵ_c = 0.22 and σ_c = 12.91 GPa). We notice that along [100] all tensile forces are equally distributed over the Zn-O bonds. This is in contrast to the tension along [110] and [111] directions.

The stress-strain curves during uniaxial tension with vanishing transverse stress in *B4-ZnO* are shown in Fig 4.4-d. Slopes in the low strain (harmonic) region are not equal whereas the maximum stress value strongly depends on the direction of the deformation. The stress-strain relation in *B4-ZnO* [001] (ϵ_c = 0.15 and σ_c = 20.42 GPa) and *B2-ZnO* [110] are nearly identical. It is so because of the similarity of the lattice planes normal to the stress direction (ϵ_c = 0. 15 and σ_c = 19.07 GPa). The stress-strain relation in *B4-ZnO* along [$\bar{1}$10] shows intermediate values (ϵ_c = 0.20 and σ_c = 15. GPa).

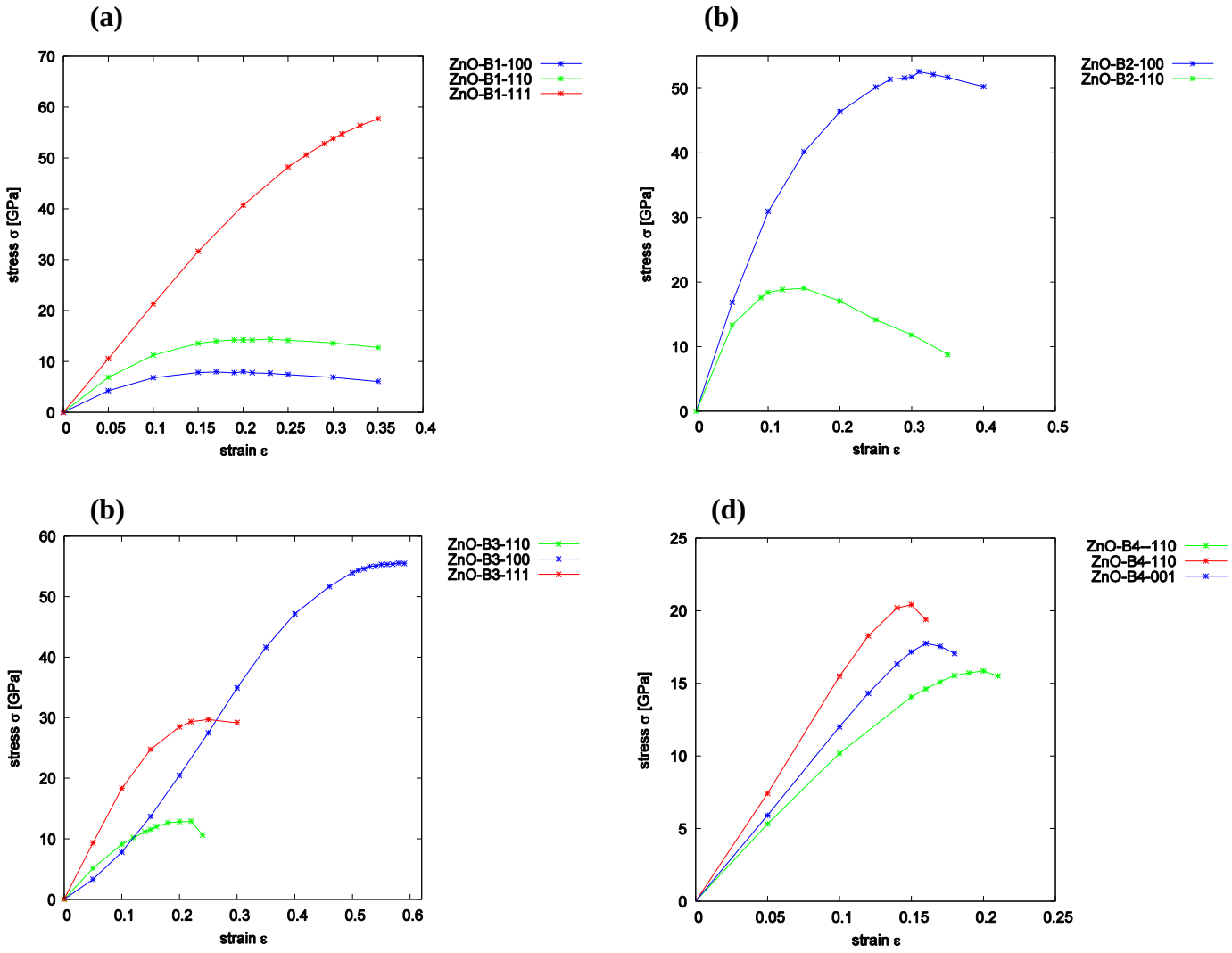

Figure 4.4 Calculated strain-stress curves without transverse stress for: (**a**) *B1-ZnO*, (**b**) *B2-ZnO*, (**c**) *B3-ZnO* and (**d**) *B4-ZnO*.

We have noticed earlier that multi-load conditions may be present in manufacturing processes combining thermal effects and epitaxial growth. As a particular situation of these conditions, we have studied in a second round of simulations the effects of superimposing transverse stress (both compressive and tensile) on the previous tensile directions for the four structures. The expected trend is a decreasing of the critical strength as we increase the superimposed transverse stress from negative to positive values. However, this is not the computed behavior for the majority of situations we have studied. For example, we can see in Fig 4.5 that the critical strength σ_c is only lowered by the (positive) transverse stress σ_t in the [111] direction in *B1-ZnO*, is increased by σ_t for compression and tension in B3-*ZnO* and B4-*ZnO* (except when the [001] direction is considered) and shows the expected decreasing trend in the two directions examined in the B2-phase. In general, the unexpected positive slope in

the ideal strength-transverse stress curve appears in this ionic compound regardless if the compressive transverse stress has positive or negative values. A more detailed exploration of the bonding network is needed to explain this variety of results that should be understood as a consequence of the directionality of the nearest neighbor ionic bonds and their organization in the corresponding structures. Obviously, the overall weakening of the compounds as multi-load conditions are enhanced, *i.e.* the higher strain energy stored in the material, is always a general principle that is preserved in this compound.

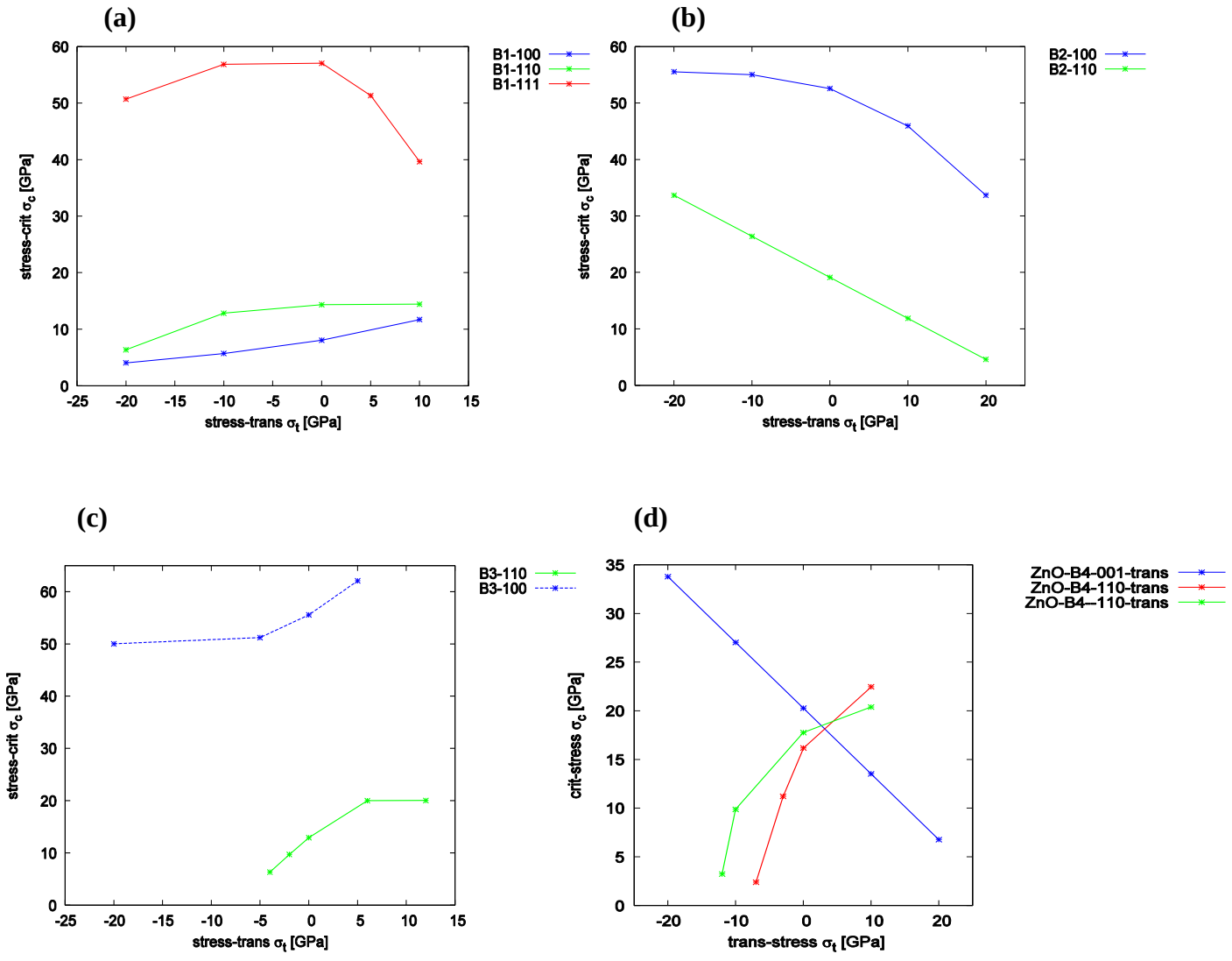

Figure 4.5 Calculated critical stress-transverse stress curves for: (**a**) *B1-ZnO*, (**b**) *B2-ZnO*, (**c**) *B3-ZnO*, and (**d**) *B4-ZnO*.

.

4.3.3. Other outcomes of the stress-strain SEOS: energetic and directional Young moduli

As stated in subsection 4.1.3, our analytical scheme allows us not only gathering information on the critical parameters, but also on the energetic of crystalline materials and on the Young moduli along specific tensile directions. From an experimental point of view, stress-strain data can be directly measured for particular directions whereas the corresponding energy-strain curves remain only accessible once an equation of state is proposed. Eq. [10] displays how, by simple integration of our stress-strain *1D-SEOS*, analytical energy-strain curves can be derived using data either from experiments or from computer simulations. In the previous subsection, we have shown that our calculated (ϵ_i,σ_i) data points are well described by the proposed *1D-SEOS*. Here, the integrated *SEOS* for all the directions of materials studied in this part are represented in Fig 4.6 The symbols correspond to the energy minima at selected strains obtained from our first-principles calculations. The calculated parameters associated with the integrated forms are collected in Table 4.7

The analytical energy curves clearly reflect the good quality of the fittings (see Fig 4.6. Two parameters define the shape of each of these curves, ϵ_{sp} and E_{sp}. The first one, previously discussed in relation to the stress-strain curves (see Table 4.1), identifies the abscissa of the inflexion point, where the directional Young modulus vanishes. The ordinate of this point is E_{sp} (see Table 4.7) and correlates quite well with the critical/spinodal strength calculated along each of the directions explored for the materials under study in this part. The higher the strength, the higher the energy required to induce an elastic instability in the material.

As regards the directional Young modulus, we can easily derive a simple expression at zero stress $Y_l(0)$ involving the three parameters of the stress-strain *1D-SEOS* by evaluating Eq.[4] at zero stress:

$$Y_l(0) = \frac{\sigma_{sp}}{\sigma_{sp}(1-\gamma)}. \qquad (11)$$

This parameter is discussed below.

Table 4.7 Energy and Young modulus parameters from the integrated stress-strain SEOS fittings

Material direction	$Y_l(0)$(GPa)	E_{sp} (Ha)
B1-ZnO [100]	107.7	0.00557
[110]	167.3	0.01149
[111]	232.9	0.05654
B2-ZnO [100]	391.2	0.06041
[110]	382.3	0.01060
[111]	-	-
B3-ZnO [100]	-	-
[110]	116.0	0.01106
[111]	219.1	0.02830
B4-ZnO [100]	-	-
[110]	-	-
[$\bar{1}$10]	117.7	0.01114

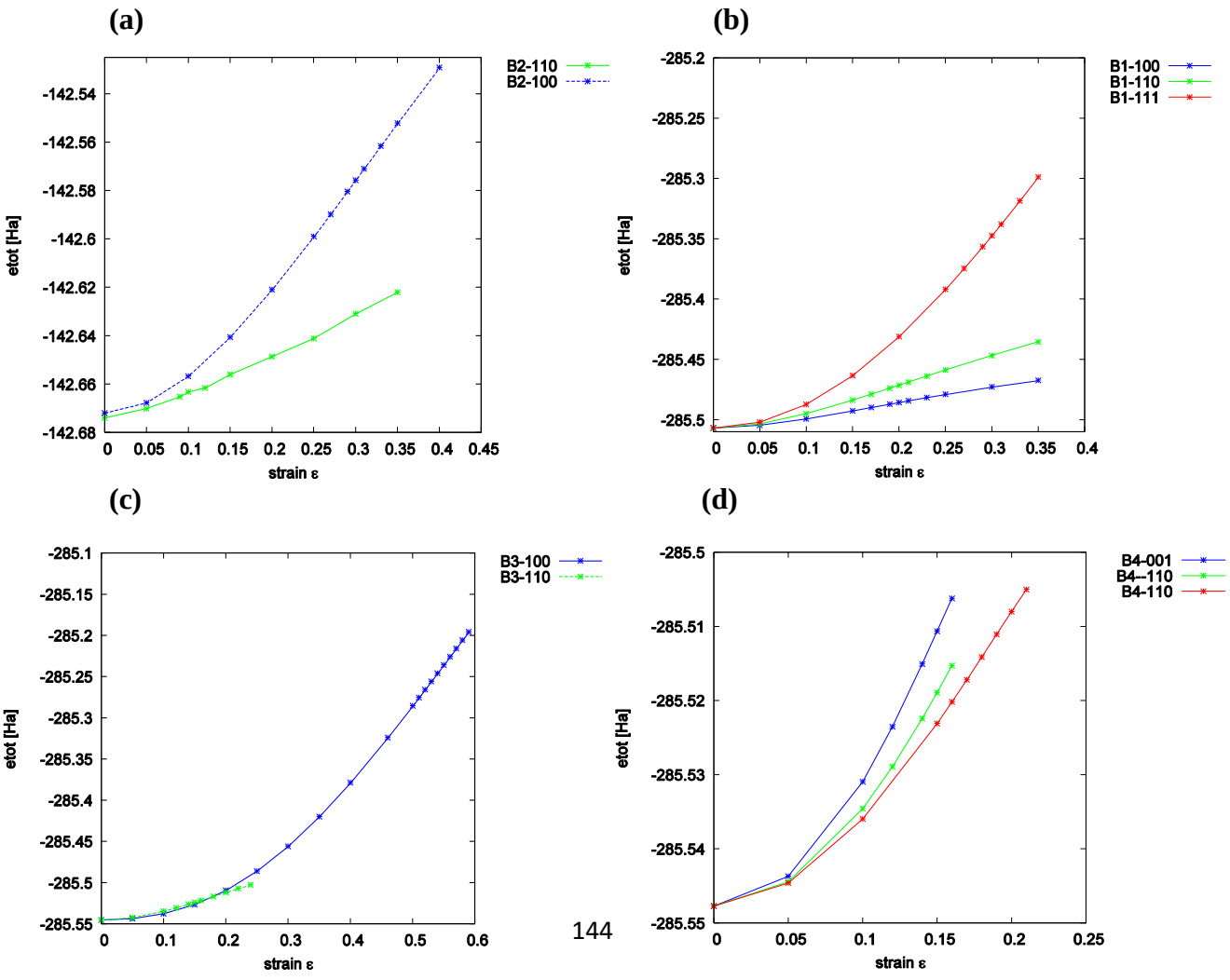

Figure 4.6. Calculated energy-strain curves for: ***(a)*** *B1-ZnO,* ***(b)*** *B2-ZnO,* ***(c)*** *B3-ZnO,* ***(d)*** *B4-ZnO.*

4.4. Layered Materials: *Graphite* and *2H-MoS2*. Results and Discussions

4.4.1. Bulk Properties

This subsection is restricted just to the summary of the equilibrium structural and elastic data of the four structures. Computed lattice constants, bulk moduli and elastic constants are collected in Table 4.8. Along with experimental and other calculated values. Overall, our results are found to be in good agreement with reported observed data, showing only slight differences due to the overestimation of the lattice constants and underestimation of the elastic constants inherent to the *GGA* level of calculations. The introduction of the *DFT-D2* correction, which is intended to take into account the *vdW* inter-layer interactions, leads our results for graphite and molybdenum disulfide to be in good agreement with the experiments and improves in general other previous local density approximation (*LDA*) or (*GGA*) results. In addition, the controversial C_{12} parameter in *2H-MoS2*, the higher discrepancy (less than 20%) is found in our calculation of C_{11} in graphite (see Table 4.8). We attribute this deviation to the above tendency of *GGA* results. Regarding C_{12} in*2H-MoS2*, the situation is different. The discrepancy between the negative value reported in the experimental paper of Feldman [70] and the positive one obtained when the *D2*-Grimmecorrection isincluded in the calculations was discussed by Peelaers and Van de Walle [71]. We only notice here that C_{12} was not directly measured but derived by Feldman using linear compressibilities reported in other works. Further details can be found in [71]. Overall, our calculated equilibrium properties provide the necessary reliable basis to undertake tensile stress simulations.

Table 4.8 Zero pressure lattice and elastic constants of graphite and *2H-MoS2*. All B_0 values calculated using Voigt elastic constants relationship.

		This work	Calculated	Experimental
Graphite	a(Å)	2.521	2.451 [72]	2.464 [73]
	c(Å)	7.067	6.582 [74]	6.712 [73]
	C_{11}(GPa)	892	1118 [75]	1109 ±16 [73]
	C_{12} (GPa)	163	235 [75]	139 ± 36 [73]
	C_{33} (GPa)	31	29 [75]	38.7 ± 7 [73]
	C_{13} (GPa)	5	8.5 [75]	0 ± 3 [73]
	C_{44} (GPa)	6	-2.8 [75]	5 ±3 [73]
	B_0 (GPa)	240	307	281
2H-MoS2	a(Å)	3.19	3.16 [76]	3.163 [77]
	c(Å)	12.56	12.296 [76]	12.341 [77]
	C_{11} (GPa)	220	218 [76]	238 [70]
	C_{12} (GPa)	45	38 [76]	-54 [70]
	C_{33} (GPa)	40	35 [76]	52 [70]
	C_{13} (GPa)	16	17 [76]	23 [70]
	C_{44} (GPa)	26	15 [76]	19 [70]
	B_0 (GPa)	75	68	57

4.4.2. Ideal strength with and without transverse stress.

This subsection is devoted to the calculation of the strain-stress curves of the two structures considered in this part. First, we collect in Fig 4.7 the results under vanishing transverse stress. For graphite, our in-plane stress-strain curves show maxima at similar strain values to those reported by Liu al. [72] for graphene, although we compute critical strengths along these directions around 25 GPa lower than in their work. This is due in part to differences between *LDA* (Liu et al.) and *GGA* (ours) levels of calculation, and on the other hand, to differences in the system, single sheet (graphene) and the bulk (graphite). To the best of our knowledge, the corresponding curve for the c-direction has not been reported so far.

Analogously, we have not found previous strain- stress curves along this direction for bulk *2H-MoS_2*, whereas for the in-plane directions the previous reported studies refer to single- or few-layers *2H-MoS_2* [78,79]. These results indicated a noticeable decreasing of σ_c as the size of the slab increases, which is also the expected trend according to our calculations.

It is usual to recall to the chemical bonding network to interpret at an atomic level differences in the strain-stress curves between compounds and/or directions. Without being strictly quantitative while keeping the basic chemical meaning, a simple and practical indicator able to account for the majority of these differences is proposed as follows. Each chemical bond in the unit cell is described by a vector connecting its two bound nearest-neighbor atoms. The projection of this vector along the corresponding tensile direction is evaluated and the sum calculated over all the bonds in the unit cell is defined as the total effective bond length (*EBL*) associated to that direction. The two main structural effects induced in the chemical bonds by the tensile strain (changes in bonding lengths and angles) are essentially captured in this parameter. *EBL* values exhibit the expected trend always increasing as the strain increases up to the stability limit.

In Fig 4.7-a,b and Fig 4.7-c,d, the responses of graphite and *2H-MoS_2* to tensile stress along the [110], [$\bar{1}$10], and [001] directions are displayed. Here, the laminar nature of these two compounds is clearly revealed by very low ideal strength values along the c-axis (ϵ_c = 0.13 and σ_c = 0.063 GPa in graphite and ϵ_c = 0.05 and σ_c = 0.069 GPa in *2H-MoS_2*) which is in concordance with the weak Van der Waals nature of the inter-layer interaction. At low strains, the in-plane graphite strains reveal an isotropic *2D*- elastic behavior in good agreement with previous *DFT* calculations [80]. At large in-plane strains, the lattice layers start to behave anisotropically and the critical stress along the next-nearest-neighbor [100] direction (ϵ_c = 0.26 and σ_c = 86 GPa in graphite and ϵ_c = 0.27 and σ_c = 22 GPa in *2H-MoS_2*) becomes greater than along the nearest-neighbor [120] direction (ϵ_c=0.11 and σ_c=78 GPa in graphite and ϵ_c=0.20 and σ_c=14 GPa in 2H-MoS2). Expected differences between stronger *C-C* than *Mo-S* intralayer bonds are also clearly manifested when comparing these data.

For all directions and structures, we now analyze new results coming from the proposed analytical *1D-SEOS*. All the curves in the four panels of Fig 4.7 were obtained from the *1D-SEOS* fittings to the calculated strain-stress data. The performance of the *1D-SEOS* is apparent and allows us to derive with confidence critical stress and critical strain values from the corresponding fitting parameters ϵ_{sp} and ϵ_{sp}, respectively. We have checked that the trends

and specific values of these two key parameters compare with high accuracy with our first-principles computed numerical values (see Table 4.1). Thus, we arrive to this interesting conclusion: the *1D-SEOS* of Eq.[7] is an appropriate analytical function for describing stress-strain data.

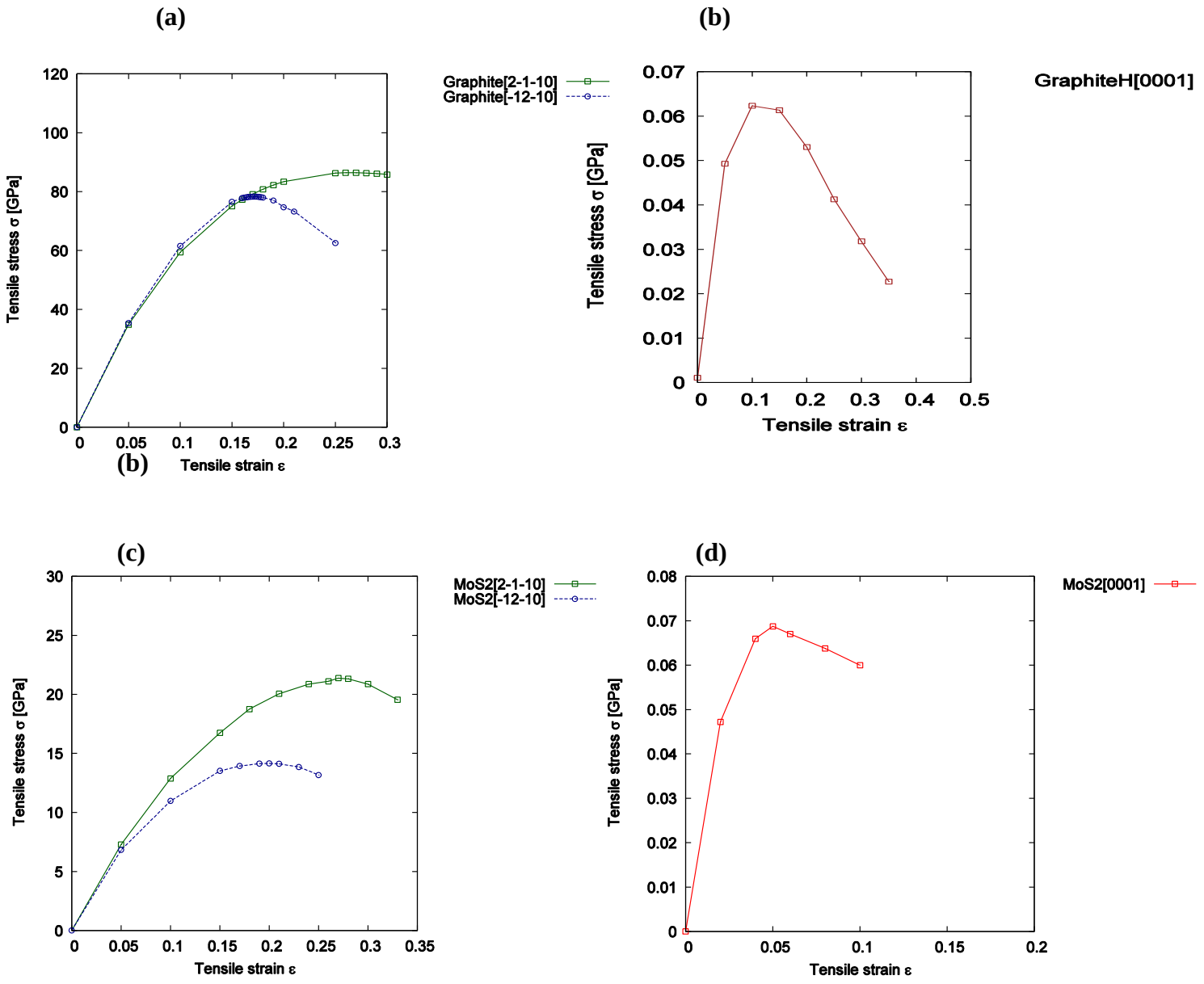

Figure 4.7 Calculated strain-stress curves without transverse stress for Graphite and for*2H-*MoS_2 (**a**),(**c**) in plane and (**b**),(**d**) normal plane.

We have noticed earlier that multi-load conditions may be present in manufacturing processes combining thermal effects and epitaxial growth. As a particular situation of these conditions, we have studied in a second round of simulations the effects of superimposing transverse stress (both compressive and tensile) on the previous tensile directions for the four structures. We detected convergence problems in some simulations that have hindered the calculations in the compressive (negative) transverse stress range in *2H-MoS_2*, and also along the [100] direction in the positive range of this compound. The expected trend is a decreasing of the critical strength as we increase the superimposed transverse stress from negative to positive values. In fact, this is the computed behavior for the majority of situations we have studied. For example, the critical strength σ_c is lowered by the transverse stress σ_t in all the directions in graphite, and *2H-MoS_2*. In this two laminar compounds, we obtain just one value at the most negative transverse stress breaking the decreasing trend along the $[\bar{1}10]$ direction. All these results are displayed in Fig 4.8. In general, the unexpected positive slope in the ideal strength-transverse stress curve appears at compressive transverse stress values. In the tensile regime, all the directions and structures show a modulated lowering of the ideal strength as the transverse tension increases which is compatible with the overall weakening of the compounds as multi-load conditions are enhanced or, in other words, to the higher strain energy stored in the material. However, we would like to notice that the opposite behavior was also found by Sestak et al. [15] and Cerný et al. [18]. The increasing of the critical strength under sumper imposed positive lateral tensile stress obtained in their calculations might be due to the different nature of the chemical bonding network. These authors deal with metallic materials where directional bonds are not identified.

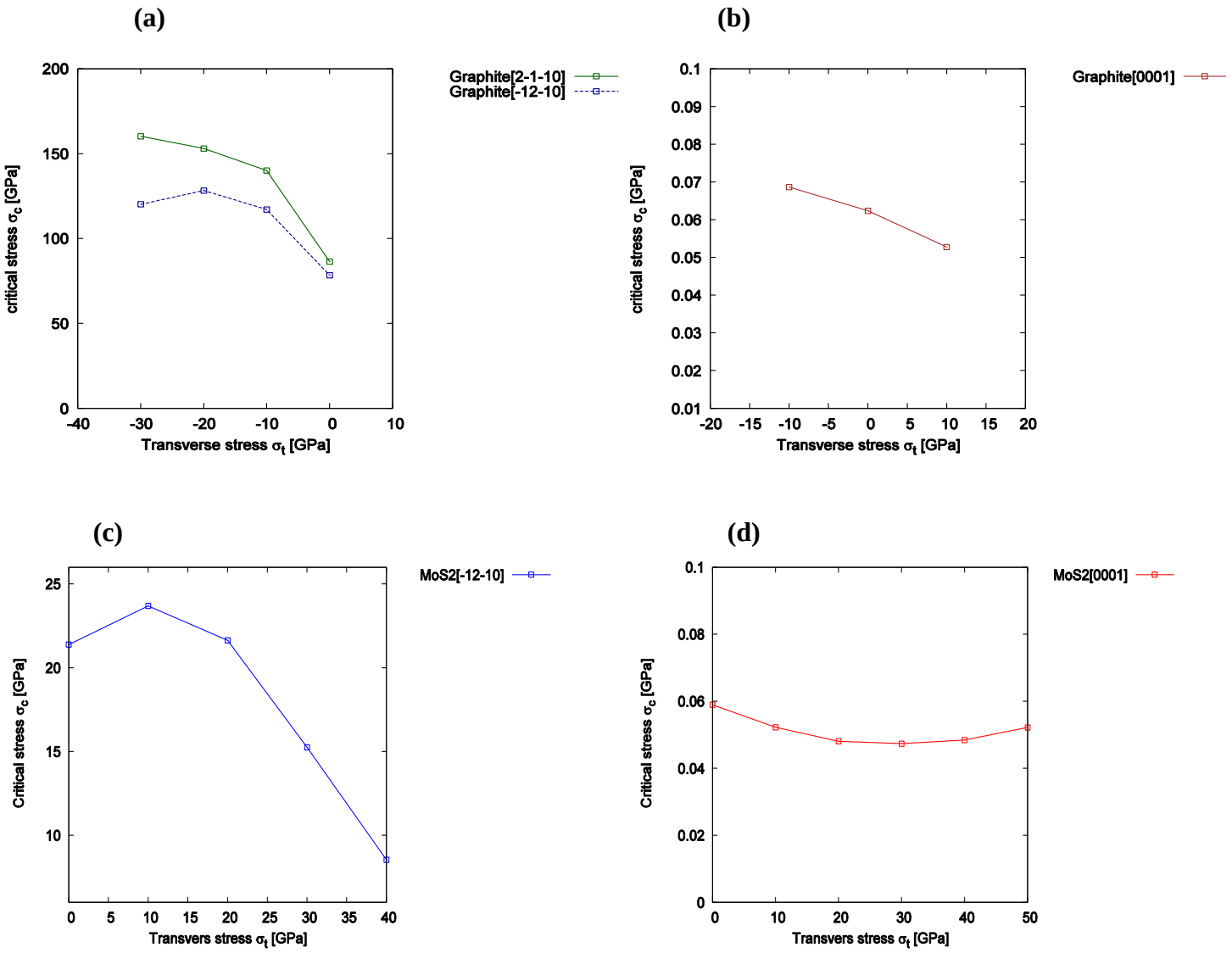

Figure 4.8 Calculated critical stress-transverse stress curves for Graphite and *2H-MoS_2* (**a**),(**c**) in plane and (**b**),(**d**) normal plane.

4.4.3 Other outcomes of the stress-strain SEOS: energetic and directional Young moduli

As stated in subsection 4.1.3, our analytical scheme allows us not only gathering information on the critical parameters, but also on the energetic of crystalline materials and on the Young moduli along specific tensile directions. From an experimental point of view, stress-strain data can be directly measured for particular directions whereas the corresponding energy-strain curves remain only accessible once an equation of state is proposed. Eq.[10] displays how, by simple integration of our stress-strain *1D-SEOS*, analytical energy-strain curves can be derived using data either from experiments or from computer simulations. In

the previous subsection, we have shown that our calculated (ϵ_i,σ_i) data points are well described by the proposed *1D-SEOS*. Here, the integrated *SEOS* for all the directions of materials studied in this part are represented in Fig 4.9. The symbols correspond to the energy minima at selected strains obtained from our first-principles calculations. The calculated parameters associated with the integrated forms are collected in Table 4.9.

The analytical energy curves clearly reflect the good quality of the fittings (see Fig 4.9. Two parameters define the shape of each of these curves, ϵ_{sp} and E_{sp}. The first one, previously discussed in relation to the stress-strain curves (see Table 4.1), identifies the abscissa of the inflexion point, where the directional Young modulus vanishes. The ordinate of this point is E_{sp} (see Table 9.) and correlates quite well with the critical/spinodal strength calculated along each of the directions explored for the materials under study in this part. The higher the strength, the higher the energy required to induce an elastic instability in the material.

As regards the directional Young modulus, we can easily derive a simple expression at zero stress $Y_l(0)$ involving the three parameters of the stress-strain *1D-SEOS* by evaluating Eq.[4]at zero stress:

$$Y_l(0) = \frac{\sigma_{sp}}{\sigma_{sp}(1-\gamma)} \qquad (11)$$

This parameter is discussed below.

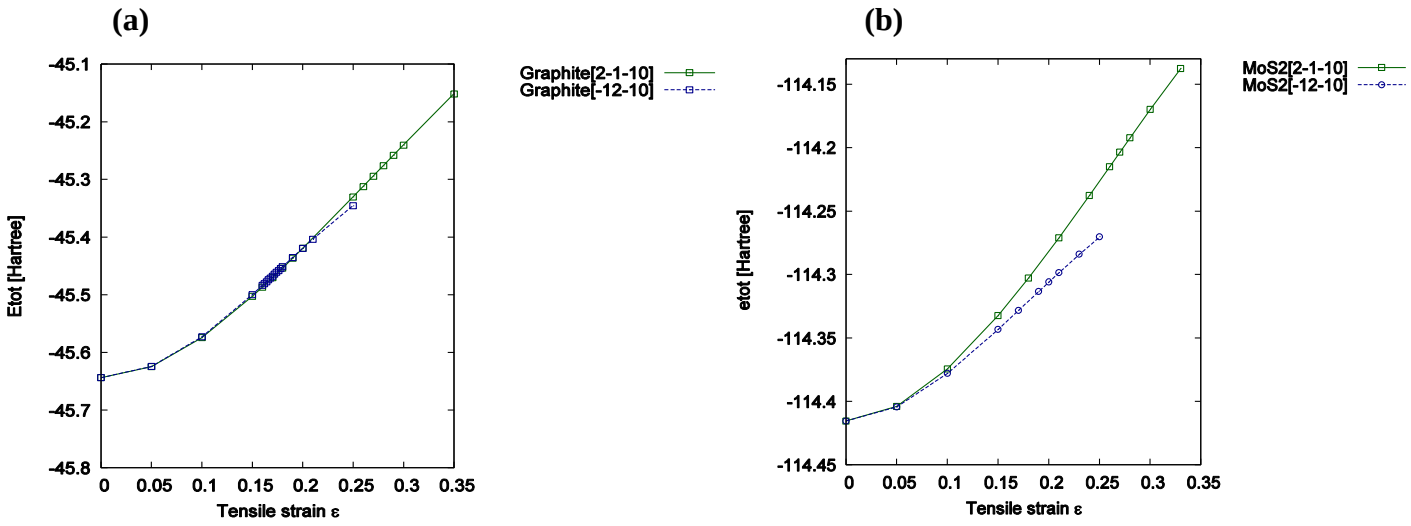

Figure 4.9 Calculated energy-strain curves for: (**a**) Graphite, and (**b**) 2H-MoS2.

Table 4.9 Energy and Young modulus parameters from the integrated stress-strain SEOS fittings

Material direction	$Y_l(0)$ (GPa)	E_{sp} (kJ/mol)
Graphite [001]	0.99< 1	-
[110]	746	201
[$\bar{1}$10]	746	113
2H-MoS2 [001]	2.41< 1	-
[110]	150	69
[$\bar{1}$10]	140	153

Let us finally conclude by analyzing these zero stress directional Young moduli in graphite and *2H-MoS_2*. Layered materials constitute a severe test for our model since weak and covalent interactions are simultaneously present. In both compounds, the van der Waals nature of the inter-layer interactions is revealed through the values of the directional Young modulus provided by the spinodal parameters. $Y_{001}(0)$ values (in GPa) are as low as 0.99 and 2.40 for graphite and *2H-MoS_2*, respectively, in contrast with the values along the [100] and [120] directions which are, respectively, 748 and 728 for graphite, and 150 and 140 for *2H-MoS_2*. The latter values can be compared with the intra-layer Young modulus reported for graphite and MoS_2 by other authors. For instance, for graphite goes from 700 to 1100 GPa ([81] and references therein), whereas for 2H-MoS_2 the values range between 130 and 220 GPa [82–84] showing a good agreement with the results obtained in this work. At this point, it must also be emphasized that our Young modulus values reflect the expected different intralayer bond strengths between the C–C and Mo–S bonds, as we previously detected in the analysis of the*1D-SEOS* parameters (see Section 4.2.2).

References

[1] Asano. K, Hayashi. T, Takayama. D, Sugawara. Y, Ryu. S.H, Palmour. J.W. **Temperature dependence of On-state characteristics, and Switching characteristics of 5 kV class 4H-SiC SEJFET.** IEEJ Trans. IA 2005, 125 (2), 147-152.

[2] Peña-Álvarez. M, del Corro. E, Morales-García. Á, Kavan. L, Kalbac. M, Frank. O. **Single Layer Molybdenum Disulfide under Direct Out-of-Plane Compression: Low-Stress Band-Gap Engineering.** NanoLetters 2015, 15, 3139–3146.

[3] Tsai. M.-L, Su. S.-H, Chang. J.-K, Tsai. D.-S, Chen. C.-H, Wu. C.-I, Wu. Li. L.-J, Chen. L.-J, He. J.-H. **Monolayer MoS_2 heterojunction solar cells.** ACS Nano 2014, 8, 8317–8322.

[4] Recio. J.M, Menéndez. J.M, Otero-de-la-Roza. A. Eds. **An Introduction to High-Pressure Science and Technology**. CRC-Press, Boca Raton, 2016.

[5] Radisavljevic. B, Radenovic. A, Giacometti. V, Kis. **A. Single-layer MoS2 transistors.** Nat. Nanotechnol. 2011, 6, 147-150.

[6] Wang. H, Yu. L, Lee. Y.H, Shi. Y, Hsu. A, Chin. M.L, Li. L.J. Dubey, M. Kong. J, Palacios. T. **Integrated circuits based on bilayer MoS2 transistors.** Nano Lett. 2012, 12, 4674-4680.

[7] Fiori. G, Szafranek. B.N, Iannaccone. G, Neumaier. D. **Velocity saturation in few-layer MoS2 transistor.** Appl. Phys. Lett 2013, 103, 233509(1)-233509(4).

[8] Kim. S, Konar. A, Hwang. W.S, Lee. J.H, Yang. J, Jung. C, Kim. H, Yoo. J.B, Choi. J.Y. **High-mobility and low-power thin-film transistors based on multilayer MoS2 crystals.** Nat. Commun. 2012, 3, 1011-1017.

[9] Bollmann.W, Spreadborough. J. **Action of Graphite as a Lubricant.** Nature 1960, 186, 29-30.

[10] Peelaers. H, Van de Walle C. G. **Elastic Constants and Pessure-Induced Effects in MoS2.** J. Phys. Chem. 2014, 118, 12073-12076.

[11] Kohn, W.; Sham, L.J. **Self-Consistent Equations Including Exchange and Correlation Effects.** Phys. Rev. 1965, 140A, 1133-1138.

[12] Argaman, N.; Markov, G. **Density functional theory: An introduction. Am. J. Phys. 2000, 68(1), 69-79. 13.**

[13] Umeno, Y.; Kitamura, T. **Ab Initio Simulation on Ideal Shear Strength of Silicon.** Mater. Sci. Eng. 2002 , B 88-1, 79-84.

[14] Cerný, M.; Rehák, P.; Umeno, Y.; Pokluda, J. **Stability and strength of covalent crystals under uniaxial and triaxial loading from first principles.** J. Phys. Condens. Matter 2013, 25, 35401-35408.

[15] Sesták, P.; Friák,M.; Holec, D.; Vsianská,M.; Sob,M. **Strength and brittleness of interfaces in Fe-Al superalloy nanocomposites under multiaxial loading: an ab initio and atomistic study.** Nanomaterials 2018, 8, 873.

[16] Umeno, Y.; Cerný, M. **Effect of normal stress on the ideal shear strength in covalent crystals.** Phys. Rev. B 2008, 77, 100101-100104.

[17] Umeno, Y.; Cerný, M. **Ideal shear strength under compression and tension in C, Si, Ge, and cubic SiC: an ab initio density functional theory study.** J. Phys. Condens. Matter 2011, 23, 385401(1)-385401(7).

[18] Cerný. M, Rehák. P, Pokluda. J. **The origin of lattice instability in bcc tungsten under triaxial loading.** Philos. Mag. 2017, 97, 2971-2984.

[19] Baonza, V.G.; Cáceres, M.; Núñez. **J. Universal compressibility behavior of dense phases.** Phys. rev. B 1995, 51, 28-37.

[20] Francisco, E.; Bermejo, M.; García Baonza, V.; Gerward, L.; Recio, J.M. **Spinodal equation of state for rutile TiO2.** Phys. Rev. B 2003, 67, 064110(1)- 064110(8).

[21] Gonze, X.; Beuken, J.M.; Caracas, R.; Detraux, F.; Fuchs, M.; Rignanese, G.M.; Sindic, L.; Verstraete M.; Zerah, G.; Jollet, F.; Torrent,M.; Roy, A.; Mikami,M.; Ghosez, Ph.; Raty, J.Y.; Allan, D.C. **First-principles computation of material properties: The ABINIT software project.** Mater. Sci. 2002; 478-492.

[22] Gonze, X.; Amadon, B.; Anglade, P.-M.; Beuken, J.-M.; Bottin, F.; Boulanger, P.; Bruneval, F.; Caliste, D.; Caracas, R.; Côté, M.; Deutsch, T.; Genovese, L.; Ghosez, Ph.; Giantomassi, M.; Goedecker, S.; Hamann, D. R.; Hermet, P.; Jollet, F.; Jomard, G.; Leroux, S.; Mancini, M.; Mazevet, S.; Oliveira, M. J. T.; Onida, G.; Pouillon, Y.; Rangel, T.; Rignanese, G.-M.; Sangalli, D.; Shaltaf, R.; Torrent, M.; Verstraete, M. J.; Zerah, G.; Zwanziger, J. W. **ABINIT: First-principles approach to material and nanosystem properties.** Comput. Phys. Commun. 2009, 180, 2582-2615.

[23] Perdew, J.P.; Burke, K.; Ernzerhof, M. **Generalized Gradient Approximation Made Simple**. Phys. Rev. Lett.; **1996**, 77, 3865-3868.

[24] Grimme, S. **Semiempirical GGA-Type Density Functional Constructed with a Long-Range Dispersion Correction.** J. Comp. Chem.; **2006**, 27, 1786-1799.

[25] Ambrosetti, A.; Ferri, N.; Di Stasio, R.A., Jr.; Tkatchencko, A. **Wavelike charge density fluctuations and van der Waals interactions in the nanoscale.** Science **2016**, 351, 1171–1176.

[26] Ambrosetti, A.; Silvestrelli, P.L. **Hidden by graphene—Towards effective screening of interface van derWaalsinteractions vian monolayer coating.** Carbon **2018**, 139, 486–491.

[27] Ambrosetti, A.; Silvestrelli, P.L. Faraday-like Screening by Two-Dimensional Nanomaterials: **A Scale Dependent Tunable Effect.**J. Phys. Chem. Lett. **2019**, 10, 2044–2050.

[28] Trouillier, N.; Martins, J.L. **Efficient pseudopotentials for plane-wave calculations.** Phys. Rev. B; 1991, 43, 3, 1993-2006 .

[29] Monkhost, H.J.; Pack, J.D.**Special points for Brillouin-zone integrations.**Phys. Rev. B; 1976, 13, 5188-5192.

[30] Momma, K.; Izumi, **F. VESTA 3 for three-dimensional visualization of crystal, volumetric and morphology data.**J. Appl. Crystallogr.**2011**, 44, 1272–1276.

[31] Born, M.; Huang, K. **Dynamical Theory of Crystal Lattice,** Oxford Clarendon Press, London, 1966.

[32] Zeina M.J.; Servio, P.; Rey A.D. **Ideal Strength of Methane Hydrate and Ice Ih from First-Principles**. Cryst. Growth. Des.; **2015**, 15, 5301-5309.

[33] Otero de la Roza, A.; Luaña, V. **Runwien: a text-based interface for the WIEN package. Computer Physics Communications**. 2009, 180, 800–812.

[34] Baonza, V.G.; Taravillo, M.; Cáceres, M.; Núñez, J. **Universal features of the equation of state of solids from a pseudospinodal hypothesis.** Phys. rev. B; 1996, 53, 5252-5258.

[35] Baonza, V.G, Cáceres, M, Núñez, J. **Universal compressibility behavior of dense phases.** J. Chem. Phys.; 1994, 19, 4955-4958.

[36] Taravillo, M.; Baonza, V.G.; Núñez, J.; Cáceres, M. **Simple equation of state for solids under compression.** Phys. rev. B; 1996, 54, 7034-7045.

[37] Baonza, V.G.; Cáceres, M.; Núñez, J. **High-pressure compressibility behavior of liquids referred to apseudospinodal curve.** Chem. Phys. Lett.; 1994, 228, 137-143.

[38] Baonza, V.G.; Cáceres, M.; Núñez, J. **Universal Behavior of Compressed Liquids.** J. Chem. Phys.; 1994, 19, 4955-4958.

[39] Francisco, E.; Bermejo, M.; García Baonza, V.; Gerward, L.; Recio, J.M. **Spinodal equation of state for rutile TiO2.** Phys. Rev. B; 2003, 67, 064110(1)- 064110(8).

[40]Ogata, S.; Li, J.; Shibutant, N.; Yip, S. **Ideal shear strain of metals and ceramics.** Phys. Rev. B 2004, 70, 104104(1)-104104(7).

[41] Brosh, E.; Makov, G.; Shneck, R.Z. **The spinodal constraint on the equation of state of expanded fluids.** J. Phys.: Condens. Matter; 2003, 19, 2991-3001.

[42] Karch, K.; Pavone, P.; Windl, W.; Schuelt, O.; Strauch, D. **Ab initio calculation of structural and lattice-dynamical properties of silicon carbide.** Phys. Rev. B; 1994, 50, 17054-17063.

[43] Umeno, 468 Y.; Kubo, A.; Nagao, S. **Density functional theory calculation of ideal strength of SiC and GaN: Effect of multi-axial stress.** Comput. Mater. Sci.; 2015, 109, 105-110.

[44] Ioffe institut, 2003. Available online: **http:// www.ioffe.ru/SVA/NSM**(accessed on 18 August 2019).

[45] Li, Z.; Brandt, R.C. **The single-crystal elastic constants of cubic (3C) SiC to 1000 °C.** J. Mater. Sci.; 1987, 22, 2557-2559.

[46] Saramasak, K.; Limpijumnong, S.; Lambrecht, W.R.L. **First principles calculations of elastic properties under pressure.** Comput. Mater. Sci.; 2010, 49, 543-546.

[47] Villard, P.; Calvert, L.D. **Pearson's Handbook of Crystallographic Data for intermetallic Phases.** ASM international. Cleveland. 1991.

[48] Kamitani, K.; Grimsditch, M.; Nipko, J. C.; Loong, C.K.; Okada, M.; Kimura, I. **The elastic constants of silicon carbide: A Brillouin-scattering study of 4H and 6H SiC single crystals.** J. Appl. Phys.; 1997, 82, 3152-3154.

[49] Jan Wrobel, Jacek Piechota. **On the structural stability of ZnO phases.** Solid State Communications 146 (2008) 324–329

[50] M. Kalay, H.H. Kart, S. Ozdemir Kart, T. Cagın. **Elastic properties and pressure induced transitions of ZnO polymorphs fromfirst-principle calculations.** Journal of Alloys and Compounds 484 (2009) 431–438

[51] S.Q. Wang, **A comparative first-principles study of ZnS and ZnO in zinc blende structure.** J. Crystal Growth 287 (2006) 185.

[52] A.B.M.A. Ashrafi, A. Ueta, A. Avramescu, H. Kumano, I. Suemune, Y.-W. Ok, T.-Y. Seong, **Growth and characterization of hypothetical zinc-blende ZnO films on GaAs (001) substrates with ZnS buffer layers.** Appl. Phys. Lett. 76 (2000) 550

[53] B. Amrani, I. Chiboub, S. Hiadsi, T. Benmessabih, N. Hamdadou.**Structural and electronic properties of ZnO under high pressures.** Solid StateCommun. 137 (2006) 395–399.

[54] S. Desgreniers, **Structural and compressive parameters High-density phases of ZnO.** Phys. Rev. B 58 (1998) 14102–141105.

[55] S. Saib, N. Bouarissa, **Structural parameters and transition pressures of ZnO: ab-initio calculations.** Phys. Stat. Sol. (b) 244 (2007) **1063–1069.**

[56] D. Maouche, F. Saad Saoud, L. Louail, **Effect of pressure on the structural and elastic properties of ZnS and MgS alloys in the B3 and B1 phases.** Mater. Chem. Phys. 106 (2007) 11–15.

[57] H. Karzel, W. Potzel, M. Kofferlein, W. Scheiessl, M. Steiner, U. Hiller, G.M.Kalvius, D.W. Mitchell, T.P. Das, P. Blaha, K. Schwarz, M.P. Pasternak. **Lattice dynamics and hyperfine interactions in ZnO and ZnSe at high external pressures.** Phys. Rev. B 53 (1996) 11425–11438.

[58] X. Wu, D. Vanderbilt, D.R. Hamann. **Systematic treatment of displacements, strains, and electric fields in density-functional perturbation theory.** Phys. Rev. B 72 (2005) 035105.

[59] J.A. Sans, A. Segura, F.J. Manjon, B. Mari, A. Munoz, M.J. Herrara-Cabrera. **Optical properties and electronic structure of rock-salt ZnO under pressure**. Microelectron. J. 36 (2005) 928–932.

[60] T.B. Bateman. **Elastic moduli of single-crystal zinc oxide.** J. Appl. Phys. 33 (1962) 3309.

[61] Z.G. Yu, H. Gong, P.Wu. **Lattice dynamics and electrical properties of wurtzite ZnO determined by a density functional theory method.** J. Cryst. Growth 287 (2006) 199–203.

[62] G. Kresse, J. Hafner. **Ab initio molecular-dynamics simulation of the liquid-metal–amorphous-semiconductor transition in germanium.** Phys. Rev. B 49 (1994) 14251–14269

[63] M. Catti, Y. Noel, R. Dovesi. **Full Piezoelectric Tensors of Wurtzite *and* Zinc Blende ZnO.** J. Phys. Chem. Solids 64 (2003) 2183.

[64] P. Gopal, N.A. Spalpin. **Polarization, piezoelectric constants and elastic constants of ZnO, MgO and CdO.** J. Electron. Mater. 35 (2006) 538–542.

[65] S.P. Łepkowski, J.A. Majewski, G. Jurczak. **Nonlinear elasticity in III-N compounds: Ab initio calculations.** Phys. Rev. B 72 (2005) 245201.

[66] T. Azuhata, M. Takesada, T. Yagi, A. Shikanai, S.F. Chichibu, K. Torii,A. Nakamura, T. Sota, G. Cantwell, D.B. Eason, C.W. Litton. Brillouin scattering study of ZnO. J. Appl.Phys. 94 (2003) 968.

[67] G. Carlotti, D. Fioretto, G. Socino, E. Verona. **Elastic properties and pressure induced transitions of ZnO polymorphs from first-principle calculations.** J. Phys. Condens. Matter 7 (1995) 9147–9153

[68] Li-Zhi Xu, Yue-Lin Liu and Hong-Bo Zhou. **Ideal strengths, structure transitions and bonding properties of a ZnO single crystal under tension**. J. Phys. Condens. Matter 21 (2009)

[69] Feldman, J. L. **Elastic constants of 2H-MoS2 and 2H-NbSe2 extracted from measured dispersion curves and linear compressibilities**. J. Phys. Chem. Solids; 1976, 37, 1141-1144.

[70] Peelaers, H.; Van de Walle. **C.G. Elastic Constants and Pressure-Induced Effects in MoS_2.** J. Phys. Chem. **2014**,118, 12073–12076.

[71] Liu, F.; Ming, P.; Li, J. **Ab initio calculation of ideal strength and phonon instability of graphene under tension.** Phys. Rev. B; 2007, 76, 064120(1)- 064120(7).

[72] Bosak, A.; Krisch, M.; Mohr, M.; Maultzsch, J.; Thomsen, C.**Elasticity of single-crystalline graphite: Inelastic x-ray scattering study.** Phys. Rev. B; 2007, 75, 153408(1)-153408(4).

[73] Ooi, N.; Rairkar, A.; Adams, J.B. **Density functional study of graphite bulk and surface properties.** Carbon; 2006, 44, 231-242.

[74] Mounet, N.; Marzari, N. **First-principles determination of the structural, vibrational and thermodynamic properties of diamond, graphite, and derivatives.** Phys. Rev. B; 2005, 71, 205214(1)-205214(14).

[75] Alexiev, V.; Prins, R.;Weber, T. **Ab initio study of MoS2 and Li adsorbed on the (10-10) face of MoS2.** Phys. Chem. Chem. Phys.; 2000, 2, 1815-1827.

[76] Fan, D.; Xu, J.; Ma, N.; Liu, J.; Xie,**H. P-V-T Equation of state of molibdenite (MoS_2) by a diamond anvil cell and in situ synchrotron angel-dispersive X-ray diffraction.** Physica B;2014, 451, 53-57.

[77] Li, T. **Ideal strength and phonon instability in single-layer MoS2.** Phys. Rev. B; 2012, 85, 235407(1)-235407(5).

[78] Li, P.; Jiang, C.; Xu, S.; Zhuang, Y.; Gao, L.; Hu, A.; Wang, H.; Lu, Y. **In situ nanomechanical characterization of multi-layer MoS2 membranes: from intraplanar to interplanar fracture.** Nanoscale; 2017,9, 9119-9128.

[79] Abbasi-Pérez, D.; Menéndez, J.M.; Recio, J.M.; Otero-de-la-Roza, A.; del Corro, E.; Taravillo, M.; Baonza, V.G.; Marqués, M. **Modeling graphite under stress: equations of state, vibrational modes, and interlayer friction.** Phys. Rev. B; 2014, 90, 054105(1)-054105(10).

[80] Sestak, P. Friak, M. Holec, D. Vsianska, M. **Strength and brittleness of interfaces in fe-Al superalloy nanoconposites under multiaxialloading:An abinitio and atomistic study.**Nanomaterials 2018, 8, 873.

[81] M. Cerny, P. Rehak, J. Pokluda.**The origine of lattice instability in bcc tungsten under triaxial loading.** Philos. Mag. 2017, 97, 2971-2984.

[82] Bertolazzi, S.; Brivio, J.; Kis, **A. Stretching and Breaking of Ultrathin MoS2.** ACS Nano; 2011, 5, 9703-9709.

[83] Lorenz, T.; Teich, D.; Joswig, J.O.; Seifert, G. **Theoretical Study of the Mechanical Behavior of Individual TiS2 and MoS2 Nanotubes.** J. Phys. Chem. C; 2012, 116, 11714-11721.

[84] Cooper, R.C.; Lee, C.; Marianetti, C.A.; Wei, X.; Hone, J.; Kysar, J.W. **Nonlinear elastic behavior of two-dimensional molybdenum disulfide.** Phys. rev. B; 2013, 87, 035423-1-035423-11.

CONCLUSIONS AND OUTLOOK

Conclusions

The ideal strength of *3C*- and *2H-SiC, ZnO*-polymorphs, graphite, and *2H-MoS_2*were evaluated by means of first principles quantum-mechanical methodologies based on the *DFT* approximation. Both, vanishing and superimposed transverse stress over uniaxial tensile strains were considered in order to evaluate the ideal strength of the all crystalline structures. The ideal strength is found to depend on the particular crystallographic direction revealing the expected stronger mechanical anisotropy in the layered and ionic compounds. We introduced the *DFT-2D* correction which take into account the vdW interactions in graphite and molybdenum disulfide layers. After an isotropic behavior at the low strain regime, we observe a different behavior along the two in-plane directions, being the ideal tensile strength smaller in the nearest-neighbor than in the next-nearest-neighbor direction. In these crystals, the lowest value of σ_c is obtained in the c-direction as expected given the weak inter-layer vdW interactions. The ideal tensile strength is generally decreased by the transverse tension. Reduction in the ideal strength by large transverse compression occurs in some structures and orientations in concordance with an increasing on the effective bond lengths in those conditions. The critical stress in all directions at all transverses loads were related and explained in terms of Effective Bond Lengths for the *SiC*-polymorphs compound.

We present a new *1D-SEOS* analytical function that was successfully applied to the computed strain-stress data points, and that can be also used to describe results from tensile stress experiments. The spinodal strain ϵ_{sp} along with the corresponding spinodal stress σ_{sp} fitting parameters have been calculated for the two covalent (*SiC*), the two layered (MoS_2 and Graphite)and the four ionic (*ZnO*) compounds. These parameters are identified with the critical strength and strain values provided they appear at the instability elastic limit. In addition, the integrated energy-strain *SEOS* reveals to be an interesting equation enclosing information on the energy stored in the material along tensile processes and providing data on the required energy to reach the instability elastic limit.

Outlook

Several extensions can be foreseen as regards the current study. We enumerate here the most straightforward directions that can be considered for future work.

- Ideal shear strength evaluation in some planes along specific directions.
- n-Layer study for graphite and molybdenum disulfide.
- Comparison of hydrostatic and non-hydrostatic conditions effects.
- Extension of the *1D-SEOS* analytical function to the take into account transverse stress effects.
- Simulation and computation of the impact of defects on the mechanical properties of these prototypical materials.

Conclusiones

La resistencia ideal de los politipos 3C y 2H del SiC, distintos polimorfos de ZnO, grafito y 2H-MoS2 se evaluó mediante metodologías de primeros principios de la mecánica cuántica basadas en la aproximación DFT. Se consideró tanto la tensión transversal superpuesta sobre las tensiones de tracción uniaxiales como su ausencia para evaluar la resistencia ideal de todas las estructuras cristalinas. Se encuentra que la resistencia ideal depende de la dirección cristalográfica particular, hecho que revela una anisotropía mecánica más fuerte en los compuestos laminares e iónicos. Introdujimos la corrección DFT-2D que tiene en cuenta las interacciones vdW en capas de grafito y disulfuro de molibdeno. Después de un comportamiento isotrópico en el régimen de baja tensión, observamos un comportamiento diferente a lo largo de las dos direcciones en el plano, siendo la resistencia a la tracción ideal más pequeña en la dirección de primeros vecinos que en la dirección de segundos vecinos. En estos cristales, el valor más bajo de σ_c se obtiene en la dirección c como se esperaba dada la débil interacción vdW entre capas. La resistencia a la tracción ideal generalmente disminuye por la tensión transversal. La reducción de la resistencia ideal mediante una gran compresión transversal se produce en algunas estructuras y orientaciones en concordancia con un aumento de las longitudes de enlace efectivas en esas condiciones. El esfuerzo crítico en todas las direcciones y en todas las cargas transversales se relacionó y explicó en términos de longitudes de enlace efectivas para los polimorfos del el compuesto SiC.

Presentamos una nueva función analítica 1D-SEOS que se aplicó con éxito a los puntos tensión-esfuerzo calculados, y que también se puede usar para describir los resultados de los experimentos de tensión. La deformación espinodal ϵ_{sp} junto con los parámetros de ajuste de la tensión spinodal correspondiente, $\sigma_{sp,}$ se han calculado para los dos politipos covalentes (SiC), los dos compuestos laminares (MoS2 y Graphite) y los cuatro polimorfos iónicos (ZnO). Estos parámetros se identifican con los valores críticos de resistencia y deformación siempre que aparezcan en el límite elástico de inestabilidad. Además, la SEOS integrada de revela ser una ecuación interesante que incluye información sobre la energía almacenada en el material a lo largo de los procesos de tracción y proporciona datos sobre la energía requerida para alcanzar el límite elástico de inestabilidad.

Perspectivas

Se pueden prever varias extensiones con respecto al estudio actual. Enumeramos aquí las líneas de investigación más inmediatas que se pueden considerar para trabajos futuros.

- Evaluación de la resistencia ideal en algunos planos a lo largo de direcciones específicas.
- Estudio de sistemas de n-capas para grafito y disulfuro de molibdeno.
- Comparación de los efectos de las condiciones hidrostáticas y no hidrostáticas.
- Extensión de la función analítica 1D-SEOS para tener en cuenta los efectos del estrés transversal.
- Simulación y cálculo del impacto de los defectos en las propiedades mecánicas de estos materiales prototípicos.

PAPER

nanomaterials

MDPI

Article

Computational Modeling of Tensile Stress Effects on the Structure and Stability of Prototypical Covalent and Layered Materials

Hocine Chorfi [1,2], Álvaro Lobato [1,3], Fahima Boudjada [2,4], Miguel A. Salvadó [1], Ruth Franco [1], Valentín G. Baonza [3,5] and J. Manuel Recio [1,*]

1 MALTA-Consolider Team and Departamento de Química Física y Analítica, Universidad de Oviedo, E-33006 Oviedo, Spain; zahraoviedo@gmail.com (H.C.); a.lobato@ucm.es (Á.L.); mass@uniovi.es (M.A.S.); ruth@uniovi.es (R.F.)
2 Physics Department, University of Constantine 1, Constantine 25017, Algeria; boudjadafahima@yahoo.fr
3 MALTA-Consolider Team and Departamento de Química Física, Universidad Complutense de Madrid, E-28040 Madrid, Spain; vgbaonza@ucm.es
4 Institut Lumiere Matiere, Université Claude Bernard Lyon 1, CNRS, F-69622 Villeurbanne, France
5 Instituto de Geociencias, IGEO, CSIC-UCM, E-28040 Madrid, Spain
* Correspondence: jmrecio@uniovi.es; Tel.: +34-985-103036

Received: 18 September 2019; Accepted: 14 October 2019; Published: 18 October 2019

Abstract: Understanding the stability limit of crystalline materials under variable tensile stress conditions is of capital interest for technological applications. In this study, we present results from first-principles density functional theory calculations that quantitatively account for the response of selected covalent and layered materials to general stress conditions. In particular, we have evaluated the ideal strength along the main crystallographic directions of 3C and 2H polytypes of SiC, hexagonal ABA stacking of graphite and 2H-MoS_2. Transverse superimposed stress on the tensile stress was taken into account in order to evaluate how the critical strength is affected by these multi-load conditions. In general, increasing transverse stress from negative to positive values leads to the expected decreasing of the critical strength. Few exceptions found in the compressive stress region correlate with the trends in the density of bonds along the directions with the unexpected behavior. In addition, we propose a modified spinodal equation of state able to accurately describe the calculated stress–strain curves. This analytical function is of general use and can also be applied to experimental data anticipating critical strengths and strain values, and for providing information on the energy stored in tensile stress processes.

Keywords: ideal strength; quantum-mechanical calculations; SiC; graphite; molybdenum disulfide; spinodal equation of state

1. Introduction

A clear understanding of the cohesive and mechanical properties of technological materials is of capital importance especially when applications are demanded in environments with hostile thermal, stress, and chemical conditions. Since the nature of the crystalline bonding networks is ultimately responsible for the response of the compounds to these external conditions, it is rewarding and necessary to investigate how macroscopic properties correlate with chemical interactions at an atomic level. Covalent and layered solids constitute two crystal families currently attracting interest in a variety of areas such as electronics and solar cell industries [1–3]. These compounds provide a good target to examine how changes in strong and weak interactions affect the observed elastic stability of materials. To this end, computer simulations constitute a practical research route to microscopically

analyze strained structures of solids since geometries optimized by minimizing the crystal energy can be accurately obtained from first-principles electronic structure calculations under different stress conditions (see for example, [4]).

Within the above two families of compounds, silicon carbide (SiC), graphite and molybdenum disulfide (MoS_2) are pertinent examples because, besides their genuine bonding networks, they are materials with a variety of applications in several technological sectors, such as new semiconductor devices, field effect transistors [1,2,5–8], lubricants [9,10], and components of solar cell panels [3]. In the manufacturing processes of these materials, mechanical failure may occur as a result of the stresses induced during the heating cycles to which the compounds are subjected. In addition, the simultaneous existence of covalent and van der Waals (vdW) interactions leads to preferential bi-dimensional and three-dimensional atomic arrangements in their crystalline structures that result in a high anisotropic response of these materials under variable stress conditions which is worth exploring.

The challenge consists in the accurate calculation of the limiting tension that these materials can support in particular directions. Considering perfect non-defective crystals, this maximum tension is known as the ideal or critical strength (σ_c) of the material for that direction. Both experimentally and theoretically, the evaluation of strain-stress curves constitutes the usual strategy to access this quantity, since after this critical point a catastrophic scenario emerges in the form of a crystal fracture or a phase transition. It then seems required to understand how the atomic level interactions correlate with the mechanism of failure in these environmental conditions and, if possible, anticipate the onset of the catastrophic scenario.

A number of theoretical studies using first-principles calculations, mainly employing density functional theory (DFT) [11,12], have permitted a quantitative evaluation of the critical strength of various materials (see [13–15] and references therein) showing that the effect of multi-axial stress obviously depends on the atomic species involved [16–18]. However, to the best of our knowledge, none of these studies have addressed the description of the observed or calculated stress–strain data by means of analytical functions as normally happens in high-pressure and related fields. Such equations of state would open the possibility of anticipating critical values for the strength and strain of materials without reaching the instability condition. In this regard, it is pertinent to recall the spinodal equation of state (SEOS) [19]. This analytical function was designed to describe the high-pressure behavior of condensed matter using as a reference state the onset of elastic instability. It has been successfully applied not only to the description of experimental and theoretical pressure-volume data, but also to the pressure evolution of one dimensional unit cell parameters [20]. Along with this fact, the SEOS is particularly well suited for the description of both experimental and theoretical stress–strain data derived from variable stress tensile conditions since, in the limit, these conditions precisely lead to the elastic instability of the material, i.e., the reference state for this analytical equation of state (EOS) .

In this study, we performed DFT calculations to obtain the critical strength of 3C and 2H polytypes of SiC, graphite and 2H-MoS_2 along their main crystallographic directions, with and without superimposed transverse stress conditions. The results are analyzed in terms of the density of chemical bonds and atomic interactions in the investigated directions of these materials. We are particularly interested in general analytical functions able to represent the behavior of different types of compounds under these tensile conditions and to reproduce the critical parameters. To this end, we propose a new SEOS form that uses the critical strain as the reference state, and that can be easily used to fit both the experimental and calculated stress–strain data.

Our paper is divided in three more sections. In the next section, we present the computational details of the electronic structure calculations and the algebra related with the new EOS. Section 3 contains the results and the discussion and is divided into three subsections, devoted, respectively, to the equilibrium properties of the four compounds, the stress–strain calculated curves, and the energetics and Young moduli derived from the proposed SEOS. The paper ends with a summary of our main findings.

2. Computational Details

2.1. Electronic Structure Calculations

First-principles electronic energy calculations and geometry optimizations under the Kohn–Sham DFT framework of 3C and 2H polytype structures of SiC, ABA stacking of graphite and hexagonal 2H-MoS_2 are carried out with the ABINIT code [21,22] using the Perdew–Burke–Ernzerhof (PBE) exchange-correlation functional [23]. In order to take into account van der Waals forces, the correction (DFT-D2) to the exchange-correlation term, as proposed by Grimme [24], is used for graphite and MoS_2. Although this pairwise approach does not capture many-body effects inherent to van der Waals interactions (see for example [25–27]), it has been proven to be accurate enough to determine optimized geometries involving the length scale (Å) of the tensile phenomena explored in this work. The so-called FHI atomic plane wave pseudopotentials [28] are adopted, while cut off energies and Monkhorst–Pack grids [29] are set to 1000 eV and $6 \times 6 \times 6$ and $6 \times 6 \times 4$ for 3C-SiC and 2H-SiC respectively, 1200 eV and $6 \times 6 \times 3$ for graphite, and 400 eV and $6 \times 6 \times 2$ for 2H-MoS_2. Atomic positions were optimized until the total energy converged within 0.1 meV. At the same time, all the strain components (except in the applied loading direction) were optimized so that the corresponding stress components turned out to be within 100 MPa from a predetermined value. The Broyden–Fletcher–Goldfarb–Shanno minimization scheme (BFGS) [22] was used. In this way, tensile-strain curves under controlled normal stress were obtained. Ideal strength (critical strength from now on) was determined as the maximum value of tensile stress before the lattice loses stability and the forces diverge. Multi-axial stress calculations have been performed superimposing a transverse stress to the chosen stress direction. Atomic positions and movements through the different paths are analyzed using the visualization program for structural models (VESTA code) [30].

For the cubic 3C-SiC polytype, we calculate how the stress increases along the [100], [110] and [111] symmetry directions. For the hexagonal 2H-SiC polytype, and graphite and 2H-MoS_2 layered crystals, calculations were performed along the inter-plane direction ([001]) perpendicular to the layers, and two in-plane directions, one containing nearest neighbors ([120], so-called zigzag direction) and the other connecting next nearest neighbors ([100], so-called armchair direction).

The stress tensor is calculated in ABINIT as the derivative of the total energy with respect to the strain tensor. The strain tensor, ϵ, can be calculated from the relation between the strain-free lattice vector of a given atom μ, $\vec{r_\mu}$, and its strained lattice vector, $\vec{r'_\mu}$, as follows [31]:

$$r'^{\alpha}_{\mu} = r^{\alpha}_{\mu} + \sum_{\beta=1}^{3} \epsilon_{\alpha\beta} r^{\beta}_{\mu}, \tag{1}$$

where the α and β symbols denote the Cartesian components.

In the calculation of the second-order elastic constants in these cubic and hexagonal lattices, we follow an energy–strain scheme (see [32,33]). The lattice was first relaxed to achieve a zero stress state and then strains were applied by multiplying the lattice vectors by the strain matrix. For a lattice initially under no stress, and using Voigt notation, the energy of the strained lattice can be expressed around the equilibrium position as:

$$E = E_0 + \frac{V_0}{2} \sum_{i,j} C_{ij} \epsilon_i \epsilon_j, \tag{2}$$

where E_0 and V_0 are, respectively, the energy and the volume of the unstrained lattice. There are three independent elastic constants for the cubic lattice (C_{11}, C_{12}, C_{44}) and five independent elastic constants (C_{11}, C_{12}, C_{33}, C_{13}, C_{44}) for the hexagonal one, thus three and five sets of finite strains were applied respectively. For each case, eleven equally-spaced strain values were applied between -0.05 and 0.05. The elastic constants were obtained from fitting a quadratic equation to the energy–strain calculated

data points. The bulk modulus B_0 for each structure was calculated using its relationship with the elastic constants.

2.2. Spinodal-Like Stress–Strain Equation of State

From a thermodynamic point of view, the elastic stability limit of a solid at athermal conditions is defined by the point where the second derivative of the internal energy with respect to the volume becomes zero. At the corresponding pressure, also named as the spinodal pressure (p_{sp}), the bulk modulus (B) of the substance tends to zero, and therefore any restoring force given by the chemical bonds is overcome, leading to a crystal rupture or a phase transition [34].

The spinodal locus has been considered as an excellent reference to describe the thermodynamic behavior of solids under high pressure conditions [19,35]. Polymers, metals, covalent and ionic crystals have been analyzed showing that their p-V data is accurately and universally represented through the spinodal constrain. This follows from the fact that along a given isotherm, the isothermal bulk modulus depends on the pressure through the following universal relation [36,37]:

$$B = B^{\star}(p - p_{sp})^{\beta}, \tag{3}$$

where $B^{\star}$ and β are, respectively, the amplitude and the pseudocritical exponent that characterize the pressure behavior of the isothermal bulk modulus.

The spinodal equation of state has not been used only in its volumetric form. For instance, Francisco et al. [20] studied the evolution under isotropic compression of the lattice parameters of rutile TiO_2, showing that a one dimensional (1D) spinodal equation of state (1D-SEOS) can reproduce accurately their pressure dependence. To that, the authors define a linear bulk modulus, or equivalently a directional Young modulus (Y_I, I specifies the direction), and applied the universal relation of Equation (3). Considering both the physical significance and the directional behaviour of this spinodal-like equation of state, in this article we introduce a 1D-SEOS to analytically describe the stress–strain curves associated with tensile stress phenomena. Indeed, under directional stretching, the critical strength attained along the stress–strain curve corresponds to the spinodal stress limit, σ_{sp}. The later parameter accounts for the maximum engineering stress at which the solid breaks, and therefore, represents the elastic limit of the material. Furthermore, at this spinodal point the directional Young modulus Y_I has a value of zero, pointing out that there is no material resistance to a phase transition or rupture. Notice that these two parameters (σ_{sp} and Y_I) are also the one-dimensional analogs of the spinodal pressure and the bulk modulus. Consequently, from this perspective, the spinodal constrain is clearly fulfilled. Accordingly, the stress dependence of Y_I can be accurately described with an amplitude factor $Y_I^{\star}$ and a pseudocritical exponent γ following an equivalent power law form as Equation (3), and taking into account the engeneering convention of signs (σ is positive for tensile and negative for compressive stress):

$$Y_I = Y_I^{\star}(\sigma_{sp} - \sigma)^{\gamma}. \tag{4}$$

Under these premises, an analytical stress–strain EOS can be derived. As the Young modulus is thermodynamically defined as the derivative of the stress with respect to the strain, the simple integration of Equation (4) leads to the following expression for a directional tensile curve:

$$\sigma = \sigma_{sp} - \{Y_I^{\star}(1 - \gamma)(\epsilon_{sp} - \epsilon)\}^{1/(1-\gamma)}. \tag{5}$$

Equation (5) provides an analytical relationship between the stress and the strain along a particular direction of a crystalline solid involving four characteristic parameters. However, it must be emphasized that only three are independent since the spinodal strength, the spinodal strain and the amplitude factor are related realizing that no strain is present at $\sigma = 0$:

$$Y_I^{\star}(1-\gamma) = \frac{\sigma_{sp}^{(1-\gamma)}}{\epsilon_{sp}}. \tag{6}$$

Using this expression in Equation (5), we arrive at our final stress–strain 1D-SEOS:

$$\sigma = \sigma_{sp}\left(1 - \left(\frac{\epsilon_{sp}-\epsilon}{\epsilon_{sp}}\right)^{\frac{1}{1-\gamma}}\right). \tag{7}$$

An interesting feature of the proposed stress–strain SEOS is that it can be also expressed analytically in its energy form. In fact, considering the isotherm at 0 K and neglecting zero point vibrational contributions, the stress is related to the internal energy E and the zero-pressure volume V_0 by means of [38]:

$$\sigma = \frac{1}{V_0}\frac{dE}{d\epsilon}. \tag{8}$$

Consequently, the integrated energy–strain SEOS is:

$$E_{sp} - E = V_0\sigma_{sp}(\epsilon_{sp}-\epsilon) - V_0\frac{(1-\gamma)}{(2-\gamma)}\frac{\sigma_{sp}}{\epsilon_{sp}}^{\frac{1}{1-\gamma}}(\epsilon_{sp}-\epsilon)^{\frac{2-\gamma}{1-\gamma}}, \tag{9}$$

where E_{sp} is the internal energy of the solid at the spinodal strain, or equivalently the spinodal energy. This quantity must be understood as the energy needed to separate the crystallographic planes perpendicular to the stress–strain direction, and therefore to overcome the interatomic forces. Moreover, the spinodal energy can be expressed in terms of the spinodal stress and spinodal strain once we set to zero, the internal energy at zero strain:

$$E_{sp} = V_0\epsilon_{sp}\left(\sigma_{sp} - \frac{1-\gamma}{2-\gamma}\right). \tag{10}$$

An important feature of our current spinodal stress–strain EOS is that the spinodal energy gives us the opportunity to connect the mechanical parameters along a given tensile direction with the cohesive interatomic interactions.

Some words of caution on the notation should be given. First, σ_c and σ_{sp} both represent the critical or ideal strength of the material along a given direction. The first symbol is obtained from (ϵ_i,σ_i) calculated or experimental data, whereas the second one comes from our 1D-SEOS fittings as we discuss later. The same applies to ϵ_c and ϵ_{sp}. Second, in our static simulations (zero temperature and zero point energy contributions neglected), the internal energy of the system E is reduced to the electronic energy obtained in our DFT calculations. Finally, the symbol E is often used in other works to design the Young modulus. To avoid confussion, here we have chosen Y_I for the directional Young modulus.

2.3. Spinodal Equation of State Fittings

The versatility of the proposed 1D-SEOS allows us to fit the Young modulus-stress (Equation (4)), stress–strain (Equation (7)), and energy–strain (Equation (10)) data. Since the spinodal hypothesis is based on the assumption that the universal relationship given in expression Equation (3) can accurately describe the stress dependence of the directional Young modulus, it becomes first necessary to examine if the proposed power law can fit the calculated data, in a reliable manner. To minimize numerical errors induced by the second strain derivative of the energy involved in the $Y_I - \sigma$ curves, a linear interpolation of the computed electronic energy has been performed. In all the cases, adjusted R-squares for the Y_I-σ curves lie in the range between 0.97 and 0.99 and residuals are equally distributed between negative and positive values with a percentage of deviation lower than 7%. In order to test the reliability of our proposed 1D-SEOS, the pseudocritical exponent and the critical strength and

critical strain have been used as fitting parameters to analytically construct the stress–strain curves and energy–strain curves for all the directions and materials studied in this work according to the expressions derived in Section 2.2. Successfully, we obtain that the differences between the analytical curves and the calculated data are always below 1%. A summary of the fitting parameters are presented in Table 1.

Table 1. One dimensional (1D) spinodal equation of state (1D-SEOS) parameters from the fittings to our computed stress–strain data. Units of σ_{sp} are GPa.

Material	Direction	γ	ϵ_{sp}	σ_{sp}
3C-SiC	[100]	0.29	0.35	90.5
	[110]	0.49	0.30	52.3
	[111]	0.36	0.15	45.1
2H-SiC	[001]	0.36	0.15	44.9
	[100]	0.46	0.29	58.0
	[120]	0.34	0.17	50.7
Graphite	[001]	0.35	0.99	0.06
	[100]	0.53	0.26	85.8
	[120]	0.37	0.11	78.3
2H-MoS_2	[001]	0.39	0.05	0.07
	[100]	0.38	0.27	21.4
	[120]	0.46	0.20	14.2

As we can see in Table 1, the γ parameter lies inside the 0.41 ± 0.12 interval, depending on the crystal and the direction considered. These γ values are much lower than the universal β value of 0.85 assumed by Baonza et al. for the volumetric compression of solids [19]. Such a difference is attributed to the fact that we are in the stretching region in this case . Indeed, Brosh et al. [39] studied the dependence of the pseudocritical exponent as a function of the reduced volume both in the compressive and expansive regimes. These authors conclude that while the universal pseudocritical exponent of 0.85 accurately describes the solid under high and moderate pressure, the exponent goes down to the value of 0.5 in the case of the negative pressure regime, which is within the range of the results obtained in our spinodal stress–strain equation of state.

3. 3C-SiC, 2H-SiC, Graphite and 2H-MoS_2: Results and Discussion

3.1. Bulk Properties

This subsection is restricted just to the summary of the equilibrium structural and elastic data of the four structures. Computed lattice constants, bulk moduli and elastic constants are collected in Table 2 along with experimental and other calculated values. Overall, our results are found to be in good agreement with the reported observed data, showing only slight differences due to the overestimation of the lattice constants and underestimation of the elastic constants inherent to the generalized gradient approximation (GGA) level of calculation. The introduction of the DFT-D2 correction, which is intended to take into account the vdW inter-layer interactions, leads our results for graphite and molybdenum disulfide to be in good agreement with the experiments and improves in general other previous local density approximation (LDA) or GGA results. In addition, the controversial C_{12} parameter in 2H-MoS_2, the higher discrepancy (less than 20%) is found in our calculation of C_{11} in graphite (see Table 2). We attribute this deviation to the above tendency of GGA results. Regarding C_{12} in 2H-MoS_2, the situation is different. The discrepancy between the negative value reported in the experimental paper of Feldman [40] and the positive one obtained when the D2 Grimme correction is included in the calculations was discussed by Peelaers and Van de Walle [10]. We only notice here that C_{12} was not directly measured but derived by Feldman using linear compressibilities reported in other

works. Further details can be found in [10]. Overall, our calculated equilibrium properties provide the necessary reliable basis to undertake tensile stress simulations.

Table 2. Zero pressure lattice and elastic constants of 3C- and 2H-SiC polytypes, graphite and 2H-MoS_2. All B_0 values calculated using Voigt elastic constants relationship.

		This Work	Calculated	Experimental
3C-SiC	a(Å)	4.39	4.34 [41], 4.38 [42]	4.34 [43]
	C_{11}(GPa)	341	390 [41], 385 [42]	352 [44]
	C_{12}(GPa)	130	134 [41], 128 [42]	140 [44]
	C_{44}(GPa)	224	253 [41], 264 [42]	233 [44]
	B_0(GPa)	200	219, 213	211
2H-SiC	a(Å)	3.085	3.05 [45], 3.09 [42]	3.076[46]
	c(Å)	5.060	5.00 [45], 5.07 [42]	5.224 [46]
	C_{11}(GPa)	528	541 [45], 536 [42]	501 ± 4 [47]
	C_{12}(GPa)	112	117 [45], 78 [42]	111 ± 5 [47]
	C_{33}(GPa)	565	586 [45], 573 [42]	553 ± 4 [47]
	C_{13}(GPa)	52	61 [45], 31 [42]	52 ± 9 [47]
	C_{44}(GPa)	156	162 [45], 164 [42]	163 ± 4 [47]
	B_0(GPa)	228	238, 214	220
Graphite	a(Å)	2.521	2.451 [48]	2.464 [49]
	c(Å)	7.067	6.582 [50]	6.712 [49]
	C_{11}(GPa)	892	1118 [51]	1109 ± 16 [49]
	C_{12} (GPa)	163	235 [51]	139 ± 36 [49]
	C_{33} (GPa)	31	29 [51]	38.7 ± 7 [49]
	C_{13} (GPa)	5	8.5 [51]	0 ± 3 [49]
	C_{44} (GPa)	6	−2.8 [51]	5 ± 3 [49]
	B_0 (GPa)	240	307	281
2H-MoS_2	a(Å)	3.19	3.16 [52]	3.163 [53]
	c(Å)	12.56	12.296 [52]	12.341 [53]
	C_{11} (GPa)	220	218 [52]	238 [40]
	C_{12} (GPa)	45	38 [52]	−54 [40]
	C_{33} (GPa)	40	35 [52]	52 [40]
	C_{13} (GPa)	16	17 [52]	23 [40]
	C_{44} (GPa)	26	15 [52]	19 [40]
	B_0 (GPa)	75	68	57

3.2. Ideal Strength with and without Transverse Stress

This subsection is devoted to the calculation of the strain-stress curves of the four structures considered in this study. First, we collect in Figure 1 the results under vanishing transverse stress. For 3C-SiC and 2H-SiC, calculated points are very similar to those reported by Umeno, Kubo, and Nagao [42]. For graphite, our in-plane stress–strain curves show maxima at similar strain values to those reported by Liu et al. [48] for graphene, although we compute critical strengths along these directions around 25 GPa lower than in their work. This is due in part to differences between LDA (Liu et al.) and GGA (ours) levels of calculation, and on the other hand, to differences in the system, single sheet (graphene) and the bulk (graphite). To the best of our knowledge, the corresponding curve for the c direction has not been reported so far. Analogously, we have not found previous strain-stress curves along this direction for bulk 2H-MoS_2, whereas for the in-plane directions the previous reported studies refer to single- or few-layer 2H-MoS_2 [54,55]. These results indicate a noticeable decreasing of σ_c as the size of the slab increases, which is also the expected trend according to our calculations.

It is usual to refer to the chemical bonding network to interpret, at an atomic level, the differences in the strain-stress curves between compounds and/or directions. Without being strictly quantitative, while keeping the basic chemical meaning, a simple and practical indicator able to account for the majority of these differences is proposed as follows. Each chemical bond in the unit cell is described

by a vector connecting its two bound nearest-neighbor atoms. The projection of this vector along the corresponding tensile direction is evaluated and the sum calculated over all the bonds in the unit cell is defined as the total effective bond length (EBL) associated to that direction. The two main structural effects induced in the chemical bonds by the tensile strain (changes in bonding lengths and angles) are essentially captured in this parameter. EBL values exhibit the expected trend always increasing as the strain increases up to the stability limit.

Figure 1a shows that in 3C-SiC the slopes in the low strain region are nearly equal regardless of the direction. However, the maximum stress value strongly depends on the direction of the deformation with a critical strength nearly twice as large along the [100] axis (ϵ_c= 0.35 and σ_c = 91 GPa), as that found for [110] (ϵ_c = 0.30 and σ_c = 53 GPa) and [111] (ϵ_c = 0.15 and σ_c = 45 GPa). We notice that along [100] all tensile forces are equally distributed over the Si-C bonds. This is in contrast to the tension along the [110] and [111] directions. For example, in the latter, one of the four C nearest neighbors of a given Si atom stand along the same [111] direction and the corresponding Si-C bond suffers a pure stretching, whereas the stretching of the other three Si-C bonds is not so effective and involves bond angle modifications upon the tensile strain along the [111] direction. At zero strain, the previously defined EBL parameter already has a value roughly twice greater for the [100] direction (17.5 Å) than for the [110] (9.3 Å) and [111] (9.5 Å) directions. Thus, although the order between the [100] and [111] directions is not captured considering just the equilibrium structure, the EBL parameter catches the essential difference between the [100] direction and these two other directions.

The stress–strain curves during uniaxial tension with vanishing transverse stress in 2H-SiC are shown in Figure 1b. Slopes in the low strain (harmonic) region are almost exactly equal whereas the maximum stress value strongly depends on the direction of the deformation. The stress–strain relation in 2H-SiC [001] (ϵ_c = 0.15 and σ_c = 45 GPa) and 3C-SiC [111] are nearly identical. It is so because of the similarity of the lattice planes normal to the stress direction, and so are the curves of 2H-SiC [100] (ϵ_c = 0.29 and σ_c = 58 GPa) and 3C-SiC [110]. The stress–strain relation in 2H-SiC along [120] shows intermediate values (ϵ_c = 0.20 and σ_c = 50 GPa). Again, these values correlate with the effective Si-C bond lengths along the corresponding directions. Calculated EBL values in Å for the [100], [120] and [001] are, respectively, 21.3, 16.8, and 12.3, following the same trend as σ_c and in agreement also with previous interpretations in terms of next-nearest Si-C interactions by Umeno et al. [42].

In Figure 1c,d, the responses of graphite and 2H-MoS_2 to tensile stress along the [100], [120], and [001] directions are displayed. Here, the laminar nature of these two compounds is clearly revealed by the very low critical strength values along the *c* axis (ϵ_c = 0.13 and σ_c = 0.063 GPa in graphite and ϵ_c = 0.05 and σ_c = 0.069 GPa in 2H-MoS_2) which is in concordance with the weak van der Waals nature of the inter-layer interaction. At low strains, the in-plane graphite strains reveal an isotropic 2D elastic behavior in good agreement with previous DFT calculations [56]. At large in-plane strains, the lattice layers start to behave anisotropically and the critical stress along the next-nearest-neighbor [100] direction (ϵ_c = 0.26 and σ_c = 86 GPa in graphite and ϵ_c = 0.27 and σ_c = 22 GPa in 2H-MoS_2) becomes greater than that along the nearest-neighbor [120] direction (ϵ_c = 0.11 and σ_c = 78 GPa in graphite and ϵ_c = 0.20 and σ_c = 14 GPa in 2H-MoS_2). Expected differences between stronger C–C than Mo–S intralayer bonds are also clearly manifested when comparing these data.

For all directions and structures, we now analyze new results coming from the proposed analytical 1D-SEOS. All the curves in the four panels of Figure 1 were obtained from the 1D-SEOS fittings to the calculated strain-stress data. The performance of the 1D-SEOS is apparent and allows us to derive with confidence critical stress and critical strain values from the corresponding fitting parameters σ_{sp} and ϵ_{sp}, respectively. We have checked that the trends and specific values of these two key parameters compare with high accuracy with our first-principles computed numerical values (see Table 1). Thus, we arrive to this interesting conclusion: the 1D-SEOS of Equation (7) is an appropriate analytical function for describing stress–strain data.

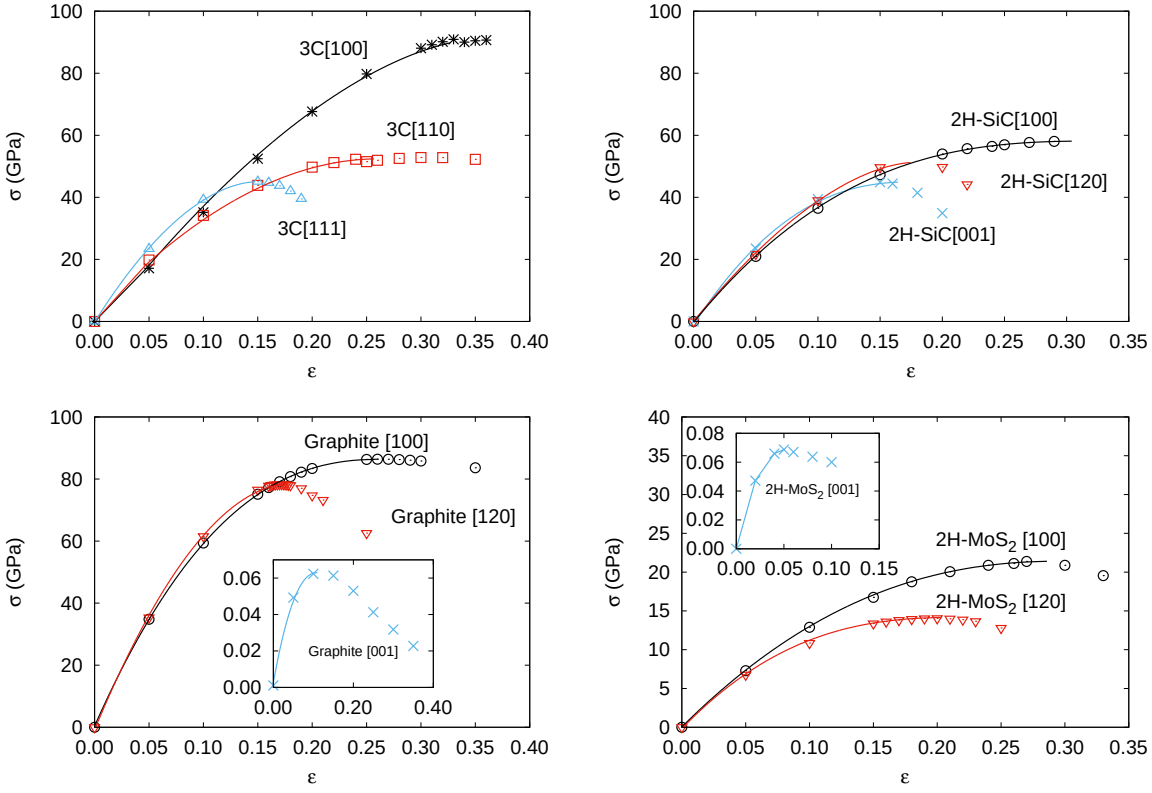

Figure 1. Calculated strain-stress curves without transverse stress for: 3C-SiC (**top left**), 2H-SiC (**top right**), Graphite (**bottom left**), and 2H-MoS_2(**bottom right**).

We noticed earlier that multi-load conditions may be present in manufacturing processes, combining thermal effects and epitaxial growth. As a particular situation of these conditions, in a second round of simulations, we have studied the effects of superimposing transverse stress (both compressive and tensile) on the previous tensile directions for the four structures. We detected convergence problems in some simulations that have hindered the calculations in the compressive (negative) transverse stress range in 2H-MoS_2, and also along the [100] direction in the positive range of this compound. Based on previous resuls in other covalent systems [42], the expected trend is a decreasing of the critical strength as we increase the superimposed transverse stress from negative to positive values. In fact, this is the computed behavior for the majority of situations we have studied. For example, the critical strength σ_c is lowered by the transverse stress σ_t in all the directions in 3C-SiC (except [110]), 2H-SiC (except [100]), graphite, and 2H-MoS_2. In this two laminar compounds, we obtain just one value at the most negative transverse stress breaking the decreasing trend along the [120] direction. All these results are displayed in Figure 2 and are in complete agreement with the computed data in 3C- and 2H-SiC reported by Umeno et al. [42]. In general, the unexpected positive slope in the critical strength-transverse stress curve appears at compressive transverse stress values. In the tensile regime, all the directions and structures show a modulated lowering of the critical strength as the transverse tension increases. This fact is compatible with the overall weakening of the compounds as multi-load conditions are enhanced, or, in Umeno et al. words as due to the higher strain energy stored in the material . However, we would like to notice that the opposite behavior was also found by Sestak et al. [15] and Cerný et al. [18]. The increasing of the critical strength under sumperimposed positive lateral tensile stress obtained in their calculations might be due to the different nature of the chemical bonding network. These authors deal with metallic materials where directional bonds are not identified, thus preventing the use for example of our EBL parameter that we introduce in what follows.

Interestingly enough, we observed an equivalent behavior when we analyzed the computed EBL parameters. In all but the cases where we have detected an exception, the calculated effective bond length parameter at the critical strain condition decreases monotonically as we superimpose the transverse stress on the corresponding tensile strain direction. Thus, we found that the decreasing of the critical strength value correlates with the decreasing in the EBL parameter. For example, along the [111] direction in 3C-SiC, EBL continuously decreases from 11.00 Å at $\sigma_t = -30$ GPa to 10.78 Å at $\sigma_t = +30$ GPa. The corresponding values at the same transverse stress conditions for the [100] direction are 24.71 Å and 21.18 Å. Similar trends are found for the EBL parameter along the [120] and [001] directions in 2H-SiC. On the contrary, in those cases where negative transverse stresses induce an unexpected behavior, this EBL parameter also shows as increasing as the transverse stress increases, up to the condition of vanishing transverse stress. Thus, along [110] in 3C-SiC and [100] in 2H-SiC, the values of EBL at $\sigma_t = -30$ GPa are, respectively, 10.94 Å and 26.08 Å, increasing up to 11.49 Å and 26.24 Å at $\sigma_t = 0$ GPa, and finally decreasing to 10.97 Å and 24.13 Å at $\sigma_t = +30$ GPa. The reason why a reduction in the critical strength occurs as compressive transverse is superimposed has been explained by the appearance of a thermodynamic competitive phase as the rock-salt structure in 3C-SiC [42]. Here, we also see that this reduction in the σ_c also correlates with the fact that the effective Si-C bond lengths along the [110] and [100] directions in 3C-SiC and 2H-SiC, respectively, show lower values at the critical conditions when the compressed transverse stress is increased, thus correlating with the trend followed by the critical strength.

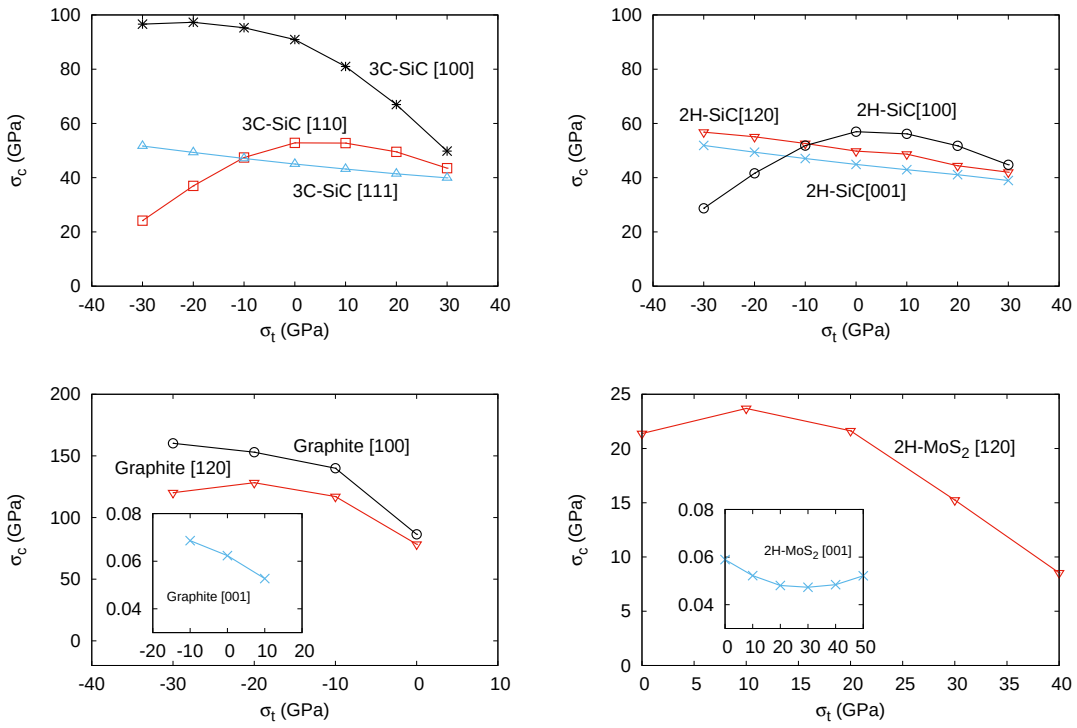

Figure 2. Calculated critical stress-transverse stress curves for: 3C-SiC (**top left**), 2H-SiC (**top right**), Graphite (**bottom left**), and 2H-MoS_2(**bottom right**).

Other Outcomes of the Stress–Strain SEOS: Energetics and Directional Young Moduli

As stated in Section 2.3, our analytical scheme allows us to gather information, not only on the critical parameters, but also on the energetics of crystalline materials and on the Young moduli along specific tensile directions. From an experimental point of view, stress–strain data can be directly measured for particular directions whereas the corresponding energy–strain curves remain only accessible once an equation of state is proposed. Equation (10) displays how, by simple integration

of our stress–strain 1D-SEOS, analytical energy–strain curves can be derived using data either from experiments or from computer simulations. In the previous subsection, we have shown that our calculated (ϵ_i,σ_i) data points are well described by the proposed 1D-SEOS. Here, the integrated SEOS for all the directions and materials studied in this work are represented in Figure 3. The symbols correspond to the energy minima at selected strains obtained from our first-principles calculations. The calculated parameters associated with the integrated forms are collected in Table 3.

The analytical energy curves clearly reflect the good quality of the fittings (see Figure 3). Two parameters define the shape of each of these curves, ϵ_{sp} and E_{sp}. The first one, previously discussed in relation to the stress–strain curves (see Table 1), identifies the abscissa of the inflexion point, where the directional Young modulus vanishes. The ordinate of this point is E_{sp} (see Table 3) and correlates quite well with the critical/spinodal strength calculated along each of the directions explored for the materials under study in this work. The higher the strength, the higher the energy required to induce an elastic instability in the material. Not surprising, the highest values are obtained in 3C-SiC along the [100] direction and graphite along the [100] direction, just the same systems and directions where we had found the greatest values for σ_c (and σ_{sp}). E_{sp} values provide also information on the energy stored in the material due to the tensile stretching. For example, along the last two directions the energy stored is expected to be higher than along other directions with flatter energy–strain curves, as [001] directions in graphite and 2H-MoS_2 (see Figure 3). Notice that for these two situations with the weakest cohesive interactions, values are so low (within the accuracy of the calculations) that only a limit value is given. Overall, we believe that these results evidence the utility of the energy–strain SEOS.

As regards the directional Young modulus, we can easily derive a simple expression at zero stress $Y_1(0)$ involving the three parameters of the stress–strain 1D-SEOS by evaluating Equation (4) at zero stress:

$$Y_1(0) = \frac{\sigma_{sp}}{\epsilon_{sp}(1-\gamma)}. \quad (11)$$

This parameter is discussed below.

Table 3. Energy and Young modulus parameters from the integrated stress–strain SEOS fittings.

Material	Direction	$Y_1(0)$ (GPa)	E_{sp} (kJ/mol)
3C-SiC	[100]	396	219
	[110]	407	110
	[111]	478	50
2H-SiC	[001]	481	50
	[100]	437	142
	[120]	450	66
Graphite	[001]	0.99	<1
	[100]	746	201
	[120]	746	113
2H-MoS_2	[001]	2.41	<1
	[100]	150	69
	[120]	140	153

In 3C-SiC, the directional Young moduli at zero stress are (in GPa) 396, 406, 478 GPa for the [100] [110] and [111] directions, respectively. These results are in concordance with the directional Young moduli calculated through the theory of representation surfaces [57]. For instance, in the case of the [111] direction

$$Y_{111} = \left(S_{11} - \frac{2}{3}\left(S_{11} - S_{12} - \frac{1}{2}S_{44}\right)\right)^{-1}, \quad (12)$$

where S_{11}, S_{12}, and S_{44} are the compliance constants related to the elastic constants by:

$$S_{11} = \frac{C_{11}+C_{12}}{(C_{11}-C_{12})(C_{11}+2C_{12})}, S_{12} = \frac{-C_{12}}{(C_{11}-C_{12})(C_{11}} + 2C_{12}), S_{44} = \frac{1}{C_{44}}. \quad (13)$$

According to the data from Table 2, and using the above equations, the calculated value for $Y_{111}(0)$ is 489 GPa in good agreement with the parameter obtained from our 1D-SEOS.

In this case, the elastic behavior of the cubic SiC polytype is not enterely isotropic and $Y_I(0)$ slightly increases along the sequence [100] [110] and [111]. $Y_I(0)$ provides a quantitative measure of the initial slope of the stress–strain curve, thus representing the resistance of the material to a tensile distortion along a particular direction at equilibrium. Under this perspective, the values of $Y_I(0)$ in the [100], [110] and [111] series of 3C-SiC inform that the direction [111] offers the highest resistance to a strain stretching at zero stress. In 2H-SiC, the values of $Y_I(0)$ point out that all the directions studied present similar resistance to distortion. Here, the solid behaves less anisotropically than in the case of the cubic polytype, expanding a narrower range of values, although both polytypes display similar zero stress Young moduli.

Let us finally conclude by analyzing these zero stress directional Young moduli in graphite and 2H-MoS_2. Layered materials constitute a severe test for our model since weak and covalent interactions are simultaneously present. In both compounds, the van der Waals nature of the inter-layer interactions is revealed through the values of the directional Young modulus provided by the spinodal parameters. $Y_{001}(0)$ values (in GPa) are as low as 0.99 and 2.40 for graphite and 2H-MoS_2, respectively, in contrast with the values along the [100] and [120] directions which are, respectively, 748 and 728 for graphite, and 150 and 140 for 2H-MoS_2. The latter values can be compared with the intra-layer Young modulus reported for graphite and MoS_2 by other authors. For instance, for graphite goes from 700 to 1100 GPa ([56] and references therein), whereas for 2H-MoS_2 the values range between 130 and 220 GPa [58–60] showing a good agreement with the results obtained in this work. At this point, it must also be emphasized that our Young modulus values reflect the expected different intralayer bond strengths between the C–C and Mo–S bonds, as we previously detected in the analysis of the 1D-SEOS parameters (see Section 3.2).

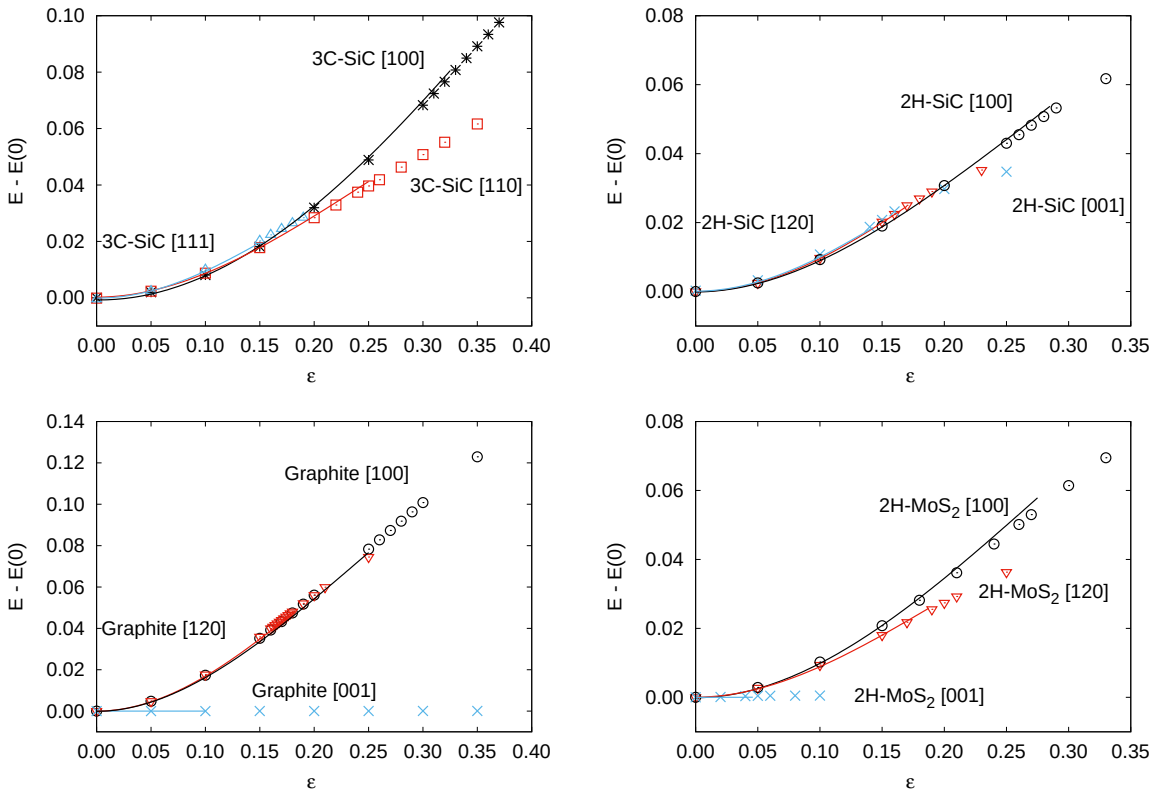

Figure 3. Calculated energy–strain curves for: 3C-SiC (**top left**), 2H-SiC (**top right**), Graphite (**bottom left**), and 2H-MoS_2(**bottom right**).

4. Conclusions

The critical strength of 3C- and 2H-SiC, graphite, and 2H-MoS_2 were evaluated by means of first principles quantum-mechanical methodologies based on the DFT approximation. Both vanishing and superimposed transverse stress over uniaxial tensile strains were considered in order to evaluate the critical (ideal) strength of the four crystalline structures. The critical strength is found to depend on the particular crystallographic direction revealing the expected stronger mechanical anisotropy in the layered compounds. In graphite and molybdenum disulfide layers, after an isotropic behavior at the low strain regime, we observe a different behavior along the two in-plane directions, the critical tensile strength being smaller in the nearest-neighbor than in the next-nearest-neighbor direction. In these crystals, the lowest value of σ_c is obtained in the c-direction as expected given the weak inter-layer vdW interactions. The critical tensile strength is generally decreased by the transverse tension. Reduction in the critical strength by large transverse compression occurs in some structures and orientations in concordance with an increase in the effective bond lengths in those conditions.

We present a new 1D-SEOS analytical function that was successfully applied to the computed strain-stress data points, and which can be also used to describe results from tensile stress experiments. The spinodal strain ϵ_{sp} along with the corresponding spinodal stress σ_{sp} fitting parameters have been calculated for the two covalent and the two layered compounds. These parameters are identified with the critical strength and strain values provided they appear at the instability elastic limit. In addition, the integrated energy–strain SEOS reveals an interesting equation, enclosing information on the energy stored in the material along tensile processes and providing data on the required energy to reach the instability elastic limit .

Author Contributions: Conceptualization, J.M.R., M.A.S., Á.L., V.G.B. and F.B.; methodology, H.C., M.A.S. and Á.L.; investigation, C.H., Á.L. and R.F.; writing–original draft preparation, C.H., J.M.R. and Á.L.; writing–review and editing, J.M.R.; Á.L., R.F.; supervision, V.G.B., J.M.R., F.B. and M.A.S.; project administration, R.F.; funding acquisition, V.G.B., J.M.R. and M.A.S.

Funding: This research was funded by the EU (FEDER) and Spanish institutions MINECO and MICINN under the projects CTQ2015-67755-C2-R and PGC2018-094814-B-C22, and Principado de Asturias-FICYT, project GRUPIN14-049.

Acknowledgments: Special thanks are due to the colleague A.H. Meziani for useful discussions. Computer facilities of MALTA-Computer center at the Universidad de Oviedo are gratefully acknowledged.

Conflicts of Interest: The funders had no role in the design of the study; in the collection, analyses, or interpretation of data; in the writing of the manuscript, or in the decision to publish the results.

References

1. Asano, K.; Hayashi, T.; Takayama, D.; Sugawara, Y.; Ryu, S.H.; Palmour, J.W. Temperature dependence of On-state characteristics, and Switching characteristics of 5 kV class 4H-SiC SEJFET. *IEEE Trans. Ind. Appl.* **2005**, *125*, 147–152. [CrossRef]
2. Peña-Álvarez, M.; del Corro, E.; Morales-García, Á.; Kavan, L.; Kalbac, M.; Frank, O. Single Layer Molybdenum Disulfide under Direct Out-of-Plane Compression: Low-Stress Band-Gap Engineering. *Nano Lett.* **2015**, *15*, 3139–3146. [CrossRef] [PubMed]
3. Tsai, M.-L.; Su, S.-H.; Chang, J.-K.; Tsai, D.-S.; Chen, C.-H.; Wu, C.-I.; Li, L.-J.; Chen, L.-J.; He, J.-H. Monolayer MoS_2 heterojunction solar cells. *ACS Nano* **2014**, *8*, 8317–8322. [CrossRef] [PubMed]
4. Recio, J.M.; Menéndez, J.M.; Otero-de-la-Roza, A. (Eds.) *An Introduction to High-Pressure Science and Technology*; CRC-Press: Boca Raton, FL, USA, 2016.
5. Radisavljevic, B.; Radenovic, A.; Giacometti, V.; Kis, A. Single-layer MoS_2 transistors. *Nat. Nanotechnol.* **2011**, *6*, 147–150. [CrossRef]
6. Wang, H.; Yu, L.; Lee, Y.H.; Shi, Y.; Hsu, A.; Chin, M.L.; Li, L.J.; Dubey, M. Kong, J.; Palacios, T. Integrated circuits based on bilayer MoS_2 transistors. *Nano Lett.* **2012**, *12*, 4674–4680. [CrossRef]
7. Fiori, G.; Szafranek,B.N.; Iannaccone, G.; Neumaier, D. Velocity saturation in few-layer MoS_2 transistor. *Appl. Phys. Lett.* **2013**, *103*, 233509(1)–233509(4). [CrossRef]

8. Kim, S.; Konar, A.; Hwang, W.S.; Lee, J.H.; Yang, J.; Jung, C.; Kim, H.; Yoo, J.B.; Choi, J.Y. High-mobility and low-power thin-film transistors based on multilayer MoS_2 crystals. *Nat. Commun.* **2012**, *3*, 1011–1017. [CrossRef]
9. Bollmann, W.; Spreadborough, J. Action of Graphite as a Lubricant. *Nature* **1960**, *186*, 29–30. [CrossRef]
10. Peelaers, H.; Van de Walle, C.G. Elastic Constants and Pessure-Induced Effects in MoS_2. *J. Phys. Chem.* **2014**, *118*, 12073–12076.
11. Kohn, W.; Sham, L.J. Self-Consistent Equations Including Exchange and Correlation Effects. *Phys. Rev.* **1965**, *140A*, 1133–1138. [CrossRef]
12. Argaman, N.; Markov, G. Density functional theory: An introduction. *Am. J. Phys.* **2000**, *68*, 69–79. [CrossRef]
13. Umeno, Y.; Kitamura, T. Ab Initio Simulation on Ideal Shear Strength of Silicon. *Mater. Sci. Eng.* **2002**, *88*, 79–84. [CrossRef]
14. Cerný, M.; Rehák, P.; Umeno, Y.; Pokluda, J. Stability and strength of covalent crystals under uniaxial and triaxial loading from first principles. *J. Phys. Condens. Matter* **2013**, *25*, 35401–35408. [CrossRef] [PubMed]
15. Sesták, P.; Friák, M.; Holec, D.; Vsianská, M.; Sob, M. Strength and brittleness of interfaces in Fe-Al superalloy nanocomposites under multiaxial loading: An ab initio and atomistic study. *Nanomaterials* **2018**, *8*, 873. [CrossRef]
16. Umeno, Y.; Cerný, M. Effect of normal stress on the ideal shear strength in covalent crystals. *Phys. Rev. B* **2008**, *77*, 100101–100104. [CrossRef]
17. Umeno, Y.; Cerný, M. Ideal shear strength under compression and tension in C, Si, Ge, and cubic SiC: An ab initio density functional theory study. *J. Phys. Condens. Matter* **2011**, *23*, 385401(1)–385401(7). [CrossRef]
18. Cerný, M.; Rehák, P.; Pokluda, J. The origin of lattice instability in bcc tungsten under triaxial loading. *Philos. Mag.* **2017**, *97*, 2971–2984. [CrossRef]
19. Baonza, V.G.; Cáceres, M.; Núñez, J. Universal compressibility behavior of dense phases. *Phys. Rev. B* **1995**, *51*, 28–37. [CrossRef]
20. Francisco, E.; Bermejo, M.; García Baonza, V.; Gerward, L.; Recio, J.M. Spinodal equation of state for rutile TiO_2. *Phys. Rev. B* **2003**, *67*, 064110(1)–064110(8). [CrossRef]
21. Gonze, X.; Beuken, J.M.; Caracas, R.; Detraux, F.; Fuchs, M.; Rignanese, G.M.; Sindic, L.; Verstraete M.; Zerah, G.; Jollet, F.; et al. First-principles computation of material properties: The ABINIT software project. *Comput. Mater. Sci.* **2002**, *25*, 478–492. [CrossRef]
22. Gonze, X.; Amadon, B.; Anglade, P.-M.; Beuken, J.-M.; Bottin, F.; Boulanger, P.; Bruneval, F.; Caliste, D.; Caracas, R.; Côté, M.; et al. ABINIT: First-principles approach to material and nanosystem properties. *Comput. Phys. Commun.* **2009**, *180*, 2582–2615. [CrossRef]
23. Perdew, J.P.; Burke, K.; Ernzerhof, M. Generalized Gradient Approximation Made Simple. *Phys. Rev. Lett.* **1996**, *77*, 3865–3868. [CrossRef] [PubMed]
24. Grimme, S. Semiempirical GGA-Type Density Functional Constructed with a Long-Range Dispersion Correction. *J. Comput. Chem.* **2006**, *27*, 1786–1799. [CrossRef] [PubMed]
25. Ambrosetti, A.; Ferri, N.; Di Stasio, R.A., Jr.; Tkatchencko, A. Wavelike charge density fluctuations and van der Waals interactions in the nanoscale. *Science* **2016**, *351*, 1171–1176. [CrossRef]
26. Ambrosetti, A.; Silvestrelli, P.L. Hidden by graphene—Towards effective screening of interface van der Waals interactions vian monolayer coating. *Carbon* **2018**, *139*, 486–491. [CrossRef]
27. Ambrosetti, A.; Silvestrelli, P.L. Faraday-like Screening by Two-Dimensional Nanomaterials: A Scale Dependent Tunable Effect. *J. Phys. Chem. Lett.* **2019**, *10*, 2044–2050. [CrossRef]
28. Trouillier, N.; Martins, J.L. Efficient pseudopotentials for plane-wave calculations. *Phys. Rev. B* **1991**, *43*, 1993–2006. [CrossRef]
29. Monkhost, H.J.; Pack, J.D. Special points for Brillouin-zone integrations. *Phys. Rev. B* **1976**, *13*, 5188–5192. [CrossRef]
30. Momma, K.; Izumi, F. VESTA 3 for three-dimensional visualization of crystal, volumetric and morphology data. *J. Appl. Crystallogr.* **2011**, *44*, 1272–1276. [CrossRef]
31. Born, M.; Huang, K. *Dynamical Theory of Crystal Lattice*; Oxford Clarendon Press: London, UK, 1966.
32. Zeina M.J.; Servio, P.; Rey A.D. Ideal Strength of Methane Hydrate and Ice Ih from First-Principles. *Cryst. Growth. Des.* **2015**, *15*, 5301–5309.
33. Otero de la Roza, A.; Luaña, V. Runwien: A text-based interface for the WIEN package. *Comput. Phys. Commun.* **2009**, *180*, 800–812. [CrossRef]

34. Baonza, V.G.; Taravillo, M.; Cáceres, M.; Núñez, J. Universal features of the equation of state of solids from a pseudospinodal hypothesis. *Phys. Rev. B* **1996**, *53*, 5252–5258. [CrossRef] [PubMed]
35. Taravillo, M.; Baonza, V.G.; Núñez, J.; Cáceres, M. Simple equation of state for solids under compression. *Phys. Rev. B* **1996**, *54*, 7034–7045. [CrossRef] [PubMed]
36. Baonza, V.G.; Cáceres, M.; Núñez, J. High-pressure compressibility behavior of liquids referred to a pseudospinodal curve. *Chem. Phys. Lett.* **1994**, *228*, 137–143. [CrossRef]
37. Baonza, V.G.; Cáceres, M.; Núñez, J. Universal Behavior of Compressed Liquids. *J. Chem. Phys.* **1994**, *19*, 4955–4958. [CrossRef]
38. Ogata, S.; Li, J.; Shibutant, N.; Yip, S. Ideal shear strain of metals and ceramics. *Phys. Rev. B* **2004**, *70*, 104104(1)–104104(7). [CrossRef]
39. Brosh, E.; Makov, G.; Shneck, R.Z. The spinodal constraint on the equation of state of expanded fluids. *J. Phys. Condens. Matter* **2003**, *19*, 2991–3001. [CrossRef]
40. Feldman, J.L. Elastic constants of 2H-MoS_2 and 2H-$NbSe_2$ extracted from measured dispersion curves and linear compressibilities. *J. Phys. Chem. Solids* **1976**, *37*, 1141–1144. [CrossRef]
41. Karch, K.; Pavone, P.; Windl, W.; Schuelt, O.; Strauch, D. Ab initio calculation of structural and lattice-dynamical properties of silicon carbide. *Phys. Rev. B* **1994**, *50*, 17054–17063. [CrossRef]
42. Umeno, Y.; Kubo, A.; Nagao, S. Density functional theory calculation of ideal strength of SiC and GaN: Effect of multi-axial stress. *Comput. Mater. Sci.* **2015**, *109*, 105–110. [CrossRef]
43. Ioffeinstitut. 2003. Available online: http://www.ioffe.ru/SVA/NSM (accessed on 18 August 2019).
44. Li, Z.; Brandt, R.C. The single-crystal elastic constants of cubic (3C) SiC to 1000 °C. *J. Mater. Sci.* **1987**, *22*, 2557–2559. [CrossRef]
45. Saramasak, K.; Limpijumnong, S.; Lambrecht, W.R.L. First principles calculations of elastic properties under pressure in SiC. *Comput. Mater. Sci.* **2010**, *49*, S43–S46.
46. Villard, P.; Calvert, L.D. *Pearson's Handbook of Crystallographic Data for intermetallic Phases*; ASM international: Cleveland, OH, USA, 1991.
47. Kamitani, K.; Grimsditch, M.; Nipko, J.C.; Loong, C.K.; Okada, M.; Kimura, I. The elastic constants of silicon carbide: A Brillouin-scattering study of 4H and 6H SiC single crystals. *J. Appl. Phys.* **1997**, *82*, 3152–3154. [CrossRef]
48. Liu, F.; Ming, P.; Li, J. Ab initio calculation of ideal strength and phonon instability of graphene under tension. *Phys. Rev. B* **2007**, *76*, 064120(1)–064120(7). [CrossRef]
49. Bosak, A.; Krisch, M.; Mohr, M.; Maultzsch, J.; Thomsen, C. Elasticity of single-crystalline graphite: Inelastic x-ray scattering study. *Phys. Rev. B* **2007**, *75*, 153408(1)–153408(4). [CrossRef]
50. Ooi, N.; Rairkar, A.; Adams, J.B. Density functional study of graphite bulk and surface properties. *Carbon* **2006**, *44*, 231–242. [CrossRef]
51. Mounet, N.; Marzari, N. First-principles determination of the structural, vibrational and thermodynamic properties of diamond, graphite, and derivatives. *Phys. Rev. B* **2005**, *71*, 205214(1)–205214(14). [CrossRef]
52. Alexiev, V.; Prins, R.; Weber, T. Ab initio study of MoS_2 and Li adsorbed on the (10-10) face of MoS_2. *Phys. Chem. Chem. Phys.* **2000**, *2*, 1815–1827. [CrossRef]
53. Fan, D.; Xu, J.; Ma, N.; Liu, J.; Xie, H. P-V-T Equation of state of molibdenite (MoS_2) by a diamond anvil cell and in situ synchrotron angel-dispersive X-ray diffraction. *Phys. B* **2014**, *451*, 53–57. [CrossRef]
54. Li, T. Ideal strength and phonon instability in single-layer MoS_2. *Phys. Rev. B* **2012**, *85*, 235407(1)–235407(5). [CrossRef]
55. Li, P.; Jiang, C.; Xu, S.; Zhuang, Y.; Gao, L.; Hu, A.; Wang, H.; Lu, Y. In situ nanomechanical characterization of multi-layer MoS_2 membranes: from intraplanar to interplanar fracture. *Nanoscale* **2017**, *9*, 9119–9128. [CrossRef] [PubMed]
56. Abbasi-Pérez, D.; Menéndez, J.M.; Recio, J.M.; Otero-de-la-Roza, A.; del Corro, E.; Taravillo, M.; Baonza, V.G.; Marqués, M. Modeling graphite under stress: Equations of state, vibrational modes, and interlayer friction. *Phys. Rev. B* **2014**, *90*, 054105(1)–054105(10). [CrossRef]
57. Nye, J.F. *Physical Properties of Crystals*; Oxford University Press: New York, NY, USA, 2004.
58. Bertolazzi, S.; Brivio, J.; Kis, A. Stretching and Breaking of Ultrathin MoS_2. *ACS Nano* **2011**, *5*, 9703–9709. [CrossRef]

59. Lorenz, T.; Teich, D.; Joswig, J.O.; Seifert, G. Theoretical Study of the Mechanical Behavior of Individual TiS_2 and MoS_2 Nanotubes. *J. Phys. Chem. C* **2012**, *116*, 11714–11721. [CrossRef]
60. Cooper, R.C.; Lee, C.; Marianetti, C.A.; Wei, X.; Hone, J.; Kysar, J.W. Nonlinear elastic behavior of two-dimensional molybdenum disulfide. *Phys. Rev. B* **2013**, *87*, 035423-1–035423-11. [CrossRef]